Thermal and Plasma Simulations of Comet C/1995 O1 (Hale-Bopp) and the Rosetta Target Comet 67P/Churyumov-Gerasimenko

Von der Fakultät für Elektrotechnik, Informationstechnik, Physik
der Technischen Universität Carolo-Wilhelmina
zu Braunschweig
zur Erlangung des Grades eines
Doktors der Naturwissenschaften
(Dr.rer.nat.)
genehmigte
Dissertation

von Nikolaos Gortsas
aus Katerini/Griechenland

1. Referent: Prof. Dr. rer. nat. Uwe Motschmann
2. Referent: Prof. Dr. rer. nat. Karl-Heinz Glaßmeier
eingereicht am: 17. Mai 2010
mündliche Prüfung (Disputation) am: 8. Juli 2010
Druckjahr: 2010

Veröffentlichungen der Dissertation

Teilergebnisse aus dieser Arbeit wurden mit Genehmigung der Fakultät für Elektrotechnik, Informationstechnik, Physik, vertreten durch den Mentor der Arbeit, in folgenden Beiträgen vorab veröffentlicht.

Publikationen

- Gortsas, N., Motschmann, U., Kührt, E., Knollenberg, J., Simon, S. & Boesswetter, A. Mapping of coma anisotropies to plasma structures of weak comets: a 3-D hybrid simulation study. Annales Geophysicae, 27, 1555-1572 (2009).

- Gortsas, N., Kührt, E., Motschmann, U. & Keller, H. U. Thermal model of water and CO activity of comet C/1995 O1 (Hale-Bopp). Eingereicht bei Icarus (2010).

- Gortsas, N., Motschmann, U., Kührt, E., Glassmeier, K.-H., Hansen, K. C., Müller, J. & Schmidt, A. Global plasma parameter simulation of Comet 67P/Churyumov-Gerasimenko approaching the Sun. Eingereicht bei Astronomy and Astrophysics (2010).

- Küppers, M., Keller, H. U., Kührt, E., A'Hearn, M., Altwegg, K., Bertrand, R., Busemann, H., Capria, M.T., Colangeli, L., Davidsson, B., Ehrenfreund, P., Knollenberg, J., Mottola, S., Rathke, A., Weiss, P., Zolensky, M., Akim, E., Basilevsky, A., Galimov, E., Gerasimov, M., Korablev, O., Lomakin, I., Marov, M., Martynov, M., Nazarov, M., Zakharov, A., Zelenyi, L., Aronica, A., Ball, A.J., Barbieri, C., Bar-Nun, A., Benkhoff, J., Biele, J., Biver, N., Blum, J., Bockelee-Morvan, D., Botta, O., Bredehöft, J.-H., Capaccioni, F., Charnley, S., Cloutis, E., Cottin, H., Cremonese, G., Crovisier, J., Crowther, S.A., Epifani, E.M., Esposito, F., Ferrari, A.C., Ferri, F., Fulle, M., Gilmour, J., Goesmann, F., Gortsas, N., Green, S. F., Groussin, O., Grün, E., Gutirrez, P. J., Hartogh, P., Henkel, T., Hilchenbach, M., Ho, T.-M., Horneck, G., Hviid, S. F., Ip, W.-H., Jäckel, A., Jessberger, E., Kallenbach, R., Kargl, G., Kömle, N. I., Korth, A., Kossacki, K., Krause, C., Kröger, H., Li, Z.-Y., Licandro, J., Lopez-Moreno, J. J., Lowry, S. C., Lyon, I., Magni, G., Mall, U., Mann, I., Markiewicz, W., Martins, Z., Marette, M., Meierhenrich, U., Mennella, V., Ng, T. C., Nittler, L. R., Palumbo, P., Pätzold, M., Prialnik, D., Rengel, M., Rickman, H., Rodriguez, J., Roll, R., Rost, D., Rotundi, A., Sandford, S., Schönbächler, M., Sierks, H., Srama, R., Stroud, R. M., Szutowicz, S., Tornow, C., Ulamec, S., Wallis, M., Waniak, W., Weissman, P., Wieler, R., Wurz, P., Yung, K. L. & Zarnecki, J. C. Triple F - A Comet Nucleus Sample Return Mission. Experimental Astronomy , 23 (3) , pp. 809-847. Springer . DOI: 10.1007/s10686-008-9115-8. ISSN 0922-6435 (2009).

Tagungsbeiträge

- Gortsas, N., Kührt, E., Motschmann, U. & Keller, H. U.: New thermal model of the sub-surface layer of comets. (Vortrag) 39. American Astronomical Society Division for Planetary Sciences (DPS), Orlando/Florida (2007).
- Kührt, E. & Gortsas, N.: Cometary activity - new data, new questions. (Vortrag) OSIRIS Co-I meeting, Venedig/Italien (2007).
- Gortsas, N., Kührt, E. & Motschmann, U.: Numerische Modellierung von Kometen-Vom Nukleus zur Plasmaumgebung. (Vortrag) Oberseminar für Theoretische Physik, TU Braunschweig, Braunschweig (2008).
- Kührt, E., Gortsas, N. & Motschmann, U.: Thermophysical modeling of cometary nuclei with moving ice boundaries. (Vortrag) Science of Solar System Ices, Oxnard/California (2008).
- Gortsas, N., Kührt, E. & Motschmann, U.: Numerical studies of surface erosion in a multi-component comet nucleus. (Vortrag) 10. Asteroids, Comets, Meteors Meeting (ACM) Baltimore/Maryland (2008).
- Gortsas, N., Kührt, E. & Motschmann, U.: Thermophysical model of the production rate of comet C/1995 O1 (Hale-Bopp). (Vortrag) Thermal Models of Planetary Science, Nizza/France (2008).
- Gortsas, N., Motschmann, U., Kührt, E., Knollenberg, J., Simon, S., Bösswetter, A., Wiehle, S. & ISSI Comet Modeling Team.: Mapping of coma anisotropies to plasma structures of 67P/Churyumov-Gerasimenko during its way to the Sun. (Vortrag) 25. Rosetta Science Working Team Meeting, ESOC, Darmstadt (2008).
- Gortsas, N., Kührt, E. & Motschmann, U.: A novel thermophysical model of the production rate of C/1995 O1 (Hale-Bopp). (Vortrag) European Geosciences Union, General Assembly 2009, Wien/Österreich (2009).
- Gortsas, N., Motschmann, U. & Kührt, E. (2009) Hybrid plasma simulation studies of coma anisotropies. (Vortrag) European Geosciences Union, General Assembly 2009, Wien/Österreich (2009).

Contents

1 Introduction

The European Space Agency's (ESA) Rosetta mission to comet 67P/Churyumov-Gerasimenko (hereafter CG) was launched from Kourou in French Guyana on an Ariane 5 launcher on March 2, 2004. The Rosetta mission is an international cooperative project between ESA, various European national space agencies, and NASA. The Rosetta space craft consists of the Rosetta orbiter and the Rosetta lander Philae. It is designed to perform a series of experiments at the comet and on its surface as described in Glassmeier et al. (2007). These experiments are going to provide a unique insight into the state and evolution of comets addressing one of the prime scientific objectives of the Rosetta mission which is to learn more about the origin of the Solar System by studying the origin of comets (Schwehm and Schulz 1999). The Rosetta mission is going to broaden our knowledge of comets in particular and the Solar System in general together with previous in-situ missions to comets like the flyby of the ICE space craft at 21P/Giacobini-Zinner, the two Vega missions and Suisei who encountered 1P/Halley, the Giotto flybys at 1P/Halley and 26P/Grigg-Skjellerup, the Deep Space 1 mission to 19P/Borrelly, the Star Dust mission to comet 81P/Wild 2, and the recent mission Deep Impact to comet 9P/Tempel 1.

Active comets belong to the brightest and most impressive objects in the Solar System. As comets approach the Sun they warm and eject gaseous and dust material into space forming a surrounding structure referred to as coma. Depending on cometary activity the coma can reach the size of the Sun with spatial extensions in the order of 10^5 to 10^6 km. Besides their coma comets are also known for the elongated tail which can reach up to 1 AU. In general, the tail consists of the plasma tail directed in anti-sunward direction and the broad and curved dust tail.

Among the questions one hopes to enlight by studying comets is the question related to Solar System formation 4.6 billion years ago. As Charnley and Rodgers (2008) reviewed current theories tell us that the Solar System formed from the collapse of an interstellar gas and dust cloud. A small fraction of the solid matter survived the earliest stages of planet formation and could be the building blocks of comets (Blum and Wurm 2008, Fernández 2007). Information about the conditions at the time of comet formation could be deduced if the structure and the composition of comet nuclei remained unchanged since the time of formation. Possible links between comets and the interstellar medium could be drawn if comets consist at least some ingredients from this source as argued by Charnley and Rodgers (2008). If presolar grains are detected in comet nuclei a link between interplanetary dust particles and comets could be established. The former are studied extensively in laboratories and could indicate that circumstellar grains are a reservoir of comet material as discussed by Hoppe (2007). These information would possibly help to distinguish among different models related to Solar System formation. The result would be a model telling us how the Solar System and eventually Earth and live on Earth might

have formed. A contribution to questions that have interested mankind ever since.

Among the questions cometary research tries to answer in this context is how pristine comets really are. The predominant species in the coma of comets is water but also more volatile species like NH_3, CO_2, CO, NH_2 and N_2, and many more have been observed. The fact that comet nuclei include such volatile species indicates that they must have formed in cold regions beyond the snow line in the protoplanetary disk. Their chemical composition might enable to trace their origin to certain regions in the protoplanetary disk. Comets are therefore considered to be the most pristine bodies in the Solar System. In contrast to Asteroids which are rocky objects and in most cases depleted in water or other volatile species showing no outgassing activity comparable to comets. Recently, this picture appeared to have been questioned by the Star Dust mission to comet 81P/Wild 2. Examination of samples from the Star Dust mission indicate a relative high amount of silicates that were formed at high temperatures which was not expected as reviewed by Burchell and Kearsley (2009). Stadermann et al. (2008) conclude that a significant amount of material in Wild 2 must be from the inner Solar System. A transport mechanism needs to bring these materials either at the time of comet formation or before to the outer Solar System. Another more simple explanation was given in Burchell and Kearsley (2009). There might be no gap between regions of asteroid formation and of comets which could lie just within a snow line allowing for the incorporation of ices. Such comets would be close enough to the Sun to incorporate high temperature silicates. Subsequent scattering by the giant planets could bring those comets to the outer Solar System. Despite these results Fernández (2007) pointed out that the elemental composition of comets indicate that these objects might be the most primitive unprocessed bodies of the Solar System. The low bulk density of comets estimated for instance by Davidsson and Gutiérrez (2005) and the tensile strength as argued by Trigo-Rodriguez and Blum (2009) corroborate this conclusion. Thereby, comets offer a window into the early stages of Solar System formation.

Thermal modeling of comets contribute to these questions by providing a framework to understand cometary activity and to calculate temperature depth profiles. Cometary activity is calculated based on assumptions on the composition and the structure of comet nuclei. Matching theoretical production rates to observations allows to constrain important parameters. The distribution of volatile species in the nucleus can be deduced from the temperature depth profiles allowing to infer how processed a comet nucleus is. In addition, thermal models are important to interpret the expected data from ESA's Rosetta mission. Among many other experiments the temporal and spatial characteristics of activity and temperature profiles beneath the surface are going to be measured.

Numerous thermal models have been developed in the past three decades with differing degree of complexity. Most thermal models account for gas diffusion and assume the existence of amorphous ice with trapped gases. Two independent groups were able to interpret the extensive set of production rates for the super volatile species CO of comet C/1995 O1 (Hale-Bopp) by assuming the presence of amorphous ice with varying amount of trapped CO gas which is released upon phase transition from amorphous to crystalline ice. Several leading groups dedicated to the thermal modeling of comets and other minor bodies gathered for an International Space Science Institute (ISSI) project at Bern/Switzerland to run simplified cases. This project is very important for thermal modeling of comets as it has posed many questions on the numerical and physical model

of the thermal evolution of comets. Rather large differences in the maximum surface temperature have been obtained for the most simple test case - a pure water ice comet - as reported by Huebner et al. (1999) and Huebner et al. (2006).

The employed, until now not verified, assumption of amorphous ice to successfully interpret the CO data of comet Hale-Bopp and the fact that large differences for the most simple test case of a comet in the comparative study among the leading thermal modeler groups have stimulated the development of a novel thermal model as part of this doctoral thesis. The model solves the heat and mass transfer problem of comets. Heat conduction, heat advection, gas diffusion, sublimation, and condensation are considered like previous models. In addition, surface erosion due to surface sublimation is properly accounted for. Numerically, this problem leads to moving boundaries which are taken into account by following well known numerical methods and which are often referred to as Stefan problem. The model is first applied to interpret the water and CO measurements of Hale-Bopp without assuming the presence of amorphous ice. Then the model is applied to predict the water and CO activity of comet CG in addition to the calculation of temperature depth profiles in preparation of the Rosetta mission.

On their journey into the inner Solar System comets are also subject to the solar wind - a plasma flow with a frozen-in magnetic field. The plasma environment of CG is investigated in the second part of the doctoral thesis. The solar wind-comet (SW-C) interaction leads depending on the outgassing strength of the comet and other parameters to the formation of characteristic plasma structures like the bow shock and the ion composition boundary and additional sharp transitions giving the impression of a multi-layered interaction region. Comets provide a unique laboratory to study the interaction of an extended *soft* obstacle, the coma of the comet, and a supersonic and super-Alfvénic plasma flow. The characteristic scales in temporal and spatial dimension make it necessary to apply a hybrid simulation model to study the SW-C interaction in order to resolve the gyromotion of the solar wind protons and cometary ions which are to a large extend responsible for the formation of the plasma structures. Besides the theoretical interest in studying the SW-C interaction such simulations provide insight in the nature and size of the interaction of the solar wind with a weakly outgassing comet. These information allow to prepare missions like the Rosetta mission to gain the largest scientific output.

The doctoral thesis consists of two parts. In Chapter 2 the thermophysical model is presented and in Chapter 3 tested. Then, the thermal model is applied to study the water and CO activity of comet Hale-Bopp in Chapter 4. The investigation of this comet is particularly important since this comet represents a kind of a reference comet as it has been extensively studied by Earth and space based instruments. In Chapter 5 which is the last chapter of the thermal part the model is applied on comet CG. In this Chapter the role of the Stefan problem is thoroughly investigated and temperature depth profiles are discussed. The second part of the thesis starts with Chapter 6 in which the hybrid model is presented. Chapter 7 is then devoted to the study of coma anisotropies of comet CG while in Chapter 8 the perihelion approach of comet CG is simulated for a single cometary ion species. The model is then extended in Chapter 9 to include a second cometary ion species, e.g. CO. A summary is given in Chapter 10.

2 Thermal model

2.1 Previous thermal models of comets

The thermal evolution of comets has been studied in various forms by several research groups after 1950 when Whipple (1950) proposed the icy-conglomerate model of comet nuclei, when Oort (1950) identified the Oort cloud as a reservoir of comets, and when Biermann (1951) correctly interpreted the plasma tail of comets to be the result of the solar wind-comet interaction. More recently, Prialnik (2006) gave a list of active modeler groups consisting of 11 entries indicating the broad interest in comets even to this day.

In the 1980's most thermal models treat the nucleus as a compact mixture of ice and dust with no bulk sublimation. The models of Weissman and Kieffer (1981), Kührt (1984), Prialnik and Bar-Nun (1987), Kührt and Keller (1994), and Julian et al. (2000) belong to this class. Around the transition from the 1980's to the 1990's thermal models based solely on the thermal conduction equation were extended to include parametrically the contribution of gas vapor through an effective thermal conductivity. This extension was stimulated by results obtained from ESA's Giotto mission to 1P/Halley. Rickman (1989) estimated the mass density of 1P/Halley to be in the ranges of 280 to 650 kg m^{-3} which lead to the conclusion that cometary nuclei had to be porous. The contribution of bulk sublimation and subsequent gas diffusion is indirectly employed in the derivation of the effective heat conductivity. A key assumption is that saturation pressure prevails at all depths and also at the surface. This approach was followed by Steiner et al. (1991), Kossacki et al. (1994), Kossacki et al. (1997), and Kossacki et al. (1999). In the early 1990's a new class of thermal models were devised which solved the coupled heat and mass transfer problem. This approach was empirically motivated by the results of Spohn and Benkhoff (1990) obtained during the KOSI experiments at the DLR in Cologne/Germany. While the boundary condition for the heat conduction equation is almost in all models besides few modifications the same the gas diffusion equation made it necessary to specify appropriate boundary conditions. A zero surface pressure is an assumption employed in such models by Mekler et al. (1990), Prialnik (1992), Prialnik et al. (1993), Podolak and Prialnik (1996), Enzian et al. (1998), Enzian (1999), and Orosei et al. (1999). Fanale and Salvail (1984), Spohn and Benkhoff (1990), de Sanctis et al. (1999), and Capria et al. (2001) employed the assumption that saturation pressure prevails at the surface. Specifying reasonable boundary conditions is very important but difficult to formulate. Rickman and Fernandez (1986), Rickman et al. (1990), Espinasse et al. (1991), Tancredi et al. (1994), Orosei et al. (1995), Capria et al. (1996), and Enzian et al. (1997) employ the conservation of the outgoing mass flux as boundary condition for the gas diffusion equation. The models of Tancredi et al. (1994), Huebner and Markiewicz (2000), and Davidsson and Skorov (2002) tried

to correct the upper boundary condition of the gas diffusion equation for the molecular back flux due to a non-maxwellian velocity distribution at the surface of the nucleus. In the model of Skorov et al. (2001) the macroscopic gas diffusion equation is replaced by a kinetic description of the sub-surface mass flow. In these models either Monte Carlo simulations of molecular migration or analytical approximations such as Clausing transmission probability functions are employed. In the last couple of years, thermal models were devised to calculate the thermal evolution of comets in 3 dimensions. Rosenberg and Prialnik (2007) presented a fully 3 dimensional model which is applied to study dust mantle formation in Rosenberg and Prialnik (2009). To simplify the calculations it is assumed that the gas subliming in the interior of the nucleus escapes to the surface with no time-delay. 3 dimensional codes allow to take into account the lateral heat flow at the surface and in the interior of the comet. They might also provide a mean to investigate surface structures and non-spherical cometary shapes. As for all thermal models the thermal conductivity is a key parameter to judge the importance of such models. Unfortunately, this parameter is not well constrained. But in connection with the Rosetta mission such models might turn out to be very useful.

The contributions of some research groups have been concentrated as part of an International Space Science Institute (ISSI) project to discuss and compare thermal models of comets. The aim was to establish a reference model against which future models could be tested. The project published in Huebner et al. (2006) results of the comparison of three and in some calculations five research groups. The groups ran a number of test cases for simple nucleus models. It turned out that even for quite simple models like a pure water ice sphere the deviations among model results where quite substantial. Compared to a previous publication by Huebner et al. (1999) the results in Huebner et al. (2006) have not much improved. At aphelion there was a deviation in the maximum surface temperature for a pure water ice sphere up to 10 K. The authors attributed the differences mainly on the treatment of the thermal gradient in the upper boundary condition of the thermal conduction equation without going into details of how the thermal gradient is calculated numerically. In addition, the authors mention that strong surface erosion might be responsible for the large deviations in the maximum surface temperature without giving an outline how erosion is defined and how it is calculated. Despite these strong deviations the project is very important for thermal modeling of comets as it gathers the experience of several research groups. Future modeling efforts can rely on this compendium and work towards an improvement of the models. The project has also demonstrated how difficult and complex thermal modeling of comets really is.

As part of this thesis the effect of surface erosion on the thermal state of the nucleus is investigated. Many groups calculated as part of their models the amount of erosion but they have not or only roughly considered what effect erosion due to sublimation has on the thermal state of the nucleus (Benkhoff and Huebner 1995, Enzian et al. 1998, de Sanctis et al. 1999, Orosei et al. 1999). Surface erosion due to sublimation leads to escaping surface material, and thus also to material that was previously heated. The internal energy stored therein is lost obstructing the penetration of the nucleus by the diurnal heat wave. In the literature, these kind of moving boundary value problems are called ablation problems. They constitute a special type of Stefan problems (SPs), which are named in remembrance of the early work of Stefan (1891) on moving boundary value problems in connection with the solidification of water. Since then, many articles have been devoted

to theoretical and more applied investigations of moving boundary value problems (Ockendon and Hodgkins 1975, Crank 1984). Douglas and Gallie (1955) published an article introducing the notion of a variable time step which is chosen such as to secure that at each time step the moving boundary is located on a grid node. Later, Murray and Landis (1959) introduced a technique characterized by a variable spatial discretization size and a fixed number of discretization points so that at each time step the moving boundary is located on a grid node. While these methods belong to the class of variable front tracking methods, Crank and Gupta (1972) proposed a method in which the spatial discretization size is kept constant but the grid is redrawn according to the movement of the boundary. The values of the field quantities are then obtained through interpolation. The textbook of Crank (1984) provides a good introduction into the field of moving boundary value problems. More recently, in the research field of thermal modeling of minor bodies in the Solar System moving boundary value techniques have been applied to study various scenarios. Merk et al. (2002) applied the method of Murray and Landis (1959) for the moving boundary to study the ^{26}Al-induced radioactive melting of Asteroids considering accretion. The same method concerning the movement of the boundary has been incorporated in the models of Merk and Prialnik (2006), which are devoted to question of the existence of liquid water in trans-Neptunian objects. Gortsas et al. (2007) incorporated the method of Crank and Gupta (1972) to study the impact of surface erosion on the thermal state of the nucleus and on cometary activity. Prialnik and Merk (2008) developed a new code treating the movement of the boundary according to the Murray and Landis (1959) method. They study growth and evolution effects of Kuiper belt objects and Enceladus.

Whether moving boundary value techniques have been applied in other models than those just cited and which were not applied to the modeling of cometary activity is very difficult to judge. In a more numerical oriented publication Prialnik (1992) described very briefly in the appendix that the number of grid points decrease as the ice at the surface sublimates. No further details like in the publication of Prialnik and Merk (2008) were given. How the movement of upper boundary is treated is not described in a review article of thermal modeling of comets in Prialnik et al. (2004) nor in an ISSI publication devoted to the modeling of heat and gas diffusion in comet nuclei by Huebner et al. (2006). Although, one reason for the large deviations among different thermal models for a pure water ice sphere in Huebner et al. (1999) and in Huebner et al. (2006) have been attributed to the thermal gradient at the surface. But it is clear that the numerical treatment of the moving boundary impacts the thermal gradient at the surface.

To conclude, either the movement of the upper boundary was not taken into account. Or if it was taken into account it might have been modeled with a method that is not so sophisticated as the one presented in this thesis and as those methods used in the above cited recently published articles which were not applied to study cometary activity. Another possibility would be that the thermal conduction coefficient was so large that the obstruction of the diurnal heat wave could be neglected. Thermal conduction coefficients around 1 W $K^{-1}m^{-1}$ and higher were quite common before the recent results of Groussin et al. (2007) in connection with the Deep Impact mission to 9P/Tempel 1.

In this thesis the approach of Gortsas et al. (2007) and Gortsas et al. (2008) is followed to investigate systematically the effect of surface erosion due to sublimation of ices on the thermal state of the nucleus and on cometary activity. The SP of comets is formulated and solved. The movement of the fixed grid and the interpolation technique with cubic

splines is taken from Crank and Gupta (1972). In extension to that, a non-constant number of intervals is introduced in order to be able to calculate oscillating boundaries which can come very close to the surface. This adaptive approach is essential to model cometary activity of a multi-component nucleus.

It will be shown that the SP is important if the internal energy of the eroded surface layers cannot be neglected compared to the energy transported into the nucleus by the thermal heat wave. Therefore, the relevance of the SP depends on the sublimation rate and on important parameters like heat conductivity, density, specific heat, and diurnal rotation period.

2.2 Characteristic scales of surface erosion

Before the presentation of the model the characteristic scales of surface erosion are estimated and compared with the characteristic scales of the diurnal heating of the rotating nucleus. A pure water ice sphere shall be considered at perihelion. The incoming solar energy is in this case consumed almost completely by water ice sublimation. Therefore, the solar flux F_S equals the water ice sublimation energy flux $Q(T_0)$ with T_0 being the surface temperature, it yields in W m^{-2}

$$F_S(r_H) = Q(T)\,. \tag{2.1}$$

r_H denotes the heliocentric distance. Sublimation of water ice at the nucleus surface leads to loss of material. The velocity v_e of this erosion process is mainly given by the mass flux $Z(T) = Q(T)/\Delta H$ in kg m^{-2} s^{-1} with ΔH denoting the latent heat of sublimation. According to Stefan (1891) v_e is given by

$$v_e = \frac{Z}{\rho_i}\,. \tag{2.2}$$

Taking, what can be considered to be a typical value for the mass density ρ_i of water ice at comets (460 kg m^{-3} with a porosity of 0.5), yields an erosion velocity of about

$$v_e \approx 10^{-6} m s^{-1}\,. \tag{2.3}$$

The other parameter values can be found in Table 2.1.

The diurnal rotation of the comet leads to a quasi periodic signal entering the nucleus through the upper boundary. For a homogeneous body in a quasi-stationary state the propagation velocity of the diurnal wave is given by

$$v_p = \sqrt{\frac{4\pi\,\kappa}{\rho_i\,c\,\tau_r}}\,. \tag{2.4}$$

κ, c and τ_r are the thermal conduction coefficient, the specific heat capacity and the diurnal rotation, respectively. The propagation velocity is calculated for a κ value of 10^{-3} W m^{-1} K^{-1} which is in good agreement with recent observations in connection with the Deep Impact mission to 9P/Tempel 1 as reported by Groussin et al. (2007). The mass density

Table 2.1: Basic parameters employed in the simulation of Hale-Bopp and CG.

Quantity	Symbol	Value	Unit
Density of water ice	ρ_i	917	kg/m^3
Specific heat of water ice	c_i	1610	J/(kg K)
Specific heat of water gas	$c_{g,i}$	1370	J/(kg K)
Pressure constant water ice	A_i	3.56×10^{12}	Pa
Temperature constant water ice	B_i	6141.667	K
Thermal enthalpy of water ice	ΔH_i	2.84×10^6	J/kg
Density of CO ice	ρ_{co}	1250	kg/m^3
Specific heat of CO ice	c_{co}	2010	J/(kg K)
Specific heat of CO gas	$c_{g,co}$	720	J/(kg K)
Pressure constant CO ice	A_{co}	1.2361×10^9	Pa
Temperature constant CO ice	B_{co}	764.16	K
Thermal enthalpy of CO ice	ΔH_{co}	0.227×10^6	J/kg
Density of dust	ρ_d	3000	kg/m^3
Specific heat of dust	c_d	1300	J/(kgK)
Emissivity	ϵ_{em}	0.96	
Bond Albedo	$\mathcal{A}$	0.04	

of water ice has a value of 460 kg m^{-3} while the other parameters can be found in Table 2.1. As a result the propagation velocity has a value of

$$v_p \approx 6 \times 10^{-7} ms^{-1} \tag{2.5}$$

which is below the erosion velocity

$$v_p < v_e \,. \tag{2.6}$$

Hence, at perihelion erosion of surface material can be much faster then time necessary to conduct thermal energy into the body if a low thermal conductivity in the order of 10^{-3} W m^{-1} K^{-1} is employed. A dimensionless constant χ, called penetration number, is introduced to distinguish easily between different regimes

$$\chi = \frac{v_e}{v_p} = Z \sqrt{\frac{c\tau}{4\pi \rho_i \kappa}} \,. \tag{2.7}$$

For the example given above the penetration number χ has a value of 1.67. Is the penetration number $\chi > 1$, then surface erosion dominates the thermal evolution of the comet and the heat transport through the surface must be treated as a moving boundary value problem. Is the penetration number $\chi \ll 1$, then continuous heating due to a fast penetration of the nucleus by the diurnal wave is dominating the thermal evolution of the comet.

Table 2.2: The penetration number χ is listed as function of the thermal conductivity. A porosity of 0.5 corresponding to a mass density of water ice of 460 kg m^{-3} was used. The remaining constants can be found in Table 2.1.

Thermal cond. κ [W m^{-1} K^{-1}]	10^{-1}	10^{-2}	10^{-3}
Penetration number χ	0.17	0.53	1.67

In this case, the penetration number suggests that it is save to neglect the Stefan problem in thermophysical modeling of comets. At least, this is the conclusion one can draw from this simple consideration of the characteristic scales. If this is also the case in the numerical solution of the problem will be discussed later. The equation of the penetration number χ, Eq. (2.7), shows that the movement of the upper boundary becomes important for high sublimation rates, slow spin motion, low thermal conductivity and ice density. In Table 2.2 the penetration number χ as function of the thermal conductivity κ is listed. Stimulated from these considerations a thermal model based on the Stefan problem which is able to solve the heat- and mass transfer problem in an eroding cometary nucleus with strict conservation of energy is developed.

2.3 Kepler Orbit

The thermal evolution of comets depends on the orbit around the Sun. In this thesis two comets with different orbits have been studied. Comet CG has a close elliptic orbit while Hale-Bopp has an almost parabolic orbit with an eccentricity e of almost 1. In this section the methods employed to calculate the orbit of the comet shall be presented and discussed.

For thermal modeling it is important to know the radial distance r_H in a heliocentric coordinate system as function of time. Depending on the degree of accuracy needed there are different approaches to solve this problem. In thermal modeling of comets the celestial mechanics equations for the radial distance to the Sun r_H and the the time-of-flight coordinate t are solved

$$\begin{aligned} t - t_0 &= \sqrt{\frac{a^3}{M_S}}\Big(E - e\sin(E)\Big) \\ r_H &= a\Big(1 - e\cos(E)\Big). \end{aligned} \tag{2.8}$$

t_0, a, E, M_S denotes the time of perihelion passage, the semi-major axis, the eccentric anomaly, and the mass of the Sun, respectively. The derivation of these equations should not be given here but can be found in Bate et al. (1971). These equations need to be complemented by a relation for the true anomaly α

$$\cos\alpha = \frac{a}{r_H}\Big(\cos(E) - e\Big). \tag{2.9}$$

While the calculation of CG's orbit should be of no great problem, this is no longer true for comet Hale-Bopp. This comet has a very eccentric orbit. As pointed out in Bate

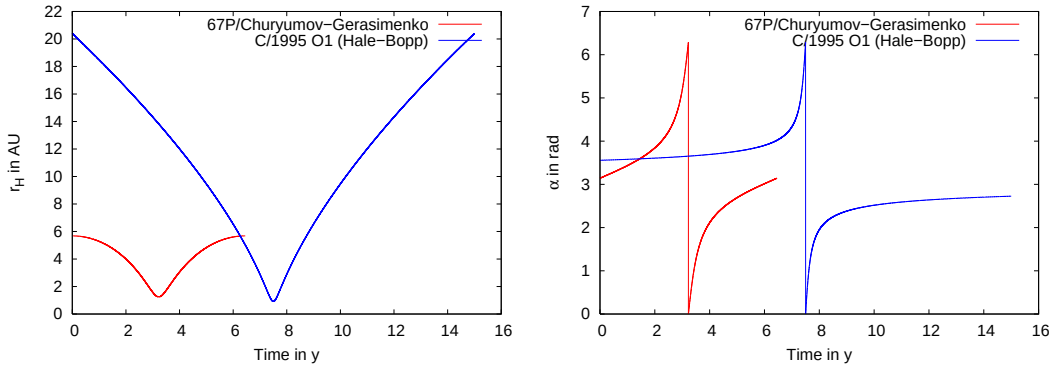

Figure 2.1: Left: Heliocentric distance r_H as function of time for CG and Hale-Bopp as employed in this thesis. For the former comet the whole orbit is calculated. The orbit of Hale-Bopp is considered only up to 20 AU from the Sun as the thermal evolution of the nucleus is determined when the nucleus is close to the Sun. Right: The true anomaly α for these two comets. The calculations are started at aphelion for CG and at 20 AU preperihelion in case of Hale-Bopp.

et al. (1971) a significant loss of numerical accuracy occurs if near-parabolic orbits are calculated with the classical Kepler equations. Special solutions have been devised for this problem. In models of cometary activity the accuracy of the orbit is, however, not a main issue for the result. Other parameters influence the simulation results more significantly. Therefore, the Kepler equations have been also used to calculate the orbit of Hale-Bopp in the range of -20 AU pre- to 20 AU postperihelion. In Fig. 2.1 the orbits and the true anomaly of CG and Hale-Bopp are displayed as function of time.

2.4 Thermal model

After having calculated the orbit of the comet the focus turns to the processes in and at the surface of the nucleus. In a volume element energy is transported through heat conduction of the ice matrix, heat advection of the vapor, and sublimation or condensation processes in the pores. A theoretical description of these processes starts with the general formulation of conservation laws of mass, momentum, and energy as appropriate for comets. Mass conservation is expressed through a balance equation for the vapor mass density ρ_μ and the solid ice mass density ρ_μ^s of species μ

$$\frac{\partial \rho_\mu}{\partial t} + \nabla(\rho_\mu u_\mu) = -\frac{\partial \rho_\mu^s}{\partial t}\,. \tag{2.10}$$

and

$$\frac{\partial \rho_\mu^s}{\partial t} = -q_\mu\,. \tag{2.11}$$

x and t denote the spatial and temporal coordinates. u_μ denotes the diffusion velocity of the μ volatile component. The source term q_μ defines bulk evaporation. Following Mekler et al. (1990) it can be calculated as the difference between the gas density ρ_μ of species μ

in the pores and the equilibrium state $\rho_{\mu,eq}$ at some bulk temperature T

$$q_\mu = f_p\,(\rho_{\mu,eq} - \rho_\mu)\,c_{th,\mu}(T)\,. \tag{2.12}$$

Here $c_{th,\mu}$ denotes the mean thermal velocity of the μ gas species and f_p is a factor that depends on structural properties of the comet, e.g. $f_p = 2\,\psi/r_p$ with ψ being the porosity and r_p the effective pore radius. It is assumed that the gas temperature equals the temperature of the bulk material. In this model the pores are modeled as cylindrical capillaries whose circular cross-section has a diameter of $2\,r_p$ as Mekler et al. (1990) proposed. The $\rho_{\mu,eq}$ is given by the vapor pressure which is calculated with the Clausius-Clapeyron equation and the assumption that the gas obeys the ideal gas law

$$\rho_{\mu,eq} = \frac{P_{v,\mu}\,m_\mu}{k_B\,T}\,. \tag{2.13}$$

The saturation pressure $P_{v,\mu}$ is given according to the empirical formula of Fanale and Salvail (1984) as $P_{v,\mu}(T) = A_\mu \exp(-B_\mu/T)$. The values of the constants can be found in Table 2.1. An implicit assumption of this approach is that there is bulk ice in the pores so that the reference state can prevail.

The mean free path of molecules exceeds the characteristic length scales of a porous nucleus, e.g. the lengths characterizing the structure of the pores. Therefore, the Knudsen number is much larger then 1. In this case the vapor velocity field can be calculated from the Knudsen formula

$$\rho_\mu u_\mu = -C_\mu \frac{\partial}{\partial x}(\rho_\mu \sqrt{T})\,. \tag{2.14}$$

C_μ is a factor that can be related to structural and thermal parameters (Benkhoff and Spohn 1991), e.g. $C_\mu = 2\,\psi\,r_p\,c_{th,\mu}$.

Equation (2.10) and (2.14) describe the diffusion of vapor inside a predefined porous structure in a macroscopic model. The conservation of energy written in terms of temperature under the assumptions of a Fourier type heat flux, the advection of energy through vapor flow, and an energy source term reads as, see e.g. Spohn and Benkhoff (1990),

$$c\,\rho\,\frac{\partial T}{\partial t} + \sum_\mu c_{g,\mu}\,\rho_\mu\,u_\mu \frac{\partial T}{\partial x} = \frac{\partial}{\partial x}\kappa\frac{\partial T}{\partial x} - \sum_\mu \Delta H_\mu q_\mu\,. \tag{2.15}$$

$c_{g,\mu}$ denotes the specific heat of vapor of the μ species. It is calculated by assuming the validity of the ideal gas law for water and CO vapor. Dust enters the model via $c\rho = \sum_\mu c_\mu\,\varrho_\mu\,\phi_\mu$. Here ϱ_μ and ϕ_μ denote the bulk ice density and the volumetric filling factor of species μ.

The description is one dimensional with respect to the processes taking place inside the nucleus. But the boundary condition accounts for different irradiation patterns which allows to consider active surface areas throughout the comet surface. The one dimensional description is justified because the lateral components of the thermal flux are assumed to be small compared to the radial flux, see also the discussion below on the thermal conduction coefficient. In addition, processes related to cometary activity are believed to be confined in the range of few cm to meters. This is small compared to the radius of a comet of several km size. Therefore, it is safe to employ the plane parallel approximation when surface features, i.e. sharp edges, are neglected.

2.5 Thermal conduction coefficient κ

Energy transport through heat conduction in the ice matrix is described by the first term on the right hand side of Eq. (2.15). Its contribution to the energy budget heavily depends on the choice of the thermal conduction coefficient κ which describes energy transport in the solid phase (grains and ices). It depends on the structure and composition of cometary material and it is sometimes assumed to be temperature dependent. Hence, there are many different approaches to this problem. Some authors introduce geometric parameters others take also the bonds between the grains into account to develop analytical models for κ as outlined in Seiferlin (1991). Smoluchowski (1982) proposed to use classical Maxwell equations employing the analogy between heat conduction in a porous ice matrix and electrical conduction in a network of resistance to arrive at an analytical expression of κ. Steiner et al. (1991),however, discussed the restricted applicability of Maxwell's formula.

Another rather widely used approach is to introduce the Hertz factor defined as the ratio of the contact area A_c between grains to the mean cross section of a grain A_s. This parameter has been used in Squyres et al. (1985) and in Kossacki et al. (1994) to correct the heat conductivity of compact ice which depends according to Klinger (1981) on the reciproce of the temperature. Espinasse et al. (1991), Prialnik (1992), Tancredi et al. (1994), and Enzian et al. (1998) are among authors who employed the temperature dependence of κ. The Hertz factor, however, is not well constrained. Laboratory measurements yield a wide range between 10^{-1} to 10^{-3} for the Hertz factor as discussed in Huebner et al. (2006). More recently, this approach has been employed also in Davidsson and Skorov (2002) who used the code of Steiner et al. (1991) to calculate light absorption of surface layers. The Hertz factor is also employed in thermal model calculations of Sanctis et al. (2010). Some authors also include radiative heat transfer to κ but at temperatures typical for comets it can be neglected. Steiner and Koemle (1991) presented an approach to add the heat transport by vapor flux through the pores to the thermal conduction coefficient κ. Thus reducing the coupled heat and mass transfer problem to a heat transfer problem with an effective heat conductivity.

On the experimental side, there are studies of the thermal conductivity of porous ice in connection with comets. For a review on various measurements, especially for water ice phases, consult Seiferlin et al. (1996) and Seiferlin (1991) and the bibliography therein.

To conclude many unsolved questions like the existence of amorphous ice or the porosity and pore size distribution in cometary nuclei make it difficult to derive realistic values. Laboratory measurements (Spohn et al. 1989, Seiferlin 1991, Grün et al. 1993, Stöffler et al. 1991) generally suffer from the widely unknown structure and composition of cometary matter and may not be representative. Therefore, in this thesis the thermal conduction coefficient is kept constant and its value has been chosen in accordance to what is currently known based on recent observations of and missions to comets (Groussin et al. 2007). This approach reflects the current state of knowledge on the heat conductivity of comets as also stated by Huebner (2008) and it allows to keep the number of free parameters low. A non-constant thermal conduction coefficient can be incorporated into the model by reimplementing the subsystem devoted to the solution of the thermal conduction coefficient and by making small changes in the subsystem devoted to the calculation of the upper boundary condition.

2.6 Characteristic time scales

Performing a thorough analysis of the relevant time scales allows to neglect the temporal variations of the vapor mass density in Eq. (2.10) as proposed by Spohn and Benkhoff (1990). The analysis is carried out for water vapor but is equally applicable to CO vapor. The μ index is therefore dropped. The characteristic time scales of heat conduction τ_h and gas diffusion τ_g can be expressed as

$$\tau_h = \frac{L^2 \rho\, c}{\kappa} \tag{2.16}$$

and τ_g as

$$\tau_g = \frac{L^2}{C\,\sqrt{T}}\,. \tag{2.17}$$

L denotes a characteristic length scale of the problem. It cannot exceed the mean free path of the vapor molecules because then the flow is deviating from the free molecular flow regime. In case that the pores are modeled to be cylindric tubes L describes the length of the pores while the previously introduced pore radius r_p describes the radius of their cross section.

All quantities in Eq. (2.10) are scaled to dimensionless quantities which are indicated by a * superscript. Time is referred to the heat time scale $t^* = t/\tau_h$ which is the time scale of the heat conduction equation. This choice enables to judge the importance of the time derivative of the mass density from the time scale of the heat conduction problem. x is scaled to L, e.g. $x^* = x/L$. The vapor density is scaled to an equilibrium value at the surface temperature of a water ice covered comet at perihelion $\rho^* = \rho/\rho_{eq}$. The velocity field is scaled to the thermal velocity at the surface temperature at perihelion, e.g. $u^* = u/c_{th}$. The mass source term which describes the change of vapor density with time is scaled to the ratio of the vapor density reference value ρ_{eq} and the time scale of gas diffusion τ_g, e.g. $q^* = q\,\tau_g/\rho_{eq}$. Mapping of Eq. (2.10) to dimensionless quantities yields then to

$$\frac{\tau_g}{\tau_h}\frac{\partial \rho^*}{\partial t^*} + \frac{\tau_g\, c_{th}}{L}\,\frac{\partial(\rho^*\, u^*)}{\partial x^*} = q^*\,. \tag{2.18}$$

Entering the expressions of the characteristic scales leads to

$$\frac{\kappa}{\rho\, c\, 2\psi\, c_{th}}\frac{1}{r_p}\frac{\partial \rho^*_\mu}{\partial t^*} + \frac{1}{2\psi}\sqrt{\frac{L^3}{r_p^3}}\,\frac{\partial(\rho^*_\mu\, u^*_\mu)}{\partial x^*} = q^*_\mu\,. \tag{2.19}$$

The coefficient of the time derivative is only significant for very small pore radii, e.g. $r_p < 10^{-8}$m. For typical pore sizes of comets in the range of few to 100 μm it is thus safe to neglect the temporal variations of the vapor density. Therefore the following equation for the gas species is solved

$$\nabla(\rho_\mu u_\mu) = f_p\,(\rho_{\mu,eq} - \rho_\mu)\, c_{th,\mu}(T)\,. \tag{2.20}$$

2.7 Boundary conditions

The evolution equations of the nucleus needs to be supplemented by appropriate initial and boundary conditions. At the surface of the comet, a balance equation is commonly

employed. The main energy source of comet nuclei is the solar energy. It depends on the radial distance of the comet from the Sun r_H and the orientation of a surface area relative to the sun. The latter is modeled with the solar zenith angle ζ. This energy is distributed among several processes taking place at the surface. As the bulk material of the comet has a certain temperature thermal re-radiation due to the Stefan-Boltzmann law emits part of the incoming solar energy. The emissivity of the comet is reduced by the emissivity coefficient ϵ_{em} which is usually set equal to $1 - \mathcal{A}$ with $\mathcal{A}$ being the Bond albedo. The surface is coupled to the nucleus interior via the thermal flux. The value of this quantity depends heavily on the thermal conductivity κ. Depending on the sign of the temperature gradient energy is exchanged between the surface and the nucleus. A third contribution is due to ice sublimation at the surface Q. Finally, the gas leaving the nucleus contributes as an other energy source due to the specific heat of the gas $c_{g,\mu}$ but this contribution is rather small. Taking all this quantities together leads to the following balance equation in W m^{-2} for the nucleus surface

$$\begin{aligned} \frac{F_{S,0}}{r_H^2(t)} (1 - \mathcal{A}) \max_{\zeta \in [0,2\pi)} \{0, \cos(\zeta)\} &= \epsilon_{em}\, \sigma T^4 + \kappa \nabla T(x,t) \\ &+ Q(T) + \sum_{\mu} c_{g,\mu}\, \rho_\mu\, u_\mu T \,. \end{aligned} \tag{2.21}$$

$F_{S,0}$ is the solar constant. The solar zenith angle controls how the incoming solar energy is distributed over the nucleus surface. The important formulas for the description in a cometocentric coordinate system have been derived by Sekanina (1979)

$$\cos(\zeta) = \cos(\theta)\cos(\phi)\cos(\theta_s) + \sin(\theta)\sin(\theta_s)\,. \tag{2.22}$$

θ is the latitude, ϕ the hour angle, and θ_s the cometocentric latitude of the subsolar point. The cometocentric latitude of the subsolar point is given by

$$\sin(\theta_s) = \sin(\delta)\sin(\Phi + \alpha)\,. \tag{2.23}$$

δ is the obliquity and Φ the argument of the subsolar meridian at perihelion.

The nucleus surface is covered by water ice of volume fraction ϕ_μ and dust. The surface sublimation term is given by the Hertz-Knudsen formula

$$Q_\mu(T) = \phi_\mu\, \Delta H_\mu\, P_{v,\mu}(T) \sqrt{\frac{m_\mu}{2\pi\, k_B T}}\,. \tag{2.24}$$

The lower boundary is given by the constraint that the thermal flux vanishes

$$\kappa \nabla T(x_b, t) = 0\,. \tag{2.25}$$

This adiabatic approach expresses the assumption that a quasi-stationary state is reached in a rotating body at depths beyond some skin depths of the thermal wave. Depending on the value of the thermal conductivity the position of the lower boundary has been chosen to secure a vanishing thermal flux well above the lower boundary.

A boundary condition for the gas diffusion problem is difficult to obtain, see e.g. the discussion in Skorov et al. (2001) and Davidsson and Skorov (2004). At this stage, the

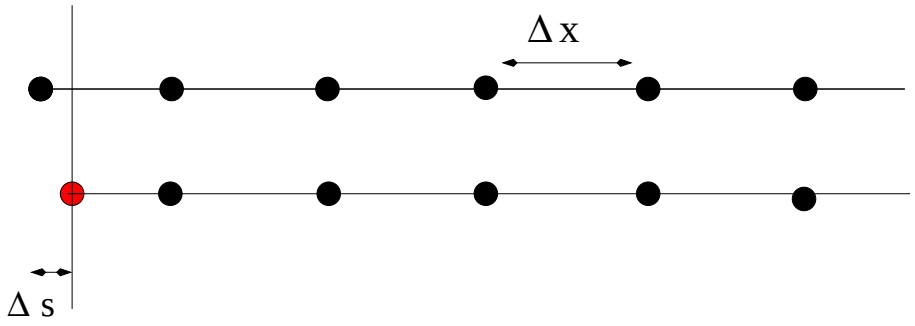

Figure 2.2: Due to surface sublimation a certain amount of material is ejected from the surface of the nucleus. This leads to a moving boundary and to a deviation between the actual grid and the current position of the surface. Special techniques are necessary for a proper treatment.

approach of most groups is followed. The vapor density is set equal to zero at the surface for CO, see e.g. Mekler et al. (1990)

$$\rho_{co}(x = 0) = 0\,. \tag{2.26}$$

For water vapor the approach of Spohn and Benkhoff (1990) is followed. The vapor density is set equal to the equilibrium conditions at the given surface temperature T_s

$$\rho_v(x = 0) = \rho_{v,eq}(T_s)\,. \tag{2.27}$$

2.8 Stefan problem of comets

The set of equations presented in the previous section, i.e. Eq. (2.10), Eq. (2.14), and Eq. (2.15) and its boundary conditions, has to be extended in order to incorporate surface erosion into the model. Due to sublimation of water ice a certain amount of surface material is ejected into space. Hence, the upper boundary is moving as sketched in Fig. 2.2. This movement poses a challenge to numerical modeling especially to the calculation of the thermal gradient in Eq. (2.21). In general, the amount of surface erosion Δs deviates from the spatial discretization size Δx. As a result the distance between the actual location of the surface boundary and the next grid node is less than Δx. In finite-difference schemes there are several approaches to deal with this situation as discussed in detail in Crank (1984). Our approach is motivated by the work of Crank and Gupta (1972). The thickness of the eroded material ds_μ of species μ is obtained from the so called Stefan condition (Stefan 1891)

$$\frac{ds_\mu}{dt} = \frac{Q_\mu(T)}{\Delta H_\mu \rho_\mu}\,. \tag{2.28}$$

The spatial grid Γ is moved according to this erosion size Δs at each time step, see Fig. 2.3. The temperature field is obtained at the new grid Γ^* through interpolation by cubic splines. The cubic splines $S_j(x)$, with j counting the number of intervals in the old grid Γ,

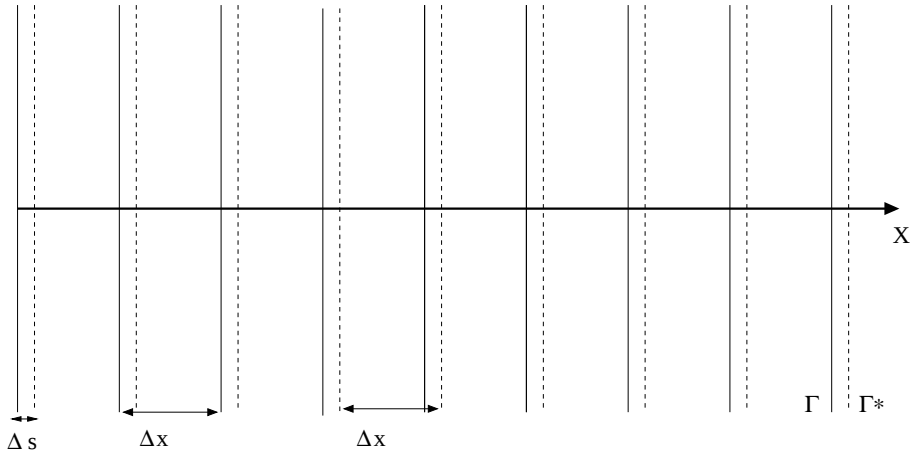

Figure 2.3: The spatial discretization size Δx remains constant throughout the computation. The old grid Γ is moved according to the erosion of surface material Δs. The temperature field at the new grid Γ^* is obtained through interpolation with cubic splines according to Crank and Gupta (1972).

are given by

$$\begin{aligned} S_j(x) &= s_{j,0} + s_{j,1}(x - x_j) + s_{j,2}(x - x_j)^2 \\ &+ s_{j,3}(x - x_j)^3 . \end{aligned} \tag{2.29}$$

The coefficients $s_{j,*}$ are obtained from a set of continuity conditions up to second order taken at the cell boundaries. x_j denotes the coordinate of the left sided edge of the interval j. Once the cubic spline functions are known the temperature at the new grid Γ^* is obtained through

$$T(x_j^*, t) := S_j(x_j + \Delta s, t) . \tag{2.30}$$

The adaptation of the spatial grid will be called temperature remapping. At each time step the erosion of surface material is taken into account. It is introduced to ascertain a constant spatial discretization despite surface erosion. It is designed to secure that the upper boundary is located on a grid node at each time step. Besides loss of energy through surface sublimation and thermal emission the nucleus is losing internal energy of the eroded surface material.

The mass density and the mass flux densities are only linearly interpolated to the new grid. Numerical calculations have shown that for the gas density a higher accuracy is not so important as for the temperature which controls the amount of energy entering the nucleus. This approach also constraints the amount of computing time considerably.

In the course of this thesis a calculation with the Stefan problem means that the temperature remapping technique described in this section is applied. In Fig. 2.4 is displayed a work flow diagram. The calculation starts with the solution of the heat and mass transfer equations. Then the thickness of surface erosion is determined by solving Eq. (2.28). Then the temperature remapping technique defined in Eq. (2.30) for the temperature field is applied on the temperature and similarly on the gas density field. Then the next time

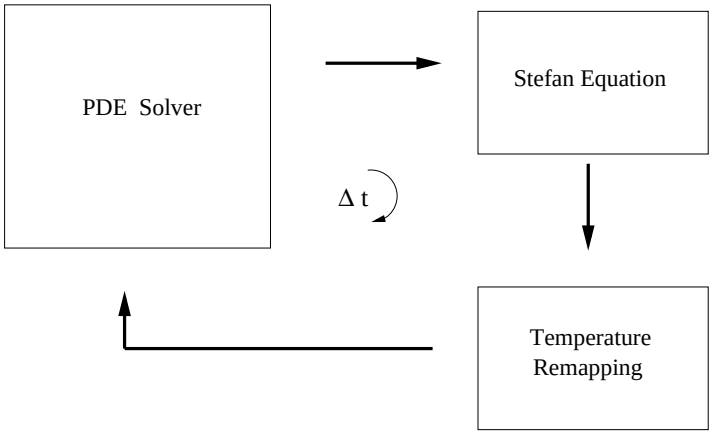

Figure 2.4: A work flow diagram showing how the temperature remapping technique is included in the solution of the thermal model. After solving the heat and mass transfer equations the thickness of surface erosion is determined by solving the Stefan equation. Then the temperature remapping technique is applied to adjust the temperature and gas density fields. Then the time step is increased and the next iteration begins. Without the Stefan problem the temperature remapping technique is not applied.

step is calculated. Neglecting the Stefan problem means that the temperature remapping technique for the temperature and the gas field is not applied.

2.9 Grid adaptation

In comets sublimation does not only occur at the surface but also in the interior. In this thesis an additional volatile species subliming from the interior is considered, e.g. CO. While the situation at the surface remains as in the previous subsection, the fact that there is a volatile species in the interior leads to a moving material interface. Therefore, the depth of the CO front denoted by Λ_{co} is time dependent. The number of grid nodes $N_\Lambda(t)$ distributed over Λ_{co} is obtained from

$$N_\Lambda(t) = \frac{\Lambda_{co}(t)}{\Delta x}\,. \tag{2.31}$$

Δx is the spatial discretization size, which is kept constant throughout the computation. Initially, the material interface is located on a grid node which means that $N_\Lambda(t)$ is an element of $\mathbf{N}$, the set of all positive integers,

$$N_\Lambda(t) \in \mathbf{N}\,. \tag{2.32}$$

In general, CO sublimation leads to a violation of condition Eq. (2.32). This movement of the CO front is resolved by first solving Eq. (2.28) for CO. Second, the thickness of surface erosion $\Delta s_i(t)$ and the movement of the CO front $\Delta s_{co}(t)$ is collected for several time steps, e.g. $t_1, ..., t_N$,

$$\Lambda_{co}(t_N) = \sum_{j=1}^{N} \Big(\Lambda_{co}(t_{j-1}) + \Delta s_{co}(t_j) - \Delta s_i(t_j) \Big). \tag{2.33}$$

Once the CO front $\Lambda_{co}(t)$ exceeds a grid node from the surface away, the number of grid nodes distributed along $\Lambda_{co}(t)$ is increased by 1. In the opposite case, the CO front $\Lambda_{co}(t)$ exceeds a grid node towards the surface leading to a reduction of the grid nodes distributed over Λ_{co} by 1. Depending whether surface erosion or CO sublimation dominates, the number of grid points between the surface and the CO front will decrease or increase with time. This approach has the benefit to be robust but it does not resolve the actual location of the inner front below the spatial discretization size Δx. It assumes that the CO front remains all the time on a grid node as long as the number of grid nodes does not change according to the described method. This approach is checked against variations of the spatial discretization size and it fulfills the appropriate stability conditions.

2.10 Summary of model assumptions

A short list of the employed model assumptions is given here based on arguments given above and on additional numerical studies:

- Only active areas without permanent dust mantles are considered that mainly contribute to activity. All dust grains are driven by the gas flow into the coma.
- The heat conductivity of cometary matter is low and, therefore a careful treatment of the thermal evolution of the comet as a Stefan problem is important.
- Heat conduction, heat advection, gas diffusion, sublimation, and condensation processes are considered.
- The existence of amorphous ice in comets or in the Solar System is not proven yet as discussed in Huebner (2008). Therefore, in distinction to many other approaches amorphous ice is not included in the present model.
- The nucleus is assumed to be spherical and smooth ignoring effects like self-heating, surface roughness and others. These assumptions should be acceptable given the lack of observational data.

2.11 Numerical solution of the model

The thermal model consists of the equations for the mass density Eq. (2.14), for the bulk gas velocity Eq. (2.14), for the heat conduction Eq. (2.15), and the boundary conditions in Eq. (2.21), Eq. (2.26), and Eq. (2.27).

This set of equations must be solved numerically. The thermal conduction equation is nonlinear if bulk sublimation of water and/or CO ice is included in the calculation. A Crank-Nicholson scheme is employed to discretize the thermal conduction equation. With a constant thermal conduction coefficient the temperature at time step $(n+1)$ is calculated from the time step (n) according to

$$\begin{aligned}\frac{T_i^{n+1}-T_i^n}{\Delta t} &= \frac{D}{2}\frac{T_{i+1}^{n+1}-2\,T_i^{n+1}+T_{i-1}^{n+1}}{\Delta x^2}+\frac{D}{2}\frac{T_{i+1}^{n}-2\,T_i^{n}+T_{i-1}^{n}}{\Delta x^2}\\ &-\sum_\mu \frac{\phi_{i,\mu}^{n+1}\,c_{g,\mu}}{2\,\rho\,c}\frac{T_{i+1}^{n+1}-T_{i-1}^{n+1}}{2\Delta x}-\sum_\mu \frac{\phi_{i,\mu}^{n+1}\,c_{g,\mu}}{2\,\rho\,c}\frac{T_{i+1}^{n}-T_{i-1}^{n}}{2\Delta x}\\ &-\sum_\mu \frac{E_\mu}{2}\left(q_{i,\mu}^{n+1}-q_{i,\mu}^{n}\right). \end{aligned} \tag{2.34}$$

ϕ denotes the mass flux, e.g. $\phi = \rho\,u$. $q_{i,\mu}^n$ denotes the mass source term defined in Eq. (2.12) at grid node (i) at time step (n) for a temperature T_i^n, e.g. $q_{i,\mu}^n = q(T_{i,\mu}^n)$. The constants D and E are defined as

$$D = \frac{\kappa}{\rho\,c} \tag{2.35}$$

and

$$E_\mu = \frac{\Delta H_\mu}{\rho\,c}\,. \tag{2.36}$$

The mass source term defined in Eq. (2.12) is linearized to first order in the time step Δt

$$q_\mu^{n+1} = q_\mu^n + \frac{\partial q_\mu^n}{\partial t}\Delta t + O(\Delta t^2)\,, \tag{2.37}$$

which is written as

$$q_\mu^{n+1} = q_\mu^n + \frac{\partial q_\mu^n}{\partial T}\left(T^{n+1}-T^n\right) + O(\Delta t^2)\,, \tag{2.38}$$

The equation for the bulk velocity Eq. (2.14) is employed to calculate the mass flux ϕ at the boundaries of the grid cell denoted by $\pm 1/2$. Its discretized form yields

$$\phi_{i\pm1/2} = -(\pm1)\,C\,\frac{\rho_{i\pm1}\sqrt{T_{i\pm1}}-\rho_i\sqrt{T_i}}{\Delta x}\,. \tag{2.39}$$

The mass flux is then used to calculate the stationary solution of the mass density balance equation defined in Eq. (2.14) which can be formulated as an explicit equation for the gas mass density

$$\rho_i = \rho_{i,eq} - \frac{1}{f_p\,c_{th}(T_i)}\frac{\phi_{i+1/2}-\phi_{i-1/2}}{\Delta x}\,. \tag{2.40}$$

The obtain set of algebraic equations are solved with a triagonal solver.

The upper boundary equation defined in Eq. (2.21) is nonlinear making special techniques necessary to find the surface temperature. This task is approached by first formulating the upper boundary condition as a root finding problem

$$F(T_0) = 0\,. \tag{2.41}$$

The technique to calculate the root is taken from Ridders (1979). Ridder's method is a root-finding algorithm that is based on the false position method well known in numerical analysis and on the use of exponential functions e^K to successfully approximate a root of a function. Assuming that a root lies between x_1 and x_2 Ridder's method evaluates the function F first at the midpoint $x_3 = (x_1 + x_2)/2$. It then solves for the factor e^K that satisfies a quadratic equation

$$F(x_1) - 2F(x_3)e^K + F(x_2)e^{2K} = 0\,. \tag{2.42}$$

The false position or regular falsi method is then applied to the functions $F(x_1)$, $F(x_3)e^K$, and $F(x_2)e^{2K}$. This yields a new guess for the root x_N. The updating formula is according to Vetterling and Flannery (2002)

$$x_N = x_3 + (x_3 - x_1)\frac{\mathrm{sign}\Big[F(x_1) - F(x_2)\Big]F(x_3)}{\sqrt{F(x_3)^2 - F(x_1)F(x_2)}}\,. \tag{2.43}$$

As discussed in more detail in Ridders (1979) the method has a number of interesting properties. In this thesis the fact that Ridder's method yields a very robust algorithm as also acknowledge in Vetterling and Flannery (2002) was the motivation to use this method. It yields results which are generally competitive with more advanced but also more complicated methods. The nonlinearities in the upper boundary of the thermal conduction equation defined in Eq. (2.21) demand for such a robust algorithm.

Ridder's method has also been used to calculate the Kepler orbit as discussed in Section 2.3.

2.12 Implementation of the model in C++

An important constrain for the model implementation was to create a program satisfying two aspects. First, it should be extendable. Second, it should have a modular design to allow the investigation of certain aspects by switching off others. The latter is important in scientific simulations as this is the only way to understand what effect a certain feature entails on the system. The former is important as in connection with the Rosetta mission new insights into the composition and structure of comets are expected making additions to the model inevitable. The program is written in the programming language C++.

The most simple scenario consists of a pure water ice comet without bulk sublimation and without the movement of the surface boundary. This model has been coded in a class referred to as Water. Around this class subclasses where constructed to address well defined tasks. The class Kepler gathers all data that are relevant for the calculation of the orbit and for the illumination conditions at different latitudes which in general depend on the orbital position of the comet. Hence, the illumination conditions of the nucleus surface depends on data calculated by the class Kepler. The class Kepler inherits from class Ridder's the methods to solve Eq. (2.8). The class Solver provides the algorithms to solve the heat conduction problem without gas diffusion and bulk sublimation. The calling of the Solver application interface (API) from class Water is declared virtual to allow new implementations of this class when gas diffusion and bulk sublimation is considered. The

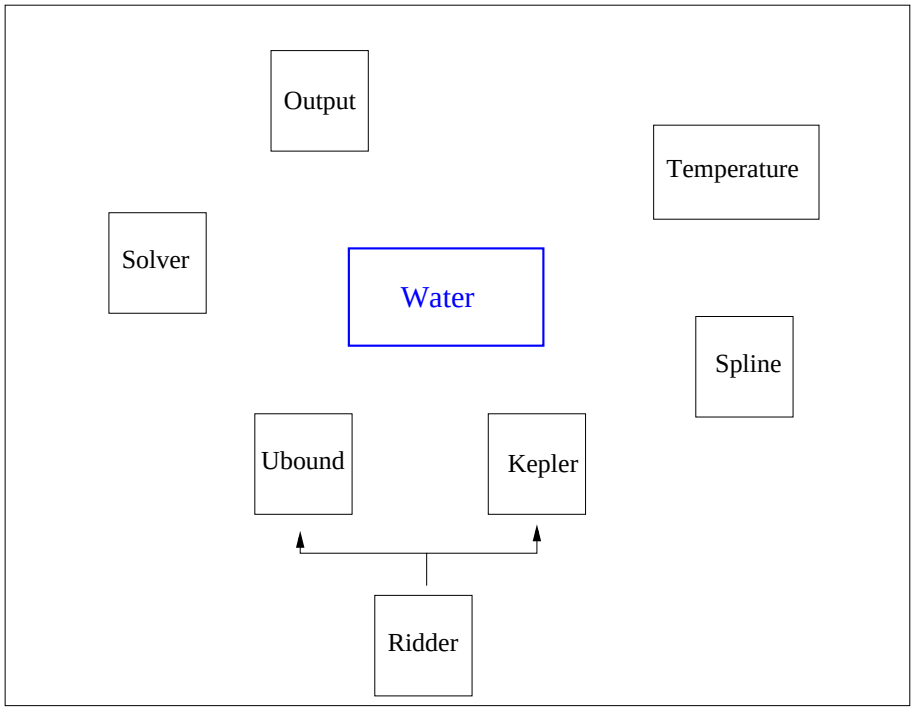

Figure 2.5: The structure of the fundamental class Water. Class Kepler calculates the Kepler orbit and related data. It publicly inherits the Class Ridder which provides Ridder's algorithm to solve Eq. (2.8). Class Solver solves the heat conduction equation without gas diffusion and bulk sublimation. Class Ubound calculates the surface temperature from Eq. (2.21) by publicly inheriting Ridder's method from class Rider. Class output consists of several classes which organizes the output of the simulation results. Class Temperature gathers all information on the temperature field. Class Spline provides the method to perform the temperature remapping technique described in Section 2.8 which can be easily switched on and off. Arrows denote inheritance.

class Ubound provides algorithms to calculate the surface temperature according to the surface boundary condition in Eq. (2.21). Ubound is derived from class Ridder as class Kepler. The temperature field and related data is gathered in class Temperature. Class Output provides different classes designed to print information and computation results. The basic class Water also includes a class Spline to perform the temperature remapping technique described in Section 2.8 which can be switched on and off through a *define* directive in a header file.

The class Water serves as a fundamental class of the computer model. Its structure is visualized in Fig. 2.5. A cometary nucleus model consisting of an ice-dust nucleus with water ice bulk sublimation and gas diffusion is derived from Water. A class Wgas publicly inherits the methods and members of class Water. In addition to the inherited methods two additional classes were constructed. First to solve the gas diffusion problem and then to solve the heat conduction problem with water ice bulk sublimation and gas diffusion. These classes were named class Gas and Solver, respectively. Therefore, the API to the solver method in class Water and the method to finish a calculation in class Water have

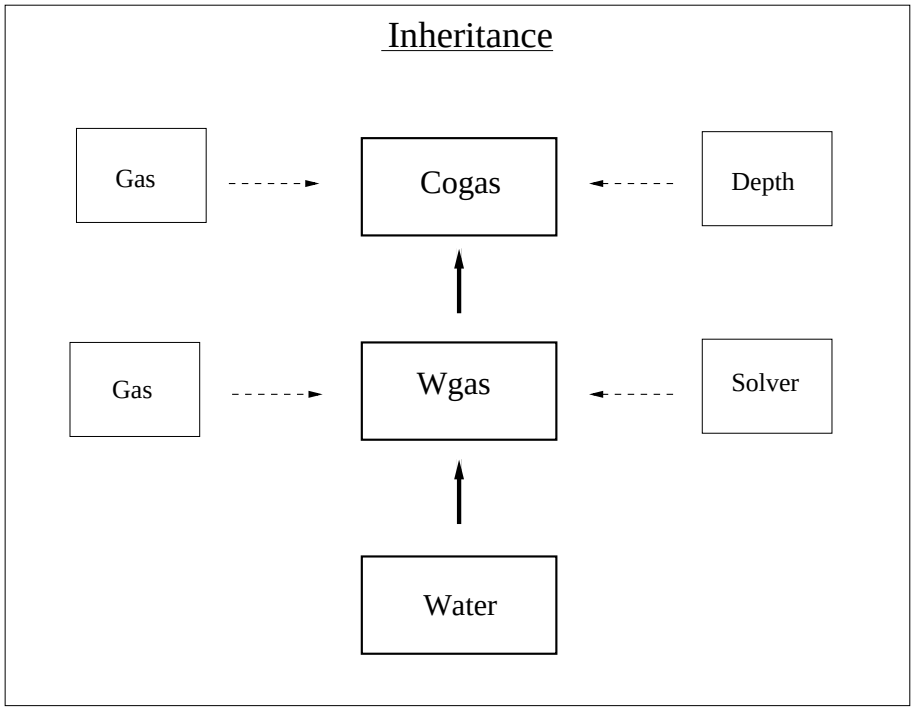

Figure 2.6: Inheritance tree of the thermal model implementation. The class Wgas inherits the methods and members of class Water publicly. A new class called Gas is introduced to solve the gas diffusion problem and a new class Solver is introduced to solve the heat conduction equation with gas diffusion and bulk sublimation. To solve the coupled heat- and mass transfer model with water and CO bulk sublimation and gas diffusion the class Cogas inherites from class Wgas. In addition to the members and methods inherited from class Wgas class Cogas consists of a member Gas for the CO gas and a new class Depth to calculate the movement of the CO front. Solid arrows denote inheritance. Dashed arrows denote inclusions compared to the base class.

been declared virtual. The mechanism to simulate the movement of the surface boundary remains as previously with an interpolation technique in class Gas for the mass density.

Extending the model further to include water and CO ice bulk sublimation and gas diffusion is achieved by publicly inheriting from class Wgas. The new class is called Cogas. In analogy to the treatment of water bulk sublimation and diffusion in Wgas the Cogas class includes a member Gas for CO as the methods to solve the gas diffusion model can be used for water and CO. To simulate the movement of the internal CO front a class Depth was designed. The inheritence tree of the programing model is displayed in Fig. 2.6.

The development of the program took place on a Linux maschine with the GNU C compiler collection and the GNU Gdb debugger. Git was used as a version control system right from the start. Few minor modifications are necessary to make the program runable on maschines with operating systems differing from the UNIX family.

3 Validation of the thermal model

In this chapter a number of tests of the thermal model are presented. The test suite comprises of numerical and physical tests to assure that the newly developed model is working properly. If not stated otherwise the following assumptions on the comet have been used in this section.

- The comet is on the orbit of CG with parameters given in Table 3.1.
- A single orbit apparition is calculated starting with a constant initial temperature distribution of 20 K.
- The comet consists of a pure water ice sphere.
- A single active point in the equatorial plane is considered.
- No obliquity effects are investigated.
- A low value of the thermal conductivity is employed, e.g. 10^{-3} W K^{-1} m^{-1}.

3.1 Numerical tests of the pure water ice sphere

A thorough numerical analysis of the employed numerical scheme is not possible because of the involved non-linearities. Classical approaches like the Von Neumann analyses may provide necessary conditions to judge the quality of the discretization scheme but in general no sufficient conditions as discussed in Hirsch (1991). A discretization scheme that gives in the linear case convergence results might produce instabilities depending on the nature of the involved non-linearities. Despite these draw backs there are recipes to judge the quality of the scheme. In this thesis the model is verified by calculating the temperature depth profiles as functions of discretization size in spatial and temporal dimensions. To be more precise, the temperature depth profile is calculated for two values of the discretization size in spatial dimension Δx_1 and Δx_2 with constant temporal discretization Δt denoted as T^1 and T^2, respectively. The method is accepted if the following condition holds

$$\max_{\Delta x \to 0} \left| T^1(x) - T^2(x) \right| \to 0 \,. \tag{3.1}$$

The same condition is applied with variable Δt and constant Δx. The values of Δt and Δx in Chapter 4 and in Chapter 5 are based on these tests.

In addition, it is important to compare simulation results for isolated scenarios for which the results can be inferred physically without strict calculation. For this purpose it

Table 3.1: Orbital parameters of CG. JPL denotes the NASA Small-Body Database.

Quantity	Symbol	Value	Source
Eccentricity	ϵ	0.640337	JPL
Semi-major axis	a_{semi}	3.4679 AU	JPL
Diurnal rotation period	τ	12.4 h	Lamy et al. (2007)
Orbital rotation period	τ_{orb}	6.46 y	JPL
Obliquity of rotation axis	δ	120 °	Lamy et al. (2007)
Argument of subsolar meridian	Ω	60°	Lamy et al. (2007)
Nucleus radius	R	2 km	Lamy et al. (2007)

is mandatory to have a code allowing to switch on and off certain features, e.g. with and without the Stefan problem, with and without gas diffusion and so on. The combination of these *numerical* and physical tests allow to have confidence in the results. For thermal modeling of comets it is also mandatory to apply the model on comet Hale-Bopp as for this comet an outstanding data set of production rates is available.

In Fig. 3.1 are displayed *numerical* tests for the spatial discretization size. The nucleus is a pure water ice sphere without the temperature remapping technique. The employed values of Δx lead to rapid convergence in the temperature depth profiles. The same is true for the Δt tests shown in Fig. 3.2.

Switching the Stefan problem on leads to slower convergence as is shown in Fig. 3.3 for the spatial discretization size. A spatial discretization of 0.5 mm is necessary. Similarly, a low temporal discretization of 50 s are necessary as shown in Fig. 3.4. These values also depend on the value of the thermal conductivity. For these tests a low value of 10^{-3} W m^{-1} K^{-1} has been employed. The spatial discretization is also constrained by the thermal skin depth which is for such a κ value around 3 mm.

3.2 Physical tests

A number of calculations for simple nuclei models are presented in this section. The case studies are simple but they are important to understand how the Stefan problem affects the thermal evolution of a comet. What effect has the Stefan problem on the thermal flux and subsequently on the energy distribution at the surface boundary? How do the Stefan problem and water vapor diffusion determine the thermal evolution of comets?

3.2.1 Thermal flux

On their journey through the Solar System comets undergo different illumination conditions which has a great impact on the thermal evolution of comets as solar irradiation is the primary energy source of comets. This is reflected by the r_H^{-2} dependence of the solar flux at the surface of the comet and by the dependence of the solar flux term on the solar

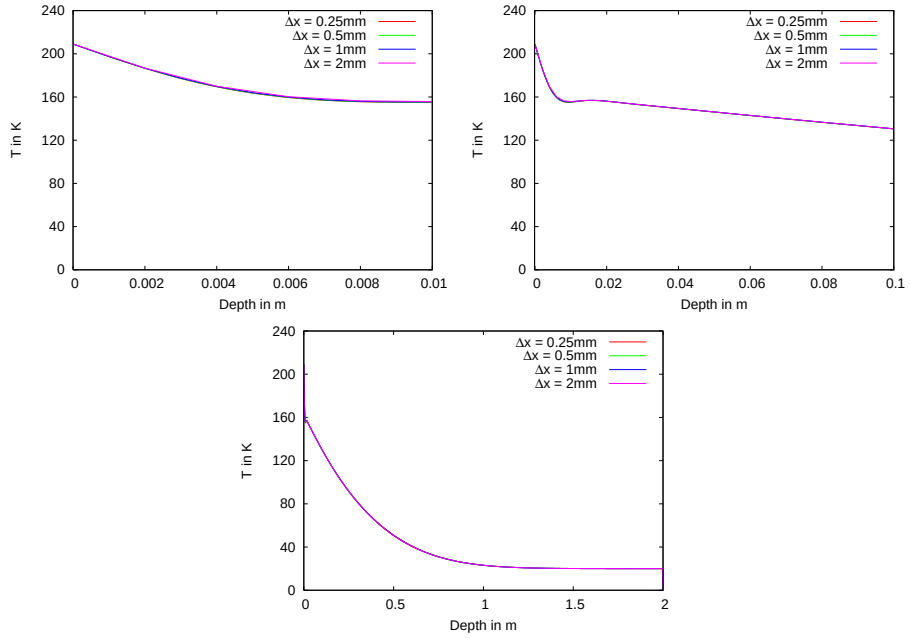

Figure 3.1: Convergence test for the spatial discretization Δx. The same calculation is shown for three distances from the surface, e.g. 1 cm, 10 cm, and 2 m. The comet is a pure water ice sphere without the temperature remapping technique. The physical length of the computational domain was set to 2 m. The thermal skin depth is for a $\kappa = 10^{-3}$ W m^{-1} K^{-1} about 3 mm and must be resolved in the simulation. The temperature depth profile converges very fast for the employed discretization.

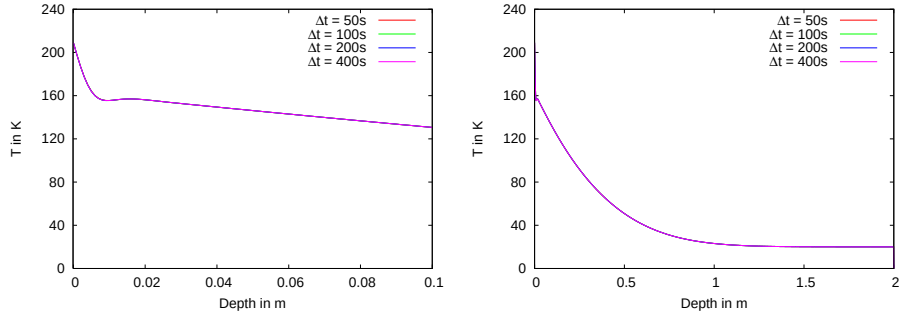

Figure 3.2: Convergence test for the temporal discretization Δt. The same calculation is shown for two distances from the surface, e.g. 10 cm and 2 m. The same scenario as in Fig. 3.1 is simulated here. A characteristic scale in temporal dimension is the diurnal rotation τ_r of the comet. In this case τ_r was about 12.4 h. Hence, low values of Δt lead to a rapid convergence.

zenith angle ζ, see Eq. (2.21). Depending on the solar input the thermal flux at the surface will provide thermal energy to the nucleus or to the surface from the nucleus. In Fig. 3.5 the thermal flux is displayed at perihelion. In the calculation with the Stefan problem the large temperature gradient at dawn is continuously reduced until surface sublimation of

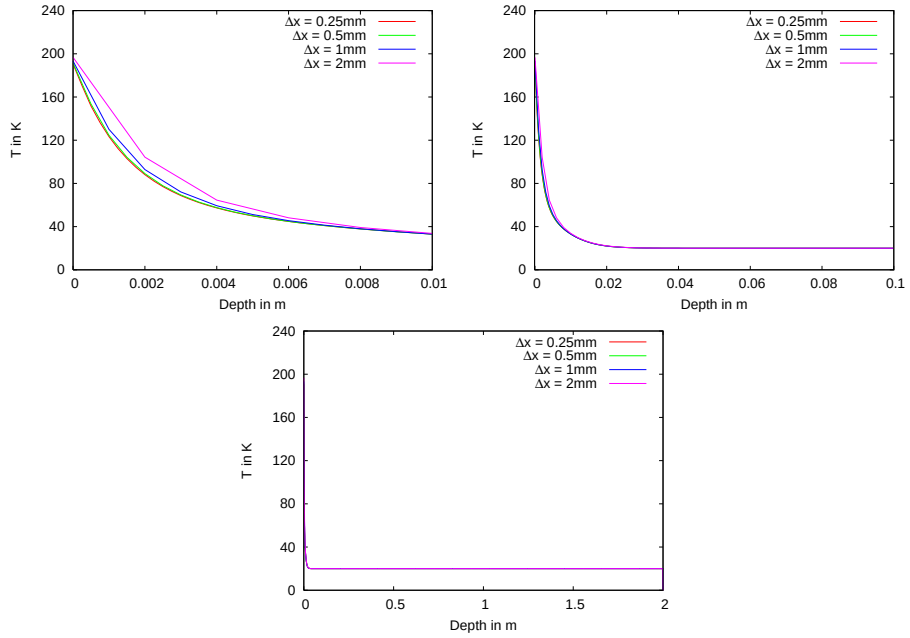

Figure 3.3: Convergence test for the spatial discretization Δx. The nucleus model is the same as in Fig. 3.1. In this case the temperature remapping technique is switched on. Refining Δx leads to converging temperature depth profiles. In this mode the rate of convergence is slower than in Fig. 3.1. With the temperature remapping technique a refined value between $\Delta x = 0.5$ to 0.25 mm must be employed.

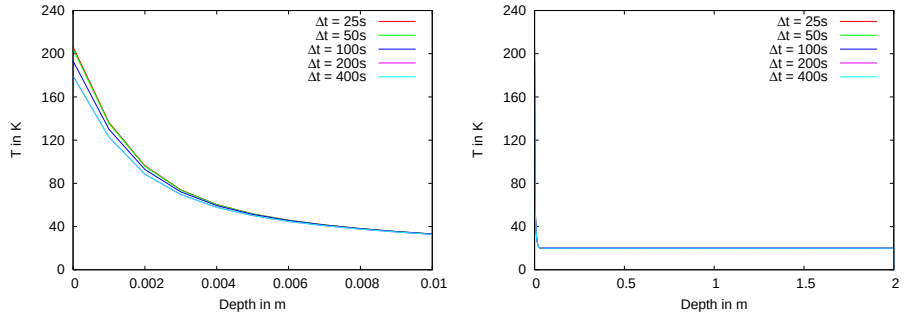

Figure 3.4: Convergence test for the temporal discretization Δt. The same scenario as in Fig. 3.3 is simulated here. The temperature remapping technique enforces a refined value of the temporal discretization Δt. Convergence is reached at a low value of $\Delta t = 50$ s.

water ice increases. As Fig. 3.5 shows when water sublimation reaches its peak value then the thermal flux increases again reaching at noon a local peak value. This enhancement of thermal flux from the surface into the nucleus is due to the erosion of previously heated surface layers. These relative warm layers are lost for the nucleus. Colder subsurface layers are excavated. Therefore, the thermal flux increases again. The peak value in the thermal flux is reached when surface sublimation and thus surface erosion is at its peak value. The temperature remapping technique accounts properly for the lost internal

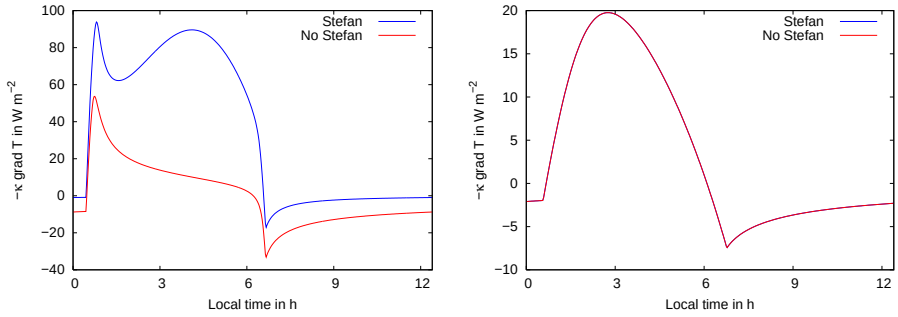

Figure 3.5: Thermal flux at the surface of a pure water ice sphere with and without the Stefan problem. A point in the equatorial plane for one diurnal rotation is shown. Left: Thermal flux at perihelion. Right: Thermal flux at aphelion. Stefan problem accounts properly for the lost internal energy of the eroded sub-surface layers through the temperature remapping technique, see Eq. (2.30). Therefore, the nucleus is much colder in the solution with the Stefan problem leading to a large thermal flux into the nucleus during local noon when surface sublimation reaches its peak value. At the aphelion position of CG, surface sublimation is negligible so that the thermal flux converge for both modi.

energy of the eroded sub-surface layers.

In the calculation without the Stefan problem the initially large temperature gradient is continuously reduced. The sub-surface layers receive thermal energy from the surface. The loss of internal energy in the warmed sub-surface layers is not taken into account. It is assumed that the energy content of these layers cannot much affect the energy budget of the nucleus. Thus, there is no need to simulate the energy loss process accurately. The thermal flux continuously declines from its peak value at dawn despite the maximum in water sublimation at noon. During the night, the nucleus without the Stefan problem conducts more energy to the surface as it is much warmer than the nucleus with the Stefan problem.

Far from the Sun the heating of the surface is weak. As shown in Fig. 3.7 water sublimation is negligible. Therefore, the thermal flux with and without the temperature remapping technique are the same. The peak value of the thermal flux is reached at around noon and not already at dawn as was the case at perihelion. The temperature differences between day and night are at 5.65 AU from the Sun smaller than at perihelion. Therefore, the peak thermal flux exhibits a smooth dependence on the local time.

3.2.2 Surface boundary at the water ice sphere

The distribution of the incoming solar energy to thermal re-radiation, water ice sublimation, and thermal conduction into the nucleus shall be investigated here in more detail to verify energy conservation. Two heliocentric distances are considered and a single diurnal rotation. The discussion starts without the temperature remapping technique.

The perihelion position is displayed in the left plot of Fig. 3.6. At a heliocentric position of 1.25 AU the incoming solar energy at noon is about 840 W m^{-2}. This energy is primarily used for water ice sublimation which comprises at noon around 85 % of the

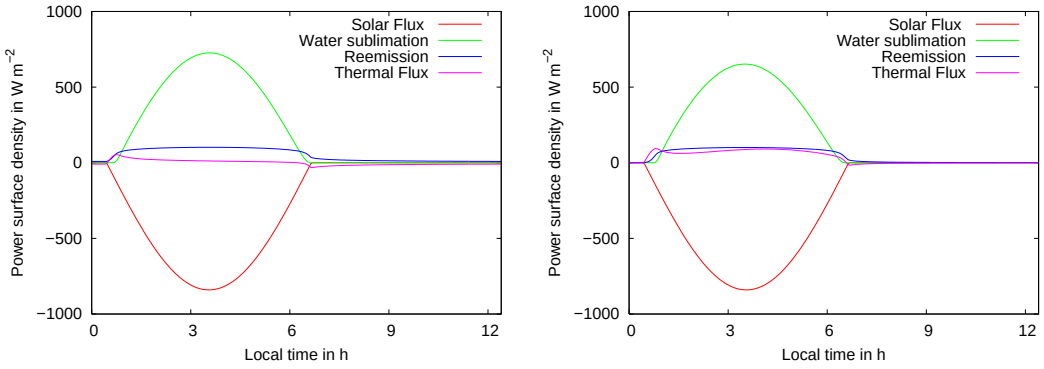

Figure 3.6: Surface boundary as described in Eq. (2.21) for the pure water ice sphere at perihelion. The solar flux, the water sublimation, the thermal reemission, and the thermal flux are displayed for an active point in the equatorial plane for a diurnal rotation. Energy input to the surface is negative. Left: Without the temperature remapping technique. At perihelion, 85 % of the incoming solar energy is transferred to water ice sublimation. Only a small fraction is conducted into the nucleus. During the night, thermal reemission dominates cooling down the nucleus. Right: With the temperature remapping technique. The Stefan problem leads to a much colder nucleus. Therefore, more energy is conducted into the nucleus leading to a strong thermal flux especially around noon when surface sublimation reaches its peak value. Less energy is available for water ice sublimation which makes a little bit more than 70 % of the solar energy. Thermal re-radiation remains almost constant. During the night this quantity is fed by thermal energy coming from the nucleus.

solar input. This is the reason why production rates of volatiles far from perihelion are important to constrain model assumptions and parameters. Near the Sun the absorbed energy is mainly used to maintain water activity while at larger heliocentric distances when water activity subsides the fractions of energy going for re-radiation and transfer into the nucleus interior become dominant. Fig. 3.7 showing the aphelion position corroborates this. Water sublimation is negligible and the small energy input from the Sun is divided among thermal re-radiation and thermal conduction. A time delay is visible as at dawn the nucleus is cold so that the thermal flux into the nucleus is large. As the nucleus warms re-radiation dominates from noon on to the night.

This picture is modified if the temperature remapping technique is switched on. At perihelion, surface erosion due to water ice sublimation leads to a colder nucleus. Therefore, the thermal flux into the nucleus is larger than in the calculation without the Stefan problem which is clearly visible when comparing the right hand side in Fig. 3.6 with the left hand side. Due to energy conservation less energy must be available to the other processes. According to Fig. 3.6 water ice sublimation shrinked from 85 % to around 70 %. Part of this energy is contained in the thermal flux. But the bulk of this energy is contained in the internal energy of the eroded surface layers.

It is also interesting to notice in which direction the Stefan problem strives the comet nucleus. The Stefan problem works against the mechanism which creates it. It tries to reduce the amount of surface sublimation and thus surface erosion.

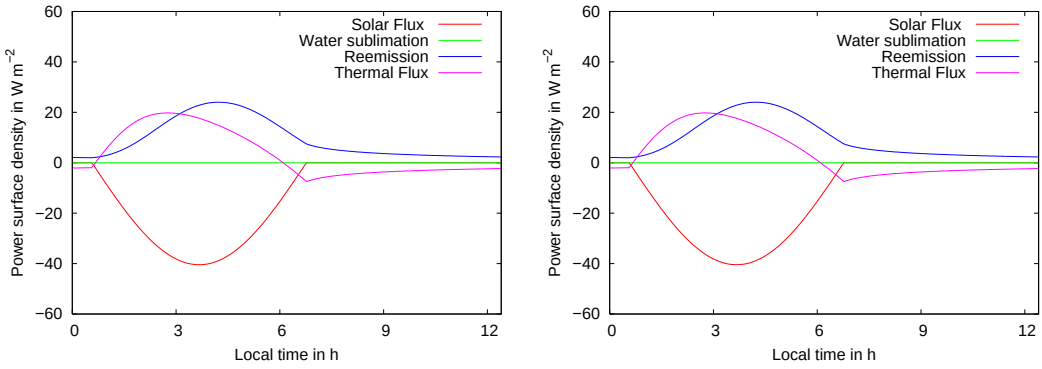

Figure 3.7: Surface boundary plot as in Fig. 3.6. Left: without the temperature remapping technique. Energy input from the Sun has shrinked considerably. At dawn, the nucleus is cold. Most solar energy is conducted into the nucleus. As the nucleus becomes warmer thermal re-radiation dominates the energy budget around noon. Water sublimation is negligible. During the night energy is provided to the surface from the nucleus. Left: with the temperature remapping technique. Water sublimation is negligible so that the Stefan problem does not affect the thermal state of the nucleus. The results are the same for both modi.

At the aphelion position of CG, water ice sublimation is negligible. Hence, the distribution of the incoming solar energy is the same for both calculations as is shown in Fig. 3.7. The sub-surface layers appear to converge to the same thermal state as the comet approaches its aphelion position.

3.2.3 The contribution of water vapor

In this section the pure water ice comet includes bulk sublimation of water and gas diffusion. The role of the effective pore radius is investigated in more detail in this chapter. The calculations are done without the temperature remapping technique described in Section 2.8. The program should reproduce the effect of energy transport from the sub-surface layers to the interior of the nucleus by gas vapor. As described in Spohn and Benkhoff (1990) energy transport by diffusing water vapor was an important result of the KOSI experiments. The measured temperature depth profiles had a convex shape which could be interpreted by vapor diffusing into the nucleus and releasing energy by condensation.

Figure 3.8 shows temperature depth profiles at perihelion and aphelion for three values of the effective pore radius r_p, e.g. 50 μm, 100 μm, and 200 μm. For comparison the temperature depth profile without bulk sublimation is also displayed. At perihelion, the convex temperature profiles as reported by Spohn and Benkhoff (1990) are clearly visible. Water vapor sublimes in the sub-surface layers and propagates into the nucleus reaching layers which are much colder than the layers in which the vapor was created. As the temperature and pressure conditions allow for vapor condensation latent heat of sublimation is released leading to local heating of the nucleus. Therefore, as Spohn and Benkhoff (1990) explained the temperature shows a convex profile in clear difference to the pure heat conducting comet. Convexity in the temperature profiles is strong for large

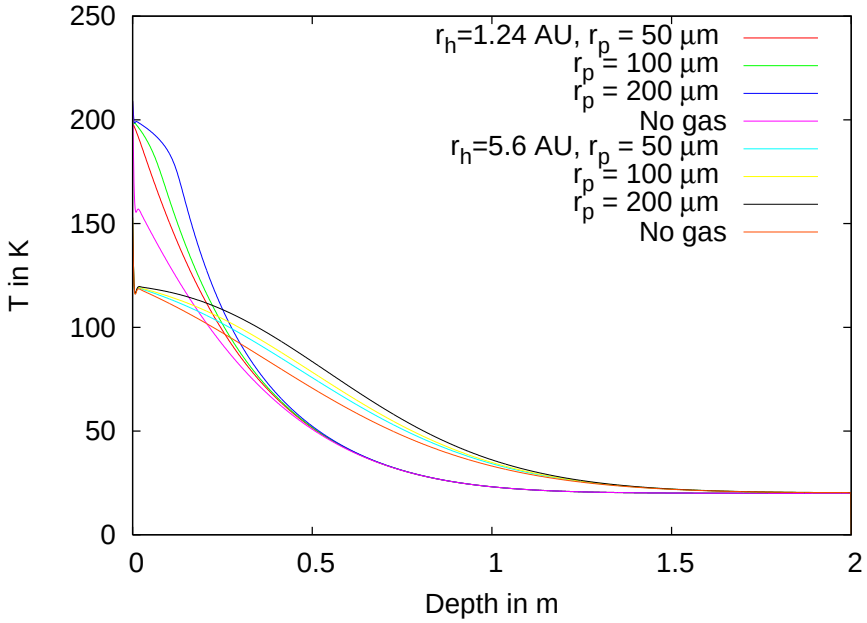

Figure 3.8: Temperature depth profile for a comet consisting of water ice with bulk sublimation and gas diffusion at perihelion and aphelion without the temperature remapping technique. The well known results of energy transport by vapor diffusing into the nucleus and releasing energy due to condensation are reproduced. Convex temperature depth profiles as reported by Spohn and Benkhoff (1990) are visible. The enhancement of this effect by a large pore radius is shown. A thermal conductivity of 10^{-3} W m^{-1} K^{-1} was used.

pore sizes, e.g. above 100 μm, as was the case in the KOSI samples. At a depth of 20 cm from the surface the temperature difference is more than 30 K depending on the choice of r_p. The effect is enhanced if the effective pore radius increases as in this case the gas can more easily be transported into the nucleus. The solution with an effective pore radius of 200 μm is at a depth of 20 cm almost 10 K above the solutions with 100 μm or 50 μm.

At aphelion, the illumination of the nucleus is low. Therefore, the amount of bulk sublimation is small leading to similar temperature depth profiles between the solutions with different pore radii and without gas diffusion at all. The differences below some 10 cm from the surface are mostly the result of a differing thermal evolution during perihelion passage. Close to the surface all gas solutions and results without gas show the same course at aphelion.

To conclude the model is able to reproduce the effect of vapor sublimation, vapor diffusion, and release of latent heat to the ice matrix as described by Spohn and Benkhoff (1990) in connection with the KOSI experiments. Vapor diffusion affects the temperature depth profiles. Its impact increases with the temperature and the effective pore size.

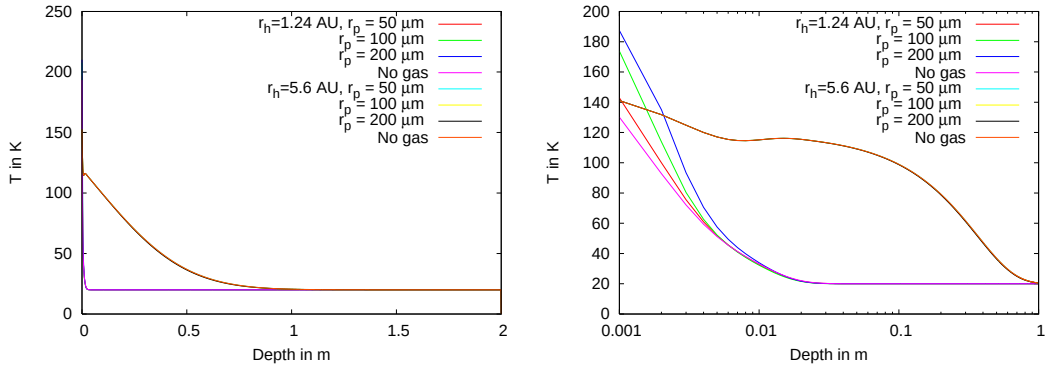

Figure 3.9: Temperature depth profile as in Fig. 3.8 this time with the temperature remapping technique. Surface sublimation leads to the erosion of warm sub-surface layers. The temperature in the new and cold sub-surface layers is too low to allow bulk sublimation. Therefore, no vapor transport into the nucleus is possible. The temperature profiles are not convex. At aphelion, surface sublimation is low but also the solar illumination of the surface. Therefore, no bulk sublimation is possble. On the right is the same plot shown only for a log scale on the abscissa. Only very close to the surface is the energy transport through the gas important.

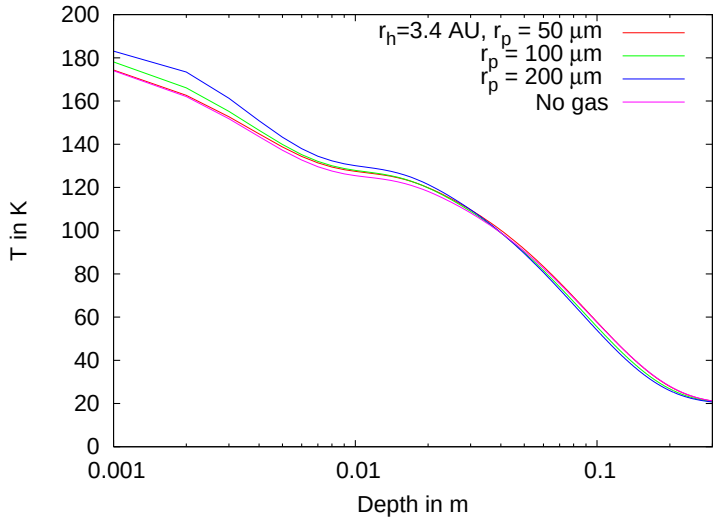

Figure 3.10: Temperature depth profile as in Fig. 3.9 at 3.4 AU from the Sun along the postperihelion branch. Note the logarithmic scale in the abscissa. At 3.4 AU surface sublimation has shrinked considerably allowing a gradual heating of the nucleus and thus bulk water sublimation and subsequent diffusion into the nucleus. Water vapor diffuses into the nucleus reaching cold regions and subsequently starts to condensate and to heat the matrix. A large pore radius enhances this effect.

3.2.4 Stefan problem and water vapor diffusion

Switching the Stefan problem for the scenario discussed in the previous section on leads to different results mainly at perihelion while at aphelion a similar conclusion can be drawn

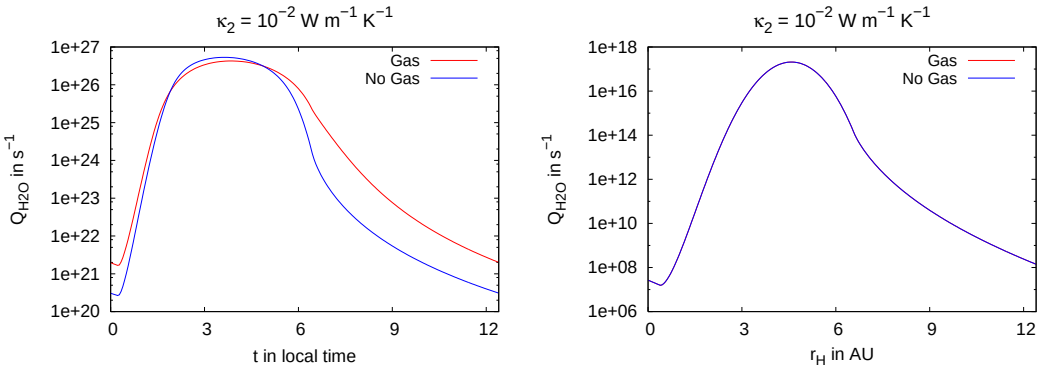

Figure 3.11: Water activity for an active point in the equatorial plane for a diurnal rotation. The Stefan problem is neglected here. Left: Water activity at perihelion. Gas diffusion leads to a lower peak value at noon while during the night the warm nucleus of the solution with gas diffusion produces a stronger water activity. Right: Water activity at aphelion. The results with and without gas diffusion are the same as no bulk sublimation is possible at such large heliocentric distances. A midsize thermal conductivity of 10^{-2} W m^{-1} K^{-1} is employed.

as before.

At perihelion, the contribution of water vapor is restricted very close to the surface to a distance less then 1 cm as displayed in Fig. 3.9. In depths beyond 1 cm from the surface the solutions for the three different pore radii are the same and they equal the solution without bulk sublimation. This result can be understood in terms of the erosion of surface material. The amount of energy conducted to the sub-surface layers remains low if erosion is increasing which is the case when the comet is close to the Sun and the active surface point is around local noon. As the sub-surface layers cannot heat up the amount of bulk sublimation of water remains low. The results are almost independent from the effective pore radius. With the Stefan problem the contribution of gas is almost negligible and confined to the immediate sub-surface layers which are subject to strong surface erosion.

During the postperihelion leg, surface sublimation is declining allowing a modest heating of the nucleus. At around 3.4 AU the sub-surface layers have reached temperatures allowing for bulk water sublimation. This leads to a gradual difference in the temperature depth profiles as was the case without the SP in Fig. 3.8. That is a high value for the effective pore radius leads to more gas diffusing into the nucleus and heating of cold regions in the interior of the nucleus. This is shown in Fig. 3.10

At aphelion, surface sublimation is low so that the movement of the upper boundary is negligible. The low energy input from the Sun, however, leads also to a negligible bulk sublimation and hence to no gas flow. The lower plot in Fig. 3.9 shows that all three solutions with gas are the same and they are equal to the solution without gas.

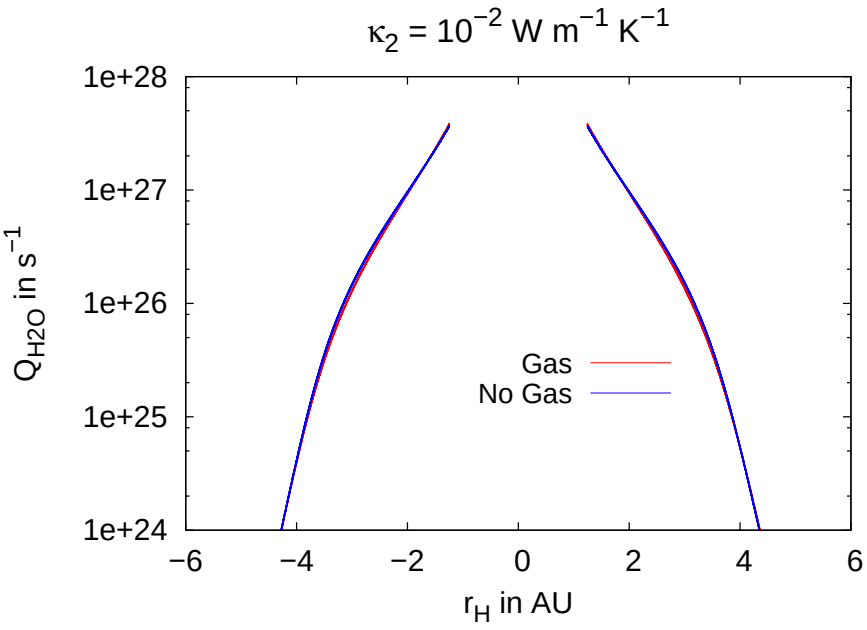

Figure 3.12: Water activity for an active point in the equatorial plane integrated over a diurnal rotation. Gas diffusion has a negligible effect on the water activity of CG.

3.2.5 Water activity with water vapor diffusion

In Fig. 3.11 water activity along a latitude in the equatorial plane is investigated with gas diffusion and without the Stefan problem. For comparison calculations without gas diffusion are also shown. A midsize thermal conductivity of 10^{-2} W m^{-1} K^{-1} is employed as for this case more energy is conducted into the nucleus allowing for stronger bulk sublimation compared to the 10^{-3} W m^{-1} K^{-1} case.

Figure 3.11 shows that water activity with gas diffusion is slightly below the solution without gas diffusion at around noon. During the night the nucleus with gas diffusion is warmer because of the heat transport by the inwards diffusing gas as also shown in Fig. 3.8 during the day. Therefore, more energy can be conducted to the surface during the night leading to higher sublimation rates. At aphelion, solar illumination of the nucleus is weak. Bulk sublimation is negligible so that water activity with and without gas diffusion is the same as shown in Fig. 3.11. Integrating the water activity for a diurnal rotation leads to very small differences in water activity over the whole orbit of CG as shown in Fig. 3.12.

3.2.6 Water activity with Stefan Problem and water vapor diffusion

In Fig. 3.13 the water activity along a latitude in the equatorial plane is investigated for two thermal conductivities. In both calculations the Stefan problem, water bulk sublimation, and diffusion are switched on. For comparison calculations without the Stefan problem are also shown. The depicted curves are time integrals for a diurnal rotation.

Figure 3.13 shows that for low thermal conductivities, e.g. 10^{-3} W m^{-1} K^{-1}, the water activity is along the whole orbit only slightly below the solution without the Stefan

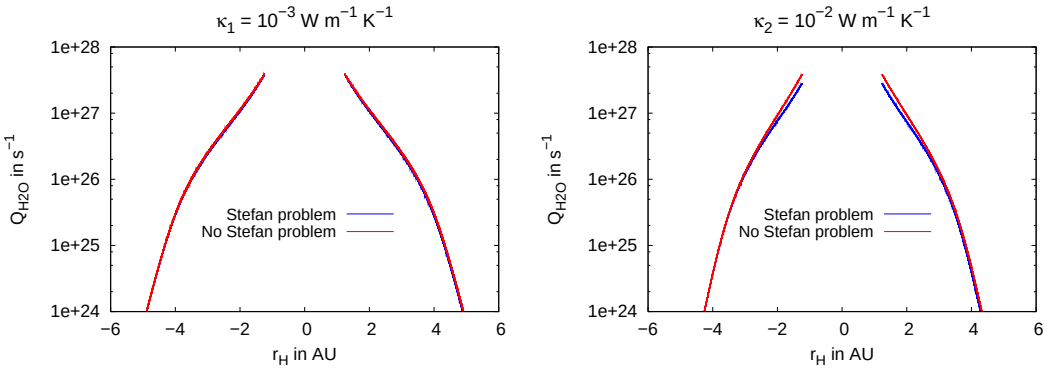

Figure 3.13: Water activity for an active point in the equatorial plane. The Stefan problem and water bulk sublimation and diffusion are switched on. Left: A low thermal conductivity of 10^{-3} W m^{-1} K^{-1} is employed. The Stefan problem solution is slightly below the solution without the temperature remapping technique. Right: A midsize thermal conductivity of 10^{-2} W m^{-1} K^{-1} is employed. In the solution with the Stefan problem water outgassing around perihelion takes only 70 % of the peak value of the solution without the Stefan problem.

problem. For higher thermal conductivities, e.g. 10^{-2} W m^{-1} K^{-1}, the water activity of the Stefan problem solution takes only 70 % of the peak value of the solution without the Stefan problem. As discussed in the previous Section a low value of κ leads to a negligible contribution of water bulk sublimation and gas diffusion around perihelion. Strong surface erosion leads to a colder nucleus prohibiting bulk sublimation of water ice at around perihelion when this process reached its peak value.

Increasing the thermal conductivity, however, leads to a different result. More energy is conducted into the nucleus enabling water bulk sublimation which cools the nucleus close to the surface further down. The thermal flux into the nucleus is getting larger. Therefore, less energy is available for surface sublimation. The solution with the Stefan problem adds to this effect. A high value of κ means that the internal energy of the eroded layers is higher than their counterparts with a small thermal conductivity. Hence, more energy is lost if these layers are eroded. Colder sub-surface layers are brought to the surface which increase further the thermal flux into the nucleus. Hence, less energy is available for water sublimation at the surface. The water production curve with the solution of the Stefan problem is below its counterpart without the Stefan problem. Water activity around the perihelion shrinked to 70 % of the peak value of the solution without the Stefan problem.

3.3 Summary

The code developed to simulate the thermal evolution of cometary nuclei is tested thoroughly in this chapter. A number of *numerical* tests were performed to prove that the model behaves as expected.

In the second part, certain isolated aspects of the model like the Stefan problem, gas

diffusion, and combination of these were studied to be prepared to interpret the complex models for comet Hale-Bopp and CG presented in the following chapters. The convergence of the thermal flux at aphelion in the solutions with and without the Stefan problem has been demonstrated. The enhanced thermal flux into the nucleus at perihelion has also been shown leading to less surface activity. The model is able to reproduce the convex temperature depth profiles reported by Spohn and Benkhoff (1990) in connection with the KOSI experiments. But, if the Stefan problem is taken into account than no convex temperature depth profiles are obtained for CG. The surface erosion of sub-surface layers prevents a strong heating of the sub-surface layers and thus bulk sublimation and heat transport via vapor diffusion. It has also been shown that gas diffusion does not much affect water activity.

4 Thermal model of C/1995 O1 (Hale-Bopp)

Hale-Bopp has been one of the most brightest comets passing Earth's orbit so far. With a peak water production of $10^{31}s^{-1}$ it was two orders of magnitude stronger than comet 1P/Halley. Hale-Bopp was extensively monitored with equipment on the ground and from space over a wide range of heliocentric distances. In cometary research Hale-Bopp is considered as a reference object. The observation campaign has lead to an unprecedented data base of production rates for various species. In this chapter the activity of Hale-Bopp for water and CO is studied.

4.1 Introduction

Hale-Bopp belongs to the family of long period (LP) comets with orbital periods above 200 years, e.g. 2534 years[1]. LP comets have randomly distributed orbital planes and aphelia. As Duncan (2008) writes LP comets appear to originate from a spherical shell of comet nuclei at heliocentric distances of 10^4 AU. This cloud was named the Oort cloud in honor of the discovering publication of Oort (1950). It is gravitationally bound to the Sun and it appears to lie just inside of the boundary between the Solar System and the galaxy. Perturbation by passing stars or galactic tides can scatter a comet on a path into the inner Solar System.

Comet Hale-Bopp was discovered at a heliocentric distance of 7.2 AU in July 1995. Its intrinsic brightness already at 7 AU offered the unique opportunity to study the evolution of cometary activity over a wide range of heliocentric distances pre- and postperihelion. The obtained data set of production rates contains important information about the physical and chemical state of the nucleus. Thermophysical nucleus models provide a mean to access this information by matching calculated production rates to those derived from observations. In particular, measurements of the nuclear activity over a wide range of heliocentric distances pre- and postperihelion strongly constrain the model assumptions and parameters. Near the Sun the absorbed energy is mainly used to maintain cometary activity while at larger heliocentric distances when the activity subsides the fractions of energy going for re-radiation and transfer into the nucleus interior become dominant.

[1] JPL Small-Body database: ssd.jpl.nasa.gov

Table 4.1: Orbital and rotational parameters of C/O1 1995 (Hale-Bopp). JPL denotes the NASA Small-Body Database.

Quantity	Symbol	Value	Source
Eccentricity	ϵ	0.9950817161	JPL
Semi-major axis	a_{semi}	185.864AU	JPL
Diurnal rotation period	τ	11.4 h	Jorda et al. (1997)
Orbital rotation period	t_{orb}	2534 y	JPL
Obliquity of rotation axis	δ	83 °	Jorda et al. (1997)
Argument of subsolar meridian	Ω	65...105°	
Nucleus radius	R	30 km	Fernández (2002)

4.2 Observations

Comet Hale-Bopp has been studied by a wide range of instruments. A good overview of the employed techniques and a discussion of the early understanding of the observations can be found in Bockelée-Morvan and Rickman (1997). From ground-based radio telescopes production rates for a variety of species were derived. A progressive release pattern for species like CO, CH_3OH, HCN, H_2O (from OH) and many others along the incoming branch has been detected (Jewitt et al. 1996, Biver et al. 1997). In addition, water production rates have been contributed by other groups (Colom et al. 1997, Stern et al. 1999, Weaver et al. 1999, Crovisier et al. 1999). Biver et al. (2002) updated their observations twice summarizing in their 2002 publication the full set of observations covering a heliocentric distance from -7 AU pre- to 15 AU postperihelion.

To understand the information coded in the production rates of comets it is important to recap the procedure applied to derive these values from observations. A general approach also applied by Biver et al. (2002) is to derive production rates from line intensities with a spherically symmetric Haser model and empirically determined temperatures and expansion velocities. The kinetic temperature and the expansion velocity of the coma are key parameters in this approach. In addition, radiative decay, infrared or ultraviolet pumping by solar irradiation are included in these models for all molecules. Thus the detected line intensities are coming from the coma. Therefore, the connection of the observed activity and sublimation processes in the nucleus is not straightforward. It is also possible that processes in the coma lead to the creation of daughter molecules which contribute to the observations. Such processes in the coma could be photochemistry, electron impact reactions, collisions in dense comae, and other types of chemical reactions. These kind of sources of volatile materials in cometary atmospheres are referred to as distributed sources. Irvine et al. (1998) and Rodgers and Charnley (1998) proposed that a chemical reaction in the coma involving HCN might be responsible for the detected HNC at comet Hale-Bopp. Cottin et al. (2001) suggest that the origin of H_2CO might lie in thermal degradation of polymers on grains in case of 1P/Halley. Eberhardt et al. (1987) reported from in-situ measurements of the local CO density in 1P/Halley during the Giotto encounter that possibly 2/3 of the local CO density originates from distributed sources. Disanti et al. (1999) and Disanti et al. (2001) reported that at a heliocentric distance of

1.5 AU the spatial distribution of CO molecules deduced from infrared long-slit observations of comet Hale-Bopp suggest that one-half of the CO was released by a distributed source. A possible parent molecule of the CO might be CHON grains. The other half is of nucleus origin. The authors also point out that beyond 2 AU from the Sun only the nucleus source of the CO was visible. Based on the work of Disanti et al. (1999) it can be concluded that around perihelion to 1.5 AU CO might also be from distributed sources. Lederer et al. (2009) reported that around 40 % of the observed of OH in the coma of Hale-Bopp might be from distributed sources. These observational findings are important contributions to the effort of understanding the activity mechanism of CO better. They suggest that the amount of CO and also of water coming directly from the nucleus might only be around 50 % for comet Hale-Bopp close to perihelion while further away from the Sun the primary source appears to be the nucleus.

In their recent paper Bockelée-Morvan et al. (2009) indicate that strong compositional inhomogeneities might be present at Hale-Bopp particularly for CO sources. The investigators report about a CO jet at a latitude position of 20° from which 40% of the observed outgassing may originate from. The authors assumed for their model that all CO is originating in the nucleus. Finally, Bockelée-Morvan et al. (2009) also report about the lack of a correlation between the CO jet and dust jets. Earlier, Lederer and Campins (2002) also wrote that comet Hale-Bopp appears to be chemically heterogeneous. These reports gave us a solid observational argument to study CO activity at different latitudes.

The Biver et al. (2002) observations of CO indicate three different regimes as the comet approaches the Sun. Beyond >3 AU the fit of the observations along the preperihelion branch appears to follow a $r_H^{-2.2}$ dependence on heliocentric distance r_H. From 3 AU to perihelion at 0.9 AU the fit follows a $r_H^{-1.9}$ law. Along the postperihelion branch the CO fit follows a r_H^{-2} dependence. The striking feature, however, is that the CO fit appears to follow the irradiation law of the nucleus' surface which follows a r_H^{-2} dependence on heliocentric distance. This observational result has stimulated the development of the thermal model presented in this thesis. Because such dependence of CO activity on the heliocentric distance appears to be only conceivable if the CO ice is stored close to the surface. But, previous thermal models of comets pushed the CO front several tens of meters below the surface as in de Sanctis et al. (2006) for comet CG. For comet Hale-Bopp Capria et al. (2000) obtained a flat CO curve if only CO bulk ice sublimation is assumed indicating that the CO ice is deep inside the nucleus even at perihelion. In this thesis, a mechanism is presented that is capable to bring the CO ice front close to the surface at perihelion which would allow to interpret the r_H^{-2} dependence of CO activity as reported by Biver et al. (2002). Besides CO also water is considered in the investigation. The other observed species could be to a higher degree from a distributed sources so that they are completely neglected in this investigation. Another interesting feature is that CO activity appears to be stalled or even decrease in the interval from 3 AU to 1.6 AU before exhibiting a steep increase.

An important input parameter for the thermal evolution of a comet is the thermal conductivity. Groussin et al. (2007) analyzed the near infrared spectra of the Deep Impact mission to comet 9P/Tempel 1. From these data a low thermal inertia of ≤ 50 W $K^{-1}m^{-2}s^{1/2}$, corresponding to a heat conductivity less than 0.003 W $K^{-1}m^{-1}$, was derived. In addition, Kührt (1999) showed for comet Hale-Bopp that a thermophysical nucleus model with a low thermal conduction coefficient of 0.001 W $K^{-1}m^{-1}$ is able to reproduce

the water sublimation measurements by assuming solely water ice sublimation without further assumptions, like extended sources (Enzian et al. 1998). More recently, Davidsson et al. (2009) re-evaluated the infrared spectra of the Deep Impact mission to comet 9P/Tempel 1. They included surface roughness into the model and derived thermal inertia values for most surface areas (inactive surface elements) in the range of 1000 to 3000 W $K^{-1}m^{-2}s^{1/2}$ or about 1 to 10 W $K^{-1}m^{-1}$. Due to the uncertainty of κ several cases were investigated from 0.001 W $K^{-1}m^{-1}$ to 0.1 W $K^{-1}m^{-1}$. The best fit to the observations was obtained with a 0.01 W $K^{-1}m^{-1}$ which is employed for the rest of the chapter.

The radius of the comet was set to 30 km as reported by Fernández (2002). According to Jorda et al. (1997) the diurnal rotation time of Hale-Bopp is about 11.4 h. Another important input parameter is the obliquity of the rotation axis. The distribution of the incoming solar energy on the surface of the comet heavily depends on this parameter as can be inferred from Eq. (2.22) and Eq. (2.23). Following Sekanina (1979), the illumination of a surface area can be calculated if the obliquity and the argument Φ of the subsolar meridian at perihelion are known. Jorda et al. (1997) published a value of 84 ° for the obliquity of Hale-Bopp. This value was used in Kührt (1999) together with an argument Φ of 64° which is slightly below the lower range provided by Vasundhara and Chakraborty (1999). Enzian et al. (1998) set Φ to 0° which was probably also employed in Enzian (1999). Vasundhara and Chakraborty (1999) calculated the obliquity and the argument of the subsolar meridian at perihelion. They published eight values for dates between Oct 6, 1996 to Oct 9, 1997 covering ranges from 77° to 90° for the obliquity and from 68° to 84° for the argument Φ. It seems that these angles are not so well constrained. Therefore, the obliquity is put to a value of 84° which was also published in Jorda et al. (1997) and considered several values for the argument Φ. It turned out that our simulations favor a value of around 105°.

4.3 Previous thermal models of comet Hale-Bopp

The observations of comet Hale-Bopp have stimulated many groups to apply their existing thermal models to match the calculated production curves with observations. Many of these thermal models rely on the assumption of amorphous ice and gas that is occluded therein and released upon phase transition (Mekler et al. 1990, Prialnik 1997a,b, Enzian et al. 1998, Enzian 1999, Capria et al. 2000, 2002). In addition, the model of Flammer et al. (1998) also includes clathrate hydrates with occluded gas. Upon phase transition, the occluded gas is continuously released during restructuring of the ice.

Prialnik (1997a) was among the first who studied comet Hale-Bopp with a thermal model assuming 5% of CO gas occluded in an amorphous ice matrix. The calculated CO curve is after perihelion almost constant in contradiction with CO observations. A similar result was reported by Flammer et al. (1998) who also obtained an almost flat CO curve. In this model is assumed that there are H_2O clathrate grains with occluded CO gas. However, the observations of Jewitt et al. (1996) and Biver et al. (1997) show a peak in CO production around perihelion. Later, Prialnik (1997b) presented a thermal model to study the long distance evolution of Hale-Bopp. A key model assumption is the existence of an amorphous ice matrix with occluded CO gas. But the model does not resolve the diurnal rotation of the comet. At that time, only few preperihelion observations were available.

Table 4.2: Set of model parameters employed for comet Hale-Bopp and CG.

Quantity	Symbol	Value
Mass concentration of water ice	X_i	0.4
Mass concentration of CO ice	X_{co}	0.1
Mass concentration of dust	X_d	0.5
Porosity	ψ	0.5
Pore radius	r_p	100 μm
Initial temperature distribution	$T_0(x)$	20 K
Initial depth of the CO front	Λ_0	50 cm

Enzian et al. (1998) presented a thermal model of Hale-Bopp and comparing the calculated water and CO production curves with preperihelion observations. Key model assumptions are the existence of amorphous ice with occluded CO gas. A modest fit through the available data points of CO has been achieved by assuming 10% of CO occluded in amorphous ice, 0° obliquity of the rotation axis, and an argument of the subsolar meridian of 0°. The water observations could not be fitted prior to 4 AU preperihelion. An estimate of the possible contribution of an extended water source due to water ice sublimation from icy grains in the coma is given. The proposed estimate allows to fit the data points beyond 4 AU. On the postperihelion branch, however, it is apparent that the water contribution of the extended source exceeds the observations. When the data set of Biver et al. (1997) became available, Enzian (1999) applied again his thermal model on Hale-Bopp. He considered two different values of the obliquity of the rotation axis 0° and 90°. The chemical composition of the comet was made up with 50% mass of dust, 40% amorphous water ice, 5% CO trapped in amorphous water ice, and 5% CO ice as an independent phase. The simulation is started at 50 AU preperihelion and finished at 50 AU postperihelion. With these assumptions the author was able to reproduce the preperihelion CO outgassing pattern with an obliquity of 90°. The fit of the CO data along the postperihelion branch is modest and ends at 4AU postperihelion. The data fit with 0° obliquity of the rotation axis was poor pre- and postperihelion. At the same time, the water production rates could not be fitted beyond 4 AU preperihelion.

Kührt (1999) showed that a thermophysical nucleus model is able to match the water sublimation measurements without the assumption of extended water sources in the coma. Based on the strong obliquity of Hale-Bopp as reported by Jorda et al. (1997), Kührt (1999) investigated the apparent strong influence of seasonal effects on the water sublimation curve. He showed that it is possible to fit the water production rates if a low thermal conductivity is used.

Capria et al. (2000) published a thermal model of comet Hale-Bopp and compared their results with CO observations in the range from -7AU pre- to 3AU postperihelion. The best fit to the data set which was available at that time was achieved by assuming that CO exists as an independent ice phase and that 20% of the CO is released only after water sublimation. Another 10% of the CO gas is trapped in amorphous ice. No water

sublimation curves are shown in this paper. In a later article, Capria et al. (2002) compared their results for the water and CO activity of Hale-Bopp with observations in the range from -7 AU pre- to 4 AU postperihelion. The calculated water flux fits the observations only in the range from -2 AU to -1 AU, preperihelion. The remaining data points in the range from -5 AU to -2 AU are not fitted by the model, neither are the data points along the postperihelion branch. The assumptions of the trapped CO ice are similar to those of Capria et al. (2000). In the range from -2 AU to -1 AU the fit of the CO data is good while in the range from -7 AU to -2 AU the curve is an upper limit to the observations. The same holds for the postperihelion branch. The range covered along the postperihelion branch is 1 AU to 4 AU. The curve does not match the data points so well.

It can be concluded that the model of Enzian (1999) and Capria et al. (2002) seem to fit the observations of Hale-Bopp for CO quite well although neither model has been applied to the full data set covering a range from -7 AU pre- to 15 AU postperihelion as reported by Biver et al. (2002). Both models employ similar assumptions on the existence of amorphous ice and the amount of occluded CO gas (5 to 20%). The water production curve could not be reproduced so well by either of model. Both suggest that extended sources might be responsible for the water sublimation beyond 4 AU preperihelion.

The existence of amorphous water ice and clathrate ice in comets is contentious. Huebner (2008) gave an overview of the current state of the debate which tends to question the existence of such water ice phases in comets. In particular, Huebner (2008) points out that neither amorphous ice nor clathrate ice were observed in interstellar clouds, in star-forming regions, or outer solar system objects. Amorphous ice was created in laboratory experiments at low temperature and fast rates of condensation. Recent papers on laboratory experiments of amorphous ice can be found in Bar-Nun and Laufer (2003), Laufer et al. (2005), and Bar-Nun et al. (2007). Blake et al. (1991) showed that amorphous ice transformes to clathrates hydrades in laboratory experiments. As Huebner (2008) emphasizes laboratory measurements are important for understanding cometary properties but they are indirect arguments and maybe sometimes not representative.

Huebner (2008) put another important argument against amorphous ices based on the sequence of condensation of materials with differing thermal enthalpies of sublimation. As temperature decreases material condenses based on the scheme that gases with higher enthalpies of sublimation condense first. That would suggest that water condenses at a much higher temperature. At these temperatures, however, it is more likely to form crystalline ice. On Earth clathrate hydrates are known to exist below the ocean bed and in cold under ground regions such as Siberia. But, as Huebner (2008) wrote the clathrates tend to disintegrate at low pressures.

Based on this collection of arguments against the existence of amorphous ice and clathrate hydrates in comets these assumptions are not employed in our model. Only bulk ice sublimation of volatile materials is considered.

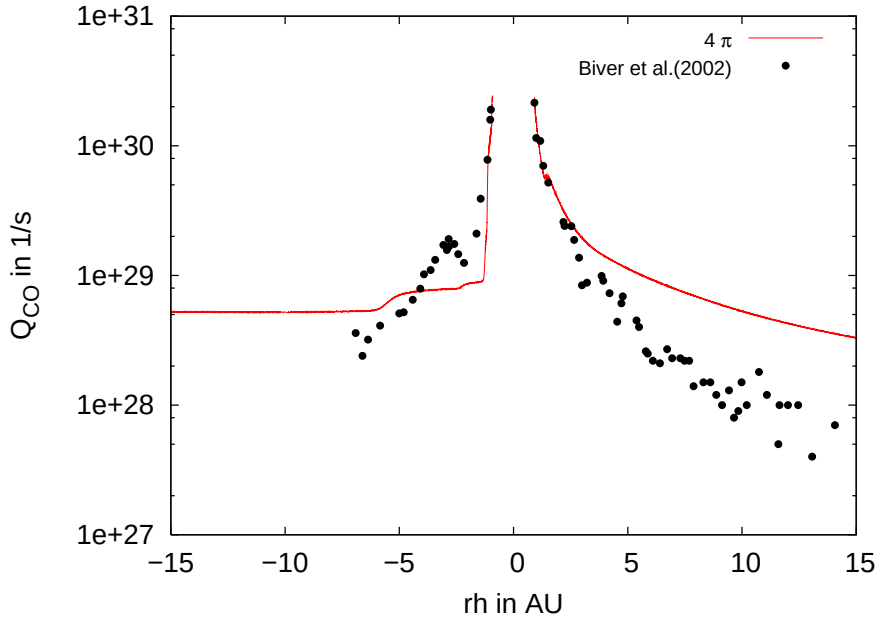

Figure 4.1: CO production curve plotted as function of heliocentric distance. The curve is calculated by integration over the whole spherical nucleus. The fraction of active surface elements was about 0.25. The CO curve fits the CO data of Biver et al. (2002) only close to perihelion well. Figure from Gortsas et al. (2010a).

4.4 Results

4.4.1 Calculation setup

The nucleus model of Hale-Bopp assumes a two-layer stratigraphy with the upper layer being a mixture of water ice and dust while the lower layer includes also CO ice. The parameters of the calculations can be found in Table 2.1, Table 4.1, and Table 4.2. Comet Hale-Bopp is a long period comet with a period of 2530 years. CO and water activity, however, is determined when the comet is close to the Sun. Therefore, for this study the comet is put at a heliocentric distance of 20 AU and the calculations are proceeded to 20 AU postperihelion. This approach was also followed by Enzian et al. (1998) and Enzian (1999). A constant initial temperature distribution of 20 K was assumed and the CO front was put to a depth of 50 cm from the surface.

4.4.2 Results for CO activity

The integrated CO activity F_{CO} of Hale-Bopp is compared with observations. Activity is calculated through integration over the whole spherical nucleus

$$F_{CO} = f_a \frac{2\pi}{\tau_r} R^2 \int_{-\pi/2}^{\pi/2} d\theta \cos(\theta) \int_0^{\tau_r} dt\, q_{CO}(\theta, t)\,. \tag{4.1}$$

R is its radius, under the assumption that the comet is spherically symmetric. The fraction f_a of active surface areas is employed to fit the observations with the calculated production

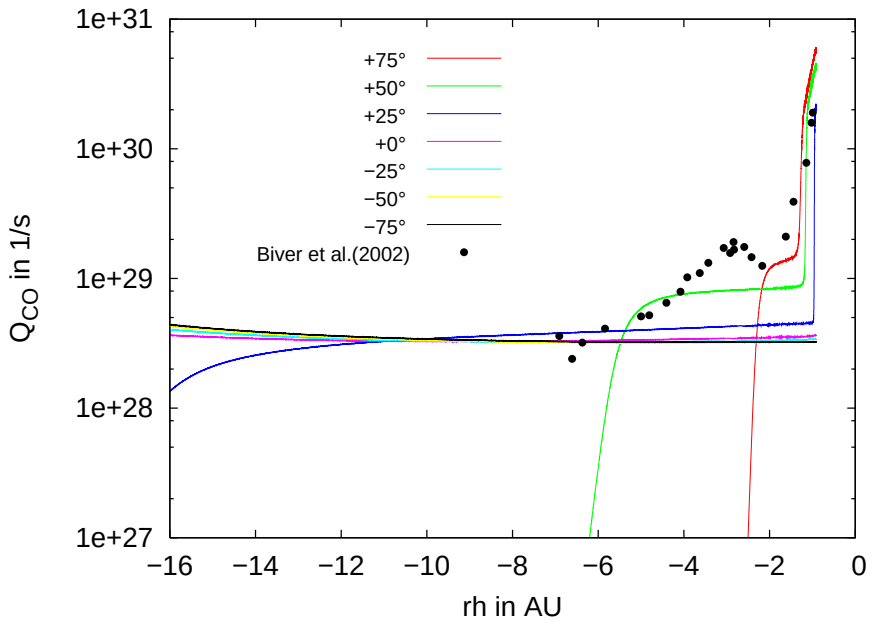

Figure 4.2: Similar CO plot as in Fig. 4.1. The CO production of seven latitudinal stripes with thickness of 25° are presented along the preperihelion branch. The CO data of Biver et al. (2002) could be fitted if CO activity is confined to the positive hemisphere above a latitude of 0°. Figure from Gortsas et al. (2010a).

curves.This approach is commonly used although it might not always be stated. q_{CO} denotes the CO flux from a latitude θ at time t at the surface.

For a thermal conductivity of 0.01 W m^{-1} K^{-1} the CO production curve is shown in Fig. 4.1. It is assumed that the active CO spots are distributed over the whole nucleus. The spherical nucleus is divided in latitudinal direction into stripes with a thickness of 25°. The obliquity of the comet was set to 84° and the argument of the subsolar meridian Φ had a value of 105°. Apparently, the model is not able to reproduce the CO production rates of Biver et al. (2002). Only close to perihelion, the model seems to fit the observations.

This result is in agreement with previous reports. So far only Enzian (1999) and Capria et al. (2002) were able to present good fits of the CO observations, however, only over a limited heliocentric distance from -7 to 4 AU and with the assumption that amorphous ice with trapped CO gas is present. This assumption is not followed in the present approach because the presence of amorphous ice in cometary nuclei is contentious, see also the discussion in Section 4.3. The most straight forward approach is to assume CO bulk ice sublimation and to perform an integration over the whole nucleus. But this approach has failed (Capria et al. 2000).

Recent observational findings concerning the chemical heterogeneity (Lederer and Campins 2002, Bockelée-Morvan et al. 2009) and a CO jet at a latitude of 20° (Bockelée-Morvan et al. 2009) indicate that cometary activity might be localized. Therefore, the CO activity of Hale-Bopp at different latitudes is investigated. In Fig. 4.2, CO activity along the preperihelion branch is depicted. This result indicates that confining CO activity on the positive hemisphere above 0° could fit the observations. The CO activity for different

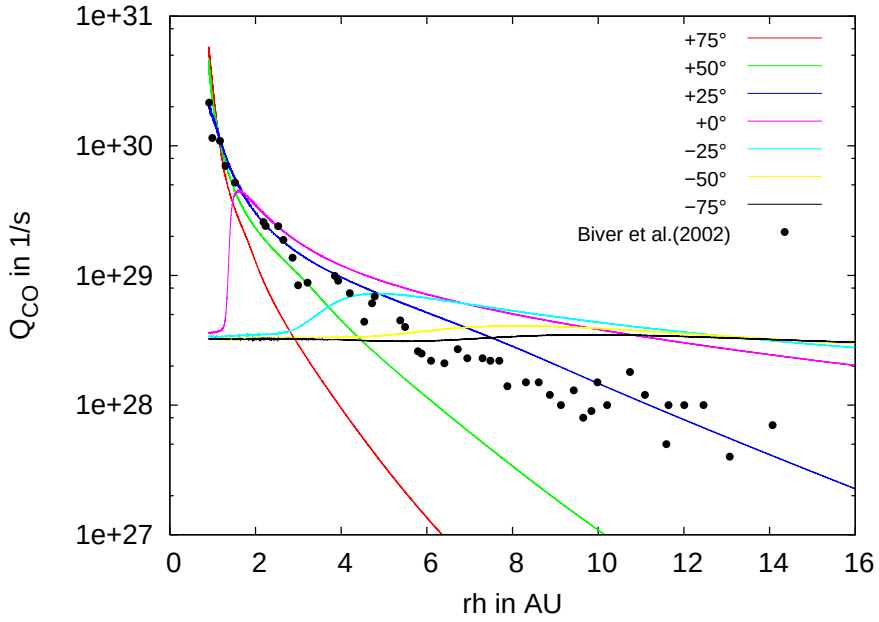

Figure 4.3: Similar CO plot as in Fig. 4.2 for the postperihelion branch. The CO data of Biver et al. (2002) along the postperihelion branch could be fitted if CO activity is confined to the positive hemisphere above a latitude of 0° as in the preperihelion case of Fig. 4.2. Figure from Gortsas et al. (2010a).

latitudinal heights along the postperihelion branch is depicted in Fig. 4.3. It is apparent that a good fit to the postperihelion CO data of Biver et al. (2002) is obtained if CO activity is confined to the positive hemisphere above 0° as in the preperihelion case. The result of such a scenario is displayed in Fig. 4.4. The good fit of the CO data depends on the assumption that CO activity is confined in the positive hemisphere and that the rotation axis of the comet is tilted. As shown in Table 4.1 the obliquity of comet Hale-Bopp is very strong leading to strong seasonal effects.

The model is able to fit the CO observations of Biver et al. (2002) over the whole measured heliocentric distance starting at -7 AU preperihelion to almost 15 AU postperihelion. The fraction of active surface elements f_a was set to 0.75. The presented CO curve seems to be in good agreement with the CO jet at a latitude of 20° as reported by Bockelée-Morvan et al. (2009) for the observations at 11 March 1997, which was close to perihelion on the preperihelion branch. At around -2 AU preperihelion the model approximates the local peak in the observations by a plateau.

4.4.3 Results for water activity

The water production curve for the best CO scenario of the previous section is depicted in Fig. 4.5. It is assumed that the positive hemisphere above 0° is active in water and CO while the remaining nucleus surface is still outgassing water vapor but not CO. The model is able to reproduce the general trend of the water observations throughout the orbit. The fraction of active surface elements f_a is about 0.25. This result is in agreement

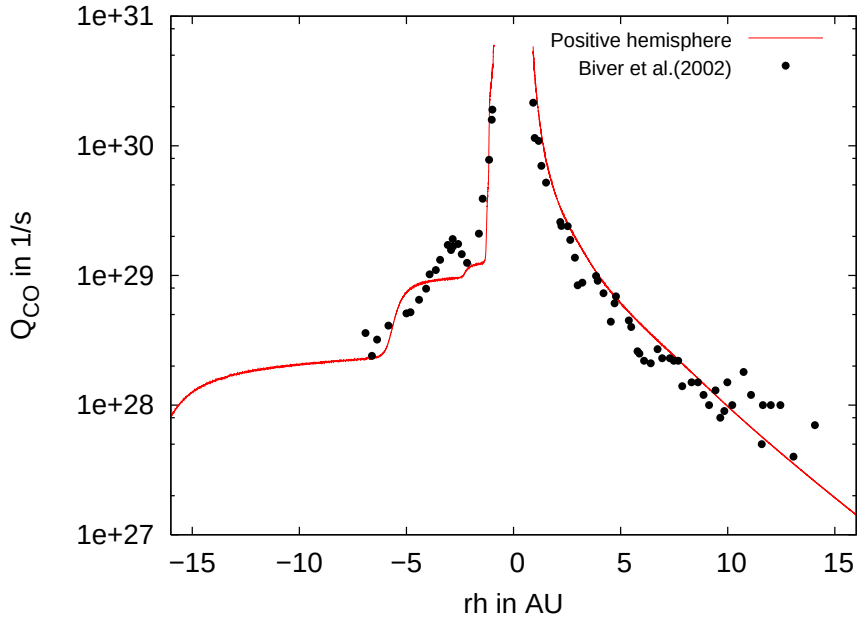

Figure 4.4: Similar CO plot as in Fig. 4.1. The CO production curve is integrated over the positive hemisphere above 10°. The fraction of active surface elements was 0.75. The CO data of Biver et al. (2002) are well reproduced along the preperihelion branch and remarkably well along the whole postperihelion branch covering a heliocentric distance from 1AU to almost 15AU. The local peak at around -2AU is approximated by a plateau. Figure from Gortsas et al. (2010a).

with Kührt (1999). Our fit of the water observations is slightly better than that presented in Enzian et al. (1998), Enzian (1999), and Capria et al. (2002). These groups argue that beyond 4AU preperihelion water activity could only be due to icy grains in the coma while around perihelion nucleus activity is mainly responsible for the observed water activity of Hale-Bopp. Enzian et al. (1998) gave an estimate of the water activity of icy grains in the coma. The water production curve of this estimate seems to fit the water observations beyond 4AU on the preperihelion branch. Along the postperihelion branch, the water production rates, however, could not be reproduced.

In a recent article, Lederer et al. (2009) analyzed Hale-Bopp data with a Monte Carlo model which indicates that extended sources due to icy grains in the coma might contribute to water activity. The simulations were performed on data from April 22-26, 1997. At that time the comet was at the beginning of its postperihelion branch.

Currently, it is difficult to judge to what extend cometary water activity could be due to extended sources and whether these sources contribute significantly to the observed water activity of this comet on its whole orbit or whether it is only a transient effect.

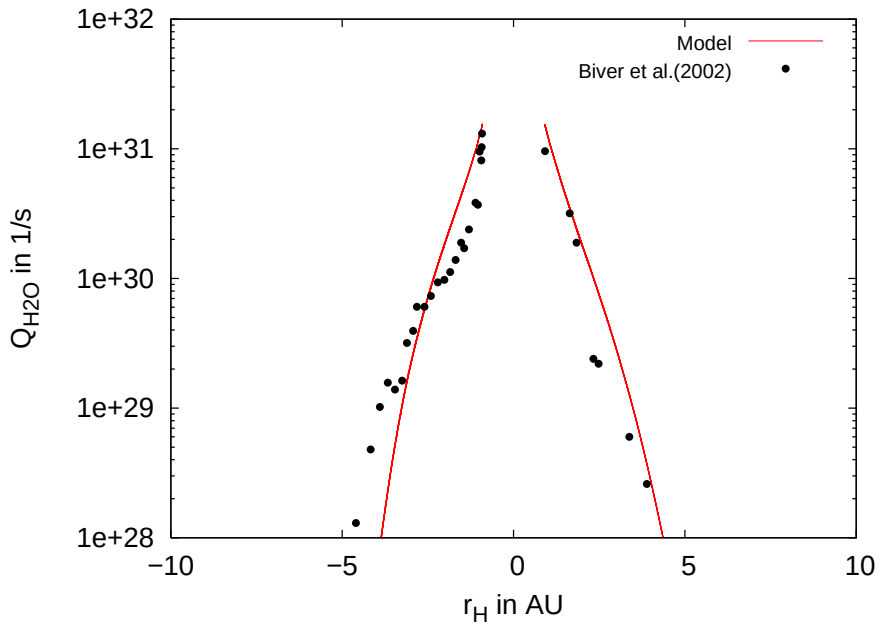

Figure 4.5: Water production curve of Hale-Bopp plotted as function of heliocentric distance. The production curve is obtained through integration over a spherical nucleus with a fraction of active surface elements of 0.25. CO activity takes place on the positive hemisphere above 0° according to the best fit scenario of Fig. 4.4 while water active surface areas are distributed over the whole nucleus. The general trend of the water production rates of Biver et al. (2002) are reproduced over the whole range. Figure from Gortsas et al. (2010a).

4.4.4 Results for different values of the argument Φ of the subsolar meridian at perihelion

The illumination of a surface area on the nucleus depends according to Sekanina (1979) on the angle between the equatorial plane of the comet and the orbit plane, e.g. obliquity of the comet, and the argument Φ of the subsolar meridian at perihelion. These values enter the calculation of the solar zenith angle ζ according to Eq. (2.22) and Eq. (2.23). Unfortunately, these values are not so well constrained but they clearly influence the outgassing pattern of the nucleus.

This should briefly be demonstrated for CO. The CO production curve for the best fit scenario of Section 4.4.2 is shown in Fig. 4.6 for an argument Φ of 105° and 95°. Thus, changing Φ by a value of 10° shifts the CO outgassing curve clearly. Hence, this parameter must be treated carefully when comparing simulations with observations.

4.5 Discussion and conclusions

A novel thermophysical approach is presented to interpret the observations of comet Hale-Bopp as reported by Biver et al. (2002). The nucleus model accounts for heat conduction, heat advection, gas diffusion, sublimation, and condensation in an ice-dust matrix with

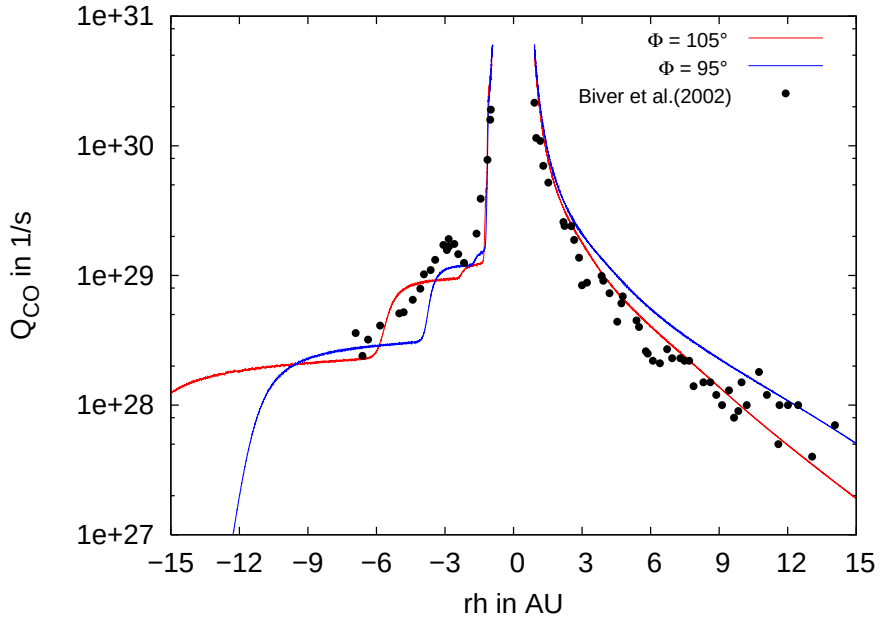

Figure 4.6: Similar CO plot as in Fig. 4.4. The importance of the argument of the subsolar meridian at perihelion Φ for the CO production curve is demonstrated. Changing the argument by 10° shifts the outgassing curve, because the illumination conditions of the different latitudes throughout the orbit change. The obliquity was throughout this paper 84°. The argument Φ and the obliquity enter the calculation of the solar zenith angle ζ (Sekanina 1979). Figure from Gortsas et al. (2010a).

moving boundaries. Surface erosion due to surface sublimation leads to a moving boundary which is resolved by applying a temperature remapping technique. This approach allows to take properly into account the loss in the internal energy of the eroded surface layers. Such moving boundary techniques are referred to as Stefan problems. They are important if the thermal conductivity is low as was the case in this investigation and as has been estimated in Section 2.2.

Our approach is guided by recent observational findings on important parameters controlling cometary activity. A low thermal conductivity (Kührt 1999, Groussin et al. 2007), the obliquity of the rotation axis (Jorda et al. 1997), the chemical heterogeneity (Lederer and Campins 2002, Bockelée-Morvan et al. 2009), and the CO jet at a latitude of 20° (Bockelée-Morvan et al. 2009) have been incorporated to calculate the water and CO activity.

For the first time, a thermal model is applied to the full data set of the water and CO production rates as reported by Biver et al. (2002). The data set covers the heliocentric range from -7 AU pre- to 15 AU postperihelion. There was no need to include amorphous ice into the model. The following results were obtained:

- The measured water production rates are well reproduced by the model. It is assumed that the active spots are distributed randomly over the whole nucleus.

- The CO production curve fits the observations over the whole heliocentric distance

starting at -7 AU to 15 AU very well. In agreement with recent reports by Bockelée-Morvan et al. (2009) about a CO source at a latitude of 20° the best fit to the observations was obtained if CO activity is confined to the positive hemisphere above a latitude of 0°. Around -2 AU preperihelion, the model approximates the local peak of the CO observations by a plateau. The CO fit along the postperihelion branch is very well.

- A low thermal conductivity of 0.01 W $K^{-1}m^{-1}$ is in good agreement with the Hale-Bopp observations.

In conclusion, currently there are two different approaches to model the outgassing pattern of Hale-Bopp for water and CO as reported by Biver et al. (2002). The approaches of Enzian (1999), Capria et al. (2002), and Prialnik (1997b) on the one hand. These models rely on the assumption that some form of amorphous ice must be present in the comet, that a certain percentage of CO must be trapped in the amorphous ice matrix which is released after phase transition, and that there is a certain percentage of CO bulk ice. On the other hand, the approach of this paper which tries to incorporate as many observational findings of the recent years as possible and which relies only on CO bulk ice.

Finally, the importance of the argument Φ of the subsolar meridian at perihelion for the CO production curve has also been demonstrated. The argument Φ and the obliquity of the comet determine the distribution of the incoming solar energy on the nucleus surface. Changing Φ by a value of 10° shifts the CO production curve clearly.

After having successfully reproduced the production rates of CO and to a certain degree also for water the thermal model is applied to predict the CO and water activity of ESA's Rosetta target comet CG.

5 Thermal model of 67P/Churyumov-Gerasimenko

5.1 Introduction

The European Space Agency's Rosetta spacecraft was launched on March 2, 2004 to the Jupiter family comet 67P/Churyumov-Gerasimenko (CG hereafter). It is designed to perform a series of experiments at the comet and on its surface as described in more detail in Glassmeier et al. (2007). These experiments are going to provide a unique insight into the state and evolution of comets. The anticipated data base is going to improve our knowledge of comets in particular and the Solar System in general. Among many other experiments the temporal and spatial characteristics of activity and temperature depth profiles will be measured. To be prepared to interpret the expected data thermophysical simulations of comets are required.

In contrast to Hale-Bopp, CG is a short period comet with an orbital period of 6.45 years and a perihelion distance of 1.25 AU[1]. Short period comets are defined by a Tisserand parameter T_J above 2. Their orbits are typically close to the ecliptic which is also the case for CG with an orbital inclination[1] of 7 °. Short period comets appear to have their origin in the trans-Neptunian region at heliocentric distances of about 10 to 50 AU. Through planetary perturbations comets are scattered in the inner planetary region. According to Fernández (2007) the orbital parameter most affected by planetary perturbations is the semimajor axis *a* and thus the orbital energy of the comet.

CG was discovered in 1969 and has been observed during 6 apparitions; the latest apparition was 2002-2003. The radius of the comet has been estimated by different techniques. Lamy et al. (2007) derived a value of 2 km from Hubble space telescope observations which is in agreement with radii derived from ground-based observations by Kamoun et al. (1998), and Tancredi et al. (2000). Lamy et al. (2007) also derived the diurnal rotation and gave a value of 12.4 h.

5.2 Observations

Comet CG has not been studied so extensively as comet Hale-Bopp. After ESA's decision to postpone the launch of Rosetta to comet 46P/Wirtanen in early 2003 and the selection of CG as the new target the interest in this comet intensified.

[1] JPL Small-Body database: ssd.jpl.nasa.gov

Only few values for the water production rate of this comet close to perihelion are available. Schleicher (2006) reported about observations of CG at the Lowell Observatory during the 1982/83 (Osip et al. 1992) and 1995/96 apparitions. The published production rates cover a heliocentric range from 1.48 pre- to 1.86 AU postperihelion. The peak water production occurred one month after perihelion passage and reached a value of $\approx 8 \times 10^{27} s^{-1}$. This outgassing strength corresponds to an active surface fraction of 3-4 % as reported by Schleicher (2006).

For CO there are no observations available. Bockelée-Morvan et al. (2004) gave an estimate of CO production at around 3 AU which is very vague so that it will be neglected in this thesis. Therefore, it is assumed that CO outgassing is uniformly distributed as water outgassing. The same value for the fraction of active surface areas which is important for Eq. 4.1 is used for CO as for water.

5.3 Results

The nucleus model of CG is characterized by a multi-component nucleus with two volatile species, i.e. water and CO ice. A two-layer stratigraphy is assumed with the upper layer being a mixture of water ice and dust while the lower layer of water ice, dust, and CO ice. For comet CG the same mass fractions have been used as for comet HB summarized in Table 4.2. Constant initial conditions for the temperature field were assumed while the density field was set to the thermal equilibrium values. This is justified by the short period of the comet. The temperature remapping technique to account for lost surface layers is taken into account. In the plots this method is referred to as Stefan problem (SP). The obliquity of the comet as reported by Lamy et al. (2007) is also included. The values for the obliquity and the argument of the subsolar meridian can be found in Table 3.1. Activity is calculated with Eq. (4.1) through integration over the whole spherical nucleus. The water ice sublimation curves are calibrated against observations at perihelion as reported by Mäkinen (2004) and Schleicher (2006) leading to an active surface area of about 3% of the total surface. This value for the active surface area is in good agreement with Schleicher (2006).

The calculations are run for several perihelion apparitions until a steady-state solution is reached. This is necessary in order to become independent from the initial conditions and to simulate short period comets. Steady-state is reached when curves of two consecutive perihelion passages exhibit no deviations. All shown curves are in this sense equilibrated.

The orbital parameters can be found in Table 3.1. The physical constants for water, CO, and dust are summarized in Table 2.1.

5.3.1 Thermal flux

The discussion of the simulation results starts with Fig. 5.1 and Fig. 5.2 showing the thermal flux through the surface for a single diurnal rotation at perihelion and aphelion. The thermal flux is plotted for an active surface point in the equatorial plane and the results are compared with and without the temperature remapping technique, that is the Stefan problem (SP). Such a comparative study is followed for comet CG in distinction

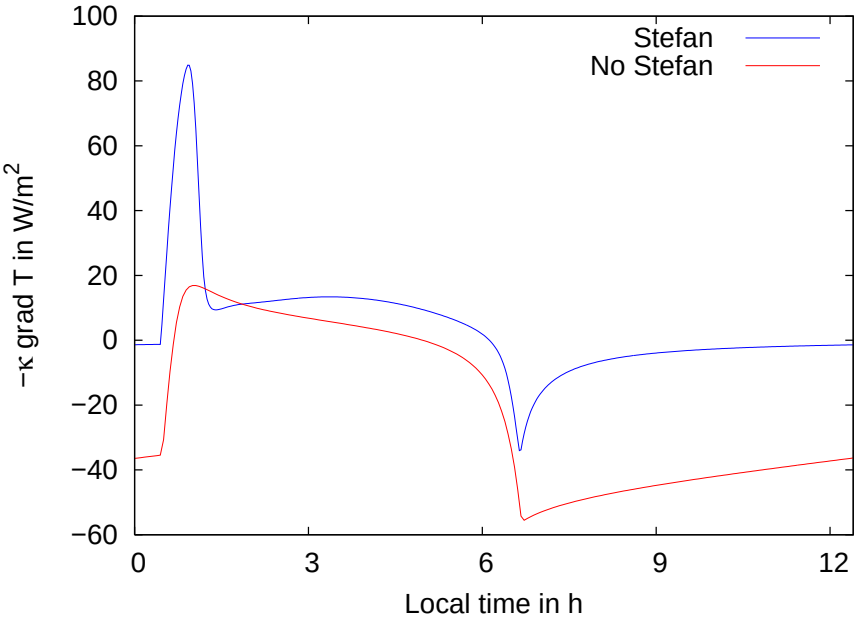

Figure 5.1: Thermal flux through the surface of comet CG for an active spot in the equatorial plane for one diurnal rotation at perihelion. For comparison the thermal flux without the temperature remapping technique is also shown. The Stefan problem accounts properly for the lost internal energy of the eroded sub-surface layers through the temperature remapping technique, see Eq. (2.30). Therefore, the nucleus is much colder in the solution with the SP leading to a larger thermal flux into the nucleus during noon at around 3 h when surface sublimation reaches its peak value. Without the SP continuous heating of the nucleus leads to a steady decline of the peak value at dawn. During the night the solution with the SP conducts less thermal energy to the surface because of a colder nucleus.

to comet Hale-Bopp because for the former temperature depth profiles are going to be measured during the Rosetta mission. It will be shown that the Stefan problem strongly modifies the thermal flux at the surface and the temperature depth profiles.

At dawn, the sub-surface layers are relatively cold. Therefore, the thermal flux into the body is in both cases relatively high. In the solution with the temperature remapping technique layers that are warmed as the active point approaches the subsolar point are eroded. With increasing surface erosion the surface recedes to greater depths. Inner less warm regions come to the surface. Hence, continuous warming of the sub-surface layers becomes virtually impossible. To reduce the relative large temperature difference, thermal flux into the body increases as the surface point moves towards noon when surface sublimation reaches its peak value. The loss process of internal energy of the eroded sub-surface layers is properly accounted for by the temperature remapping technique.

Without the SP thermal flux through the upper boundary is continuously declining. The initially large temperature gradient is reduced through continuous heating of the sub-surface layers, which are retained in this mode. The temperature remapping technique is not applied on the temperature field. Therefore, the internal energy budget of the nucleus

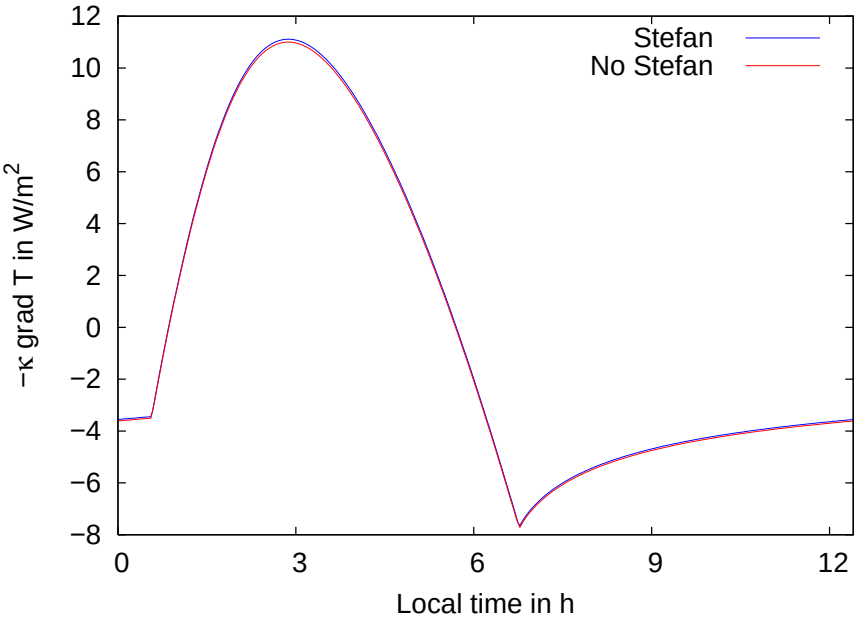

Figure 5.2: Thermal flux plot as in Fig. 5.1 but at aphelion. CG's aphelion position is 5.6 AU. At these heliocentric distances energy input from the Sun is low and surface sublimation is negligible. Hence, surface erosion due to sublimation is negligible. The solutions with and without the Stefan problem are the same.

is not altered. Despite the fact that the surface boundary is moving towards the CO front. The assertion is that the amount of internal energy in the eroded sub-surface layers is small and therefore it should not much affect the production curves of CO and water. Later on, it will be demonstrated that this is generally not a valid approximation.

Towards dusk the two curves converge again as a result of weak surface erosion. During the night, the solution of the SP provides less thermal energy to the surface due to a colder nucleus. At aphelion, surface erosion is negligible. As is shown in Fig. 5.2 the thermal flux curves with and without the SP are essentially the same.

Table 5.1: The thermal conduction coefficient κ employed in this chapter.

Thermal conduction coef. κ	κ_1	κ_2	κ_3
Value [W m^{-1} K^{-1}]	10^{-3}	10^{-2}	10^{-1}

5.3.2 Temperature depth profiles

The temperature as function of depth for an active surface element in the equatorial plane are displayed in Fig. 5.3 and Fig. 5.4 at perihelion and aphelion, respectively.

At perihelion, strong surface erosion due to surface sublimation brings fresh and cold material to the surface. The mechanism appears to consist of several steps and shall be

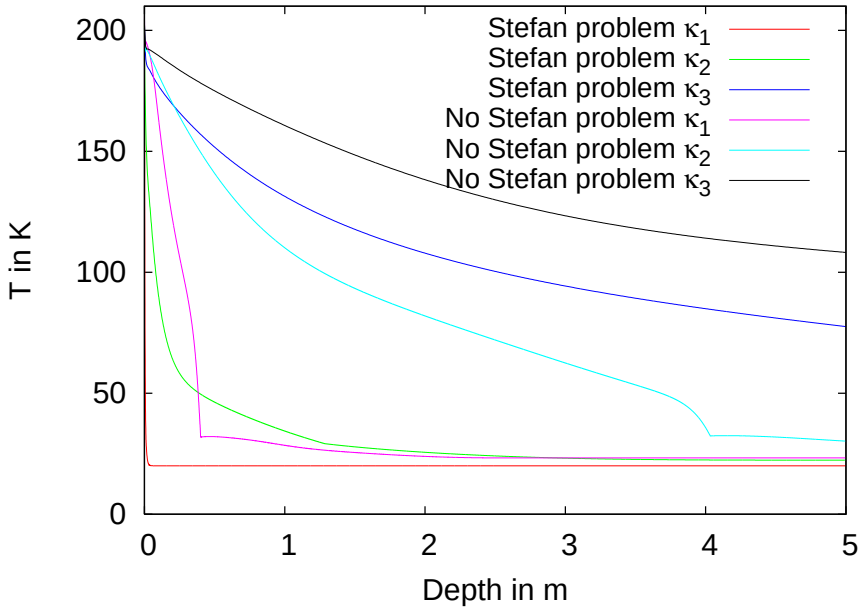

Figure 5.3: Temperature depth profiles at perihelion. The corresponding active point is located in the equatorial plane. The local time is noon. At perihelion water ice sublimation and thus surface erosion is strong leading to a substantially less heated nucleus. The temperature depth profiles of the SP solution are generally cooler than in the solutions without the SP. The step structure indicates the location of the CO front which acts as a cooling devise preventing a further heating of deeper layers. Increasing the thermal conduction coefficient pushes the CO front several meters below the surface, see also the CO depth plot in Fig. 5.7. The thermal conduction coefficient is given in Table 5.1.

described first for the arc of increasing surface sublimation. This is the case when the active surface point moves from the night side to the day side. At dawn surface sublimation is weak. The surface and sub-surface layers are warmed. With increasing surface activity these (sub-)layers are lost for the nucleus due to erosion. As the internal energy of these sub-surface layers is lost most of the incoming solar energy that is transported into the nucleus is used to warm the now new and cold surface and subsurface layers. With increasing surface activity these layers which recently adapted to the surface conditions are lost. Hence, the process has to start in principle again. The process is stopped when surface sublimation has passed its peak value at around noon and subsides during the night. Along the arc with declining surface activity the loss process of heated sub-surface layers is getting weaker. A gradual warming of the nucleus is now possible. This energy, however, is partly lost during the night side due to thermal emission at the surface.

This mechanism leads at perihelion to much steeper temperature depth profiles as is shown in Fig. 5.4. Second the position of the front of volatile materials like CO in this calculation is getting close to the surface. The actual position of the CO front depends on the choice of the thermal conductivity. A low value of κ brings the CO front close to the surface. The CO depth in the calculation with the Stefan problem is only 7 % of the CO depth without the Stefan problem for a $\kappa = 10^{-3}$ W m^{-1} K^{-1}. This figure rises to 28 % for

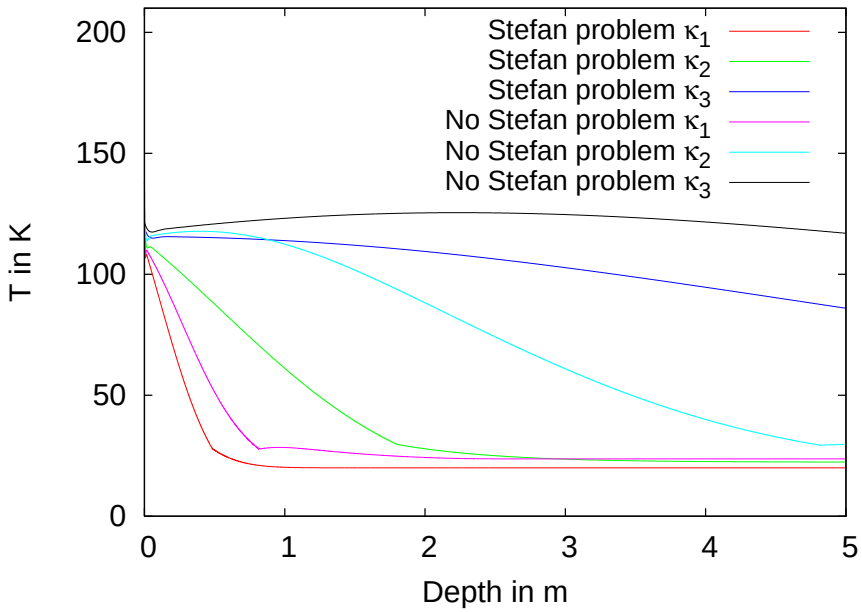

Figure 5.4: Temperature depth profiles as in Fig. 5.3 at aphelion. Surface sublimation and thus surface erosion is negligible. The solutions with and without the SP converge close to the surface. At greater depths memory effects are visible as a result of a different thermal evolution during perihelion passage. A high thermal conductivity leads to a warmer nucleus. The CO front is several meters below the surface. The thermal conduction coefficient is given in Table 5.1.

$\kappa = 10^{-2}$ W m^{-1} K^{-1}. In the calculation without the Stefan problem the adaptation of the sub-surface layers to the surface conditions is continuous. The temperature remapping technique is not applied. Therefore, the internal energy of the sub-surface layers is retained allowing an energy transport into deeper layers. Therefore, the temperature depth profiles without the Stefan problem generally show higher temperatures. The assumption to neglect the Stefan problem is that the internal energy in the sub-surface layers is small compared to the energy conducted from the surface into the nucleus. Around perihelion, this assumption is apparently not well justified. This conclusion appears to be also independent from the thermal conductivity.

At aphelion, sublimation of water ice is low and therefore surface erosion. Consequently, the SP should not much alter the temperature depth profiles of CG. Figure 5.4, however, shows strong differences between calculations with and without the Stefan problem. In this context it is important to distinguish two different regimes. The layers close to the surface in the range of cm are coupled to the surface rather strongly. In these layers the temperatures for the two modi converge well as can be expected due to the negligible Stefan problem. At larger depths, in the range of several cm to m the temperature distribution depends on the thermal history of the nucleus. Figure 5.3 shows that around perihelion the nucleus exhibits a different thermal evolution depending whether the Stefan problem is taken into account and also what thermal conductivity was employed. A low thermal conductivity leads to smaller differences in the thermal history of CG there-

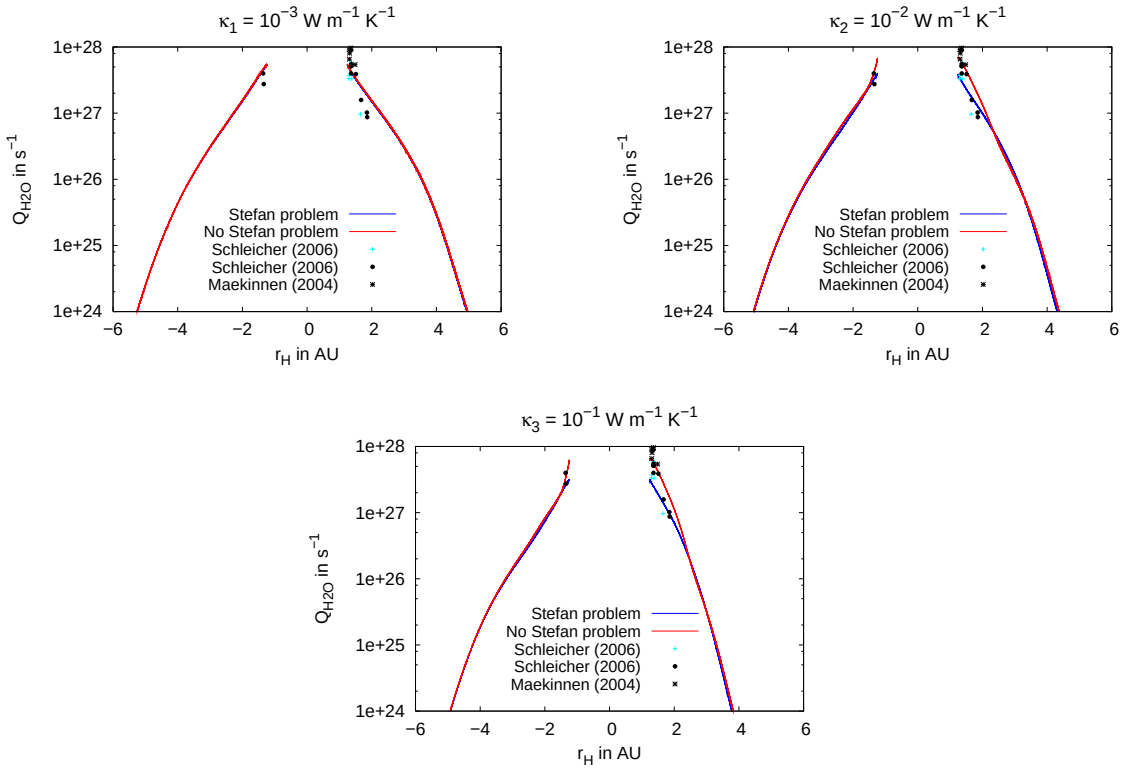

Figure 5.5: The water outgassing curve as function of heliocentric distance with the temperature remapping technique labelled as Stefan problem. For comparison the solution without the Stefan problem is also displayed. For low thermal conductivities the water outgassing curve is not much affected. Increasing the conductivity leads to less water outgassing in the Stefan problem solution. See Sections 5.3.3 and 5.3.4 for a detailed discussion.

fore the temperature depth profiles with and without the Stefan problem tend to converge better than those with higher κ values.

5.3.3 Sublimation curves of water and CO ice

The activity of water and CO ice, and the CO depth profiles for a thermal conductivity of 10^{-3} W m^{-1} K^{-1} are displayed in Fig. 5.5, in Fig. 5.6, and in Fig. 5.7, respectively. For comparison, the solution without the temperature remapping technique, labeled as no Stefan problem, is also shown.

The water sublimation curve is symmetric with respect to perihelion and not much affected by the SP. In contrast to that, the CO sublimation curves exhibits a distinct asymmetry between the pre- and the postperihelion leg. In the range from aphelion to 3.9 AU preperihelion surface erosion is weak. The thermal wave penetrates the sub-surface layers and through continuous heating during the day pushes the CO front to greater depths. In both modi the maximum distance to the surface is reached at around 3.9 AU, see Fig. 5.7.

From 3.9 AU to perihelion, surface sublimation increases and exceeds the CO sublimation rates. Therefore, both modi bring the CO front closer to the surface. But only in

the calculation with the SP is the internal energy of the comet reduced by the amount of internal energy of the eroded sub-surface layers. This is achieved by applying the temperature remapping technique Eq. (2.30). This reduction in internal energy prevents a continuous heating during the day. It leads to a substantially less heated comet as discussed in Section 5.3.1 and 5.3.2. As a result the surface of the comet is moving towards the CO front but the amount of energy reaching the CO front remains almost constant. Hence, the CO outgassing curve shows along the preperihelion branch an almost constant course. Only close to perihelion when the CO front is almost at the surface, compare Fig. 5.7, CO production starts to increase reaching a peak value at perihelion comparable to the solution without the SP.

In the calculation without the SP the reduction of internal energy is neglected. The temperature remapping technique is not applied. Therefore, the calculation without the SP shows a continuous heating of the nucleus during the day. The CO front is effectively supplied with thermal energy leading to high sublimation rates and a deeper CO front, see CO plot in Fig. 5.7. As Fig. 5.6 shows the CO sublimation curve without the SP exhibits a liftoff which occurs exactly at around 3.9 AU. After perihelion, both CO sublimation curves exhibit a very similar progression. The CO depth curves, however, show a retardation effect. The solution without the SP reaches its minimum distance to the surface around 0.6 AU after the solution with the SP. This is a consequence of a deeper CO front and the continuous heating along the incoming branch in the solution without the SP which created warmer sub-surface layers. As the comet passes 2 AU water sublimation is rapidly declining which allows the CO front to recede almost in parallel for both modi. The effect of the SP is shrinking so that the amount of energy reaching the CO front increases. Therefore, the CO production is comparable to its counterpart without the SP solution. The fact that both modi produce a similar progression of the CO curve along the postperihelion branch is the result of the low κ value. Figure 5.6 shows the CO curves for higher κ values which show clear differences also along the postperihelion branch between the calculations with and without the SP. de Sanctis et al. (2006) studied CG with their thermal model obtained a similar water gas production curve as shown in Fig. 5.5. With respect to CO their model predicts a flat CO production curve.

5.3.4 Influence of the heat conductivity κ

The heat conductivity κ is a key parameter for the thermal evolution of comets. Huebner (2008) recently summarize that this very important parameter is not well constrained. Due to this uncertainty and the discussion in Section 2.5 several cases covering values from 10^{-3} W K^{-1}m^{-1} to 10^{-1} W K^{-1}m^{-1} were investigated.

The thermal conductivity is not only important for the amount of heat that is transported into the nucleus at daytime and released at night but it also controls the amount of eroded surface material and the energy loss due to surface erosion. The penetration number χ also depends on this parameter. According to this quantity low thermal conductivities make it necessary to treat the evolution of the comet as a Stefan problem. For higher values, χ is small indicating that the Stefan problem might not be so important for the thermal evolution of the comet.

We have seen in the previous section that the CO sublimation pattern is strongly modified by the SP problem especially along the preperihelion branch while the water subli-

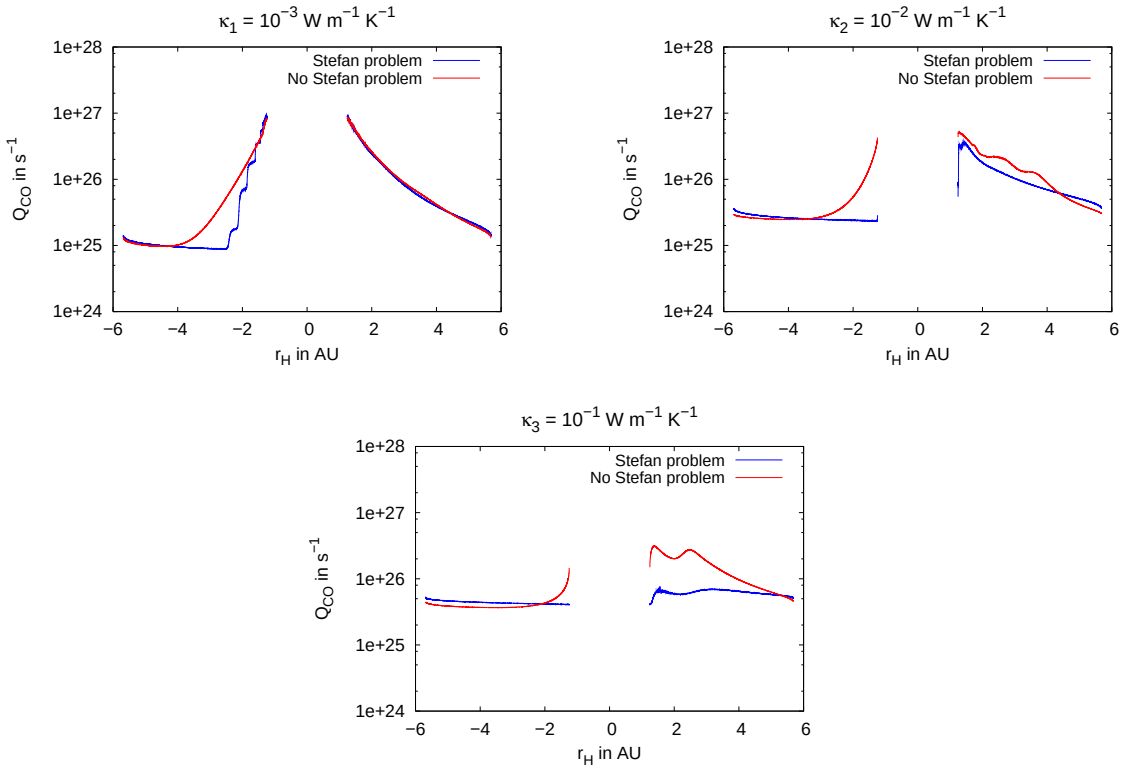

Figure 5.6: Similar plot as in Fig. 5.5 for CO. Surface erosion due to surface sublimation leads to escaping surface material. The internal energy of these layers is lost for the system. Therefore, less thermal energy can reach the CO front leading to a stalled CO outgassing along the preperihelion branch in which water sublimation at the surface increases. At perihelion the CO has come very close to the surface causing a peak in CO outgassing. Along the postperihelion branch water sublimation is declining reducing surface erosion and thus the obstruction of the diurnal heat wave is getting weaker. High thermal conductivities lead to less CO activity with the tendency to converge to a flat CO production curve. See Sections 5.3.3 and 5.3.4 for a detailed discussion.

mation curve exhibits only small differences for a low thermal conductivity, e.g $\kappa_1 = 10^{-3}$ W $K^{-1}m^{-1}$. The situation is different for a relative high thermal conductivity as shown in Fig. 5.5. Increasing κ generally reduces the water sublimation rate throughout the orbit because more energy is conducted into the nucleus. This is the case with and without the Stefan problem if the water curves of the same modi are compared. Second, the water production curve of the solution with the temperature remapping technique is below its counterpart without the SP around perihelion at the postperihelion branch.

A large value in the thermal conductivity increases the energy conduction into the nucleus. Inside the nucleus water bulk sublimation cools the nucleus and thereby increases further the thermal flux from the surface into the nucleus. Therefore, less energy is available for surface sublimation. The SP problem adds to this effect. A high value of κ means that the internal energy of the eroded layers is higher than their counterparts with a small thermal conductivity. Hence, more energy is lost if these layers are eroded. Colder subsurface layers are brought to the surface which increase further the thermal flux into the

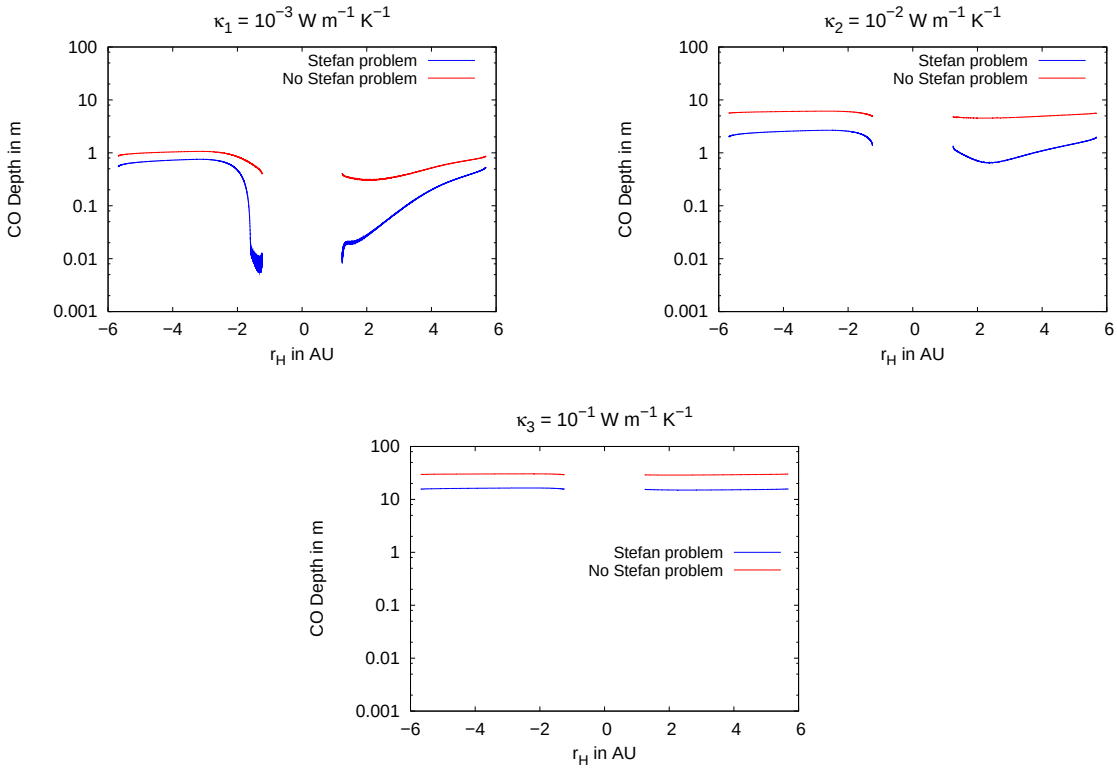

Figure 5.7: Similar plot as in Fig. 5.5 for the depth of the CO front. Low thermal conductivity: Along the preperihelion branch two intervals can be discerned. From aphelion to 3.9 AU water sublimation is lower than CO sublimation. The CO front moves to greater depths. From 3.9 AU to perihelion water sublimation exceeds CO bringing the CO front closer to the surface. In the calculation with the Stefan problem the temperature remapping technique leads to a colder nucleus. Therefore, CO comes closer to the surface. Neglecting the temperature remapping technique leads to a warmer nucleus. Hence, the CO front remains at larger depths. Higher thermal conductivities push the CO front several meters from the surface. See Sections 5.3.3 and 5.3.4 for a detailed discussion.

nucleus. Hence, less energy is available for water sublimation at the surface. The water production curve with the solution of the SP is below its counterpart without the SP. This result has already been encountered in Section 3.2.6 for a simple comet model.

Further away from perihelion the SP becomes less important. The differences in the water sublimation curves become smaller. In the SP solution the comet is colder even with a relative high thermal conductivity. Therefore, the water sublimation of the SP solution is below its counterpart without the SP also far from perihelion. The energy coming back to the surface during the night is mostly re-radiated and not relevant for water sublimation.

Increasing the thermal conductivity starts to decouple the CO sublimation from the current position of the comet relative to the Sun as is displayed in Fig. 5.6. The CO sublimation curve of the SP solution is getting flat. The solution without the SP exhibits a stronger maximum around perihelion but the peak is less pronounced compared to the low thermal conductivity solution. There is the tendency visible to converge to a flat CO profile with increasing heat conductivity.

It is also interesting to notice that for a low κ the differences between the CO curves of the solution with and without the Stefan problem were confined in the preperihelion branch as is displayed in Fig. 5.6. Higher κ value appears to move these differences to the postperihelion branch. For a high κ value of 10^{-1} W K^{-1}m^{-1} the preperihelion curves show until before perihelion the same course with quantitative differences while along the postperihelion branch the differences become quite pronounced. The intermediate κ value of 10^{-2} W K^{-1}m^{-1} further corroborates this conclusion.

A low κ value keeps the CO front rather close to the surface as is shown in Fig. 5.7. Therefore, during perihelion approach the CO front can be brought rather fast close to the surface in both modi.

A higher κ value, however, pushes the CO front several tens of center meters or even meters deep into the nucleus. During perihelion approach the CO front is brought closer to the surface in both modi but its minimum distance to the surface is reached after perihelion passage when water sublimation starts to decline again. Thermal energy can then reach the CO front and cause higher sublimation rates. The CO depth plots in Fig. 5.7 corroborate this conclusion. The Stefan problem prevents strong CO sublimation because of surface erosion which is around perihelion strong even if the nucleus is on the postperihelion branch. Therefore, the CO curve of the Stefan problem solution tends faster to the flat CO profile.

The value of the thermal conductivity has a strong impact on the results in both solutions with and without the SP. It is shown that with an increasing value of κ the CO sublimation pattern starts to decouple from the processes taking place at the surface. In other hand, the SP problem has an increasing influence on the water sublimation pattern with increasing thermal conductivity.

Going back to the length scale estimates of Section 2.2 which motived the approach to study the Stefan problem in more detail the conclusion that the Stefan problem appears to be also important for higher thermal conductivities is new. For higher κ values the penetration number χ is rather low as listed in Table 2.2. Apparently, the Stefan problem is more complex than the simple but intuitive discussion on the characteristic scales of Section 2.2. The loss in internal energy of the eroded sub-surface layers is not included in the discussion of Section 2.2. But as the present discussion has shown this energy is important and it leads to the effect that with increasing κ the water sublimation at the surface with the Stefan problem starts to deviate from the solution without the Stefan problem which was not the case for low thermal conductivities, e.g. 10^{-3} W K^{-1}m^{-1}.

5.3.5 Comparison with observational data

Unfortunately, there are only few observations of water for comet CG which are mainly confined to the perihelion region. Therefore, it is difficult to compare the model results with observations. However, to discriminate between models and parameters, observations at large heliocentric distances are necessary.

Hanner et al. (1985), Osip et al. (1992), Crovisier et al. (2002), Mäkinen (2004), and Schleicher (2006) provide water production rates of CG around perihelion. The data points of Schleicher (2006) for the 1982/1983 observational campaign, referred to as Schleicher I, and for the 1995/96 apparition, referred to as Schleicher II, together with the SWAN data of Mäkinen (2004) are plotted in Fig. 5.5. The data, however, allow to

derive the fraction of active surface areas which is important of for Eq. (4.1). A value of 3 % was employed to match the observations at perihelion which is in good agreement with Schleicher (2006).

5.4 Conclusion and outlook

The thermophysical model developed in Chapter 2.4 is applied on CG the target comet of ESA's Rosetta mission. Thermal flux, temperature depth profiles, and activity of water and CO are studied. The influence of the thermal conductivity as a key yet poorly constrained parameter has been studied. The nucleus model consists of a multi-component comet with water ice, dust, and CO ice. The novel feature of this model is the self-consistent treatment of surface erosion as a moving boundary value problem (Stefan problem) with a rigorous treatment of the internal energy loss process due to ablation. The importance of the Stefan problem is worked out in detailed. The model accounts for heat conduction and advection, gas diffusion, sublimation, and condensation processes in a porous multi-component nucleus with moving boundaries. Seasonal effects were also taken into account.

The SP leads to a considerably less heated nucleus with the following consequences for the thermal flux and the temperature depth profiles at perihelion and aphelion.

- At perihelion, the thermal flux at the surface is much larger in the SP solution compared to the solution without the SP. At aphelion, surface sublimation is negligible. Therefore, the thermal flux in the solutions with and without the SP are the same.

- The temperature depth profiles with the SP are generally cooler compared to the results obtained without the SP. This is the case independent from the thermal conductivity and the position of the comet relative to the Sun.

The effect of the SP on the activity of water and CO gas depends on the value of the thermal conduction coefficient. For low thermal conductivities, e.g. 10^{-3} W $K^{-1}m^{-1}$, it can be summarized:

- Water sublimation of the SP solution is slightly below the solution without the SP.

- The CO activity in the SP solution exhibits a characteristic asymmetry with respect to perihelion. The incoming branch shows an almost stagnating CO production while the post perihelion branch exhibits a decline in analogy to the declining solar irradiation at the surface. In contrast to that, the CO sublimation curve without the SP is symmetric with respect to perihelion and its course follows the solar irradiation of the surface with a peak value at perihelion.

- The SP brings the CO front close to the surface at perihelion while without the SP the CO front remains several tens of cm below the surface.

Increasing the thermal conductivity to a value of 10^{-1} W $K^{-1}m^{-1}$ leads to the following results:

- Water sublimation of the SP solution takes only 70% of the solution without the SP around perihelion. This reflects a more effective cooling mechanism of the SP with a larger thermal conduction coefficient.

- Along the preperihelion branch the CO curves with and without the Stefan problem are flat with small quantitative differences until before perihelion. Along the post-perihelion branch both CO curves exhibit a peak value. But in the solution with the Stefan problem the peak is less pronounced. The minimum distance of the CO front from the surface is reached after perihelion passage.

Hence, in case of a small thermal conductivity the SP has a small effect on surface sublimation of water ice and a strong impact on CO sublimation inside the nucleus especially along the preperihelion branch.

In case of a high thermal conductivity the Stefan problem has a larger effect on surface sublimation of water ice. The CO front with the Stefan problem converges faster to a flat CO profile. As result there are differences in the CO curves with and without the Stefan problem along the postperihelion branch but the tendency is to converge to a flat CO production curve in both modi.

For low values of the thermal conductivity, Rosetta should measure a steep temperature gradient below an active area mainly near perihelion. Even at strong solar insolation the temperatures are extremely low directly below the surface since the cold CO front is located at a depth of only some centimeters. This would also mean that other volatiles and amorphous ice, if it does exist, are present near the surface and one could possibly find pristine matter in shallow depths.

6 Hybrid plasma simulation model

The hybrid plasma simulation technique employed in this thesis to calculate the plasma environment of weak comets is presented. The model was developed by Bagdonat and Motschmann (2002) and already applied to study various aspects of the interaction between the solar wind and weak comets, e.g. 46P/Wirtanen und CG. As part of this thesis the code is applied and extended to study the plasma environment of CG in more detail by including results from the thermal modeling of the nucleus. In this introductory chapter, the model and few aspects of its implementation are discussed.

6.1 Introduction

The study of the solar wind-comet (SW-C hereafter) interaction was initiated by observations of comets when Biermann (1951) drew the conclusion that the orientation of cometary ion tails in almost anti-sunward direction indicate the existence of a radially streaming plasma flow originating in the Sun, the solar wind. This flow of protons, electrons, and a small fraction of other ionized particles propagates with supersonic and super-Alfvénic velocity in the range of 300-1500 km s^{-1}. Its most important feature is its state of magnetization. The solar wind is a complex plasma flow which is subject to many variations in density, flow velocity, and other observables.

The interaction of the solar wind with comets has been studied through spacecraft missions and models in the past three decades. For reviews consult Neugebauer (1990), Coates (1997), and Coates and Jones (2009). Several missions with instruments suitable for studying the plasma environment of comets were flown to comet 21P/Giacobini-Zinner (GZ), 1P/Halley, 26P/Grigg-Skjellerup (GS), and 19P/Borelly. The data acquired from these missions together with theoretical models have improved our understanding of the SW-C interaction.

Analytical models provide basic but still very important insights into structure and magnitude of the effects to be expected (Biermann et al. 1967, Mendis and Flammer 1984). Magnetohydrodynamics (MHD) and multi-fluid models constitute a very efficient method to study the global structure of the plasma environment of strongly outgassing comets (Wegmann et al. 1987, Bogdanov et al. 1996, Gombosi et al. 1996, Hansen et al. 2007, Benna and Mahaffy 2006). In this regime, close to perihelion, the characteristic length scale of the solar wind-comet interaction is large compared to the gyroradius of the heaviest particles and thus a fluid description is appropriate. Results from MHD models were used to study ion chemistry of comets 1P/Halley by Rubin et al. (2009), Hale-Bopp, and Hyakutake, and other studies of the plasma environment of 1P/Halley. However, for low cometary production rates, as reported by Schleicher (2006) for CG, where the

extension of the coma is small compared to the large gyroradius of the heaviest considered species, a kinetic description provides valuable insights into the plasma environment of comets (Lipatov et al. 2002, Motschmann and Kührt 2006). Hybrid models treat the dynamics of the solar wind ions and cometary ions kinetically while retaining a fluid description for the electrons. The hybrid model resolves the velocity distribution function of protons and cometary ions thus enabling to study kinetic effects due to a non-equilibrium velocity distribution.

The outgassing strength of the nucleus is an important input parameter of plasma simulations. It determines the size and nature of the interaction region. The thermal modeling part of the thesis has taught us that cometary activity increases by several orders of magnitude as the comet approaches the Sun. The most abundant species close to the Sun in the evolving coma which increases from few km to thousands or even millions of km is water vapor (Krankowsky et al. 1986). Freshly born neutrals expand with supersonic velocity radially away from the nucleus which can exert only a negligible gravity attraction. The neutral particles can ionize either by photoionization or charge exchange. The ionized particles immediately start to interact with the solar wind. The new born ions are accelerated by the convective electric field and perform a cycloidal motion gyrating around the magnetic field. This cycloidal motion translates to a ring in velocity phase space which is unstable and leads to the production of plasma waves. These waves scatter the particles in pitch angle to a shell in velocity phase space. Then this shell is thickened and if enough time passes the velocity shell distribution becomes a Maxwellian around the local solar wind velocity (Motschmann and Glassmeier 1993a, Coates et al. 1993). Conservation of momentum and energy thus leads to the transfer of energy from the solar wind to the pick-up currents and to waves (Motschmann and Glassmeier 1993b, Glassmeier et al. 1993). Continuous deceleration of the solar wind by mass loading is possible only until the mean molecular weight of the plasma particles reaches a critical value (Biermann et al. 1967). At this point a weak shock forms decelerating the plasma flow to subsonic velocities. The spatial heterogeneous mass loading pattern leads to a draping of the magnetic field frozen in the solar wind flow around the obstacle on large scale. The draped magnetic field organizes the heavy cometary ions to form the plasma tail.

An interesting feature of comets is the fact that their coma is growing as they approach the Sun and that the coma is comprised of many species. Depending on the heliocentric position of the comet different ion species are dominating the coma. The growing coma creates a very different obstacle to the solar wind flow. Several AU from the Sun cometary activity is in general very low. The solar wind is hitting a bare nucleus while close to the Sun the coma covers hundred of thousands of km. This unique laboratory will be simulated in this thesis. It is thus the coma which poses a special kind of obstacle to the solar wind as the cometary nucleus provide little impediment to the solar wind flow (Keller et al. 1986a).

In the hybrid model, main aspects of this very complex and here only broadly described phenomenon are modelled. Important ingredients of the cometary part of the SW-C interaction are the outgassing strength, the activity pattern, and the ionization process. The dynamics of the cometary ions are treated in complete analogy to the solar wind protons in the macroparticle approach. Newtonian equations of motion with the Lorentz force as the main driving force are solved. The cometary electron population is add as another contribution to the solar wind electron fluid with a much lower temperature.

6.2 Material theory I - ion dynamics

The mean free path of solar wind particles is several AU large exceeding the characteristic scale lengths of the SW-C interaction of 10^6 to 10^9m by 5 to 3 orders of magnitude as argued by Axford (1962). Therefore, the solar wind plasma can be regarded as collision free. For weak comets and for the scale lengths which the hybrid code resolves the assumption of a collision free plasma should also be valid in the vicinity of the nucleus.

A general formalism for the description of an ensemble of particles is given by the Liouville equation allowing to calculate the time evolution of the phase space probability density F for a given Hamilton function $\mathcal{H}$ and appropriate initial conditions (Cap 1970)

$$\frac{dF}{dt} = \frac{\partial F}{\partial t} + \{\mathcal{H}, F\}\,. \tag{6.1}$$

The curly brackets denote the Poisson brackets. This equation serves as a starting point for different levels of approximations to obtain a statistical description of a wide range of phenomena. Among them is also the statistical description of a collision free plasma, the so called Vlasov plasma. To derive the Vlasov equation from Eq. (6.1) it is assumed that no direct particle interaction can occur between the constituents of the plasma and that the particles obey the canonical equations for a given electromagnetic field. In this case, the distribution function disentangles to a product of 1-particle distribution functions f. The derived equation is the Vlasov equation (Cap 1970)

$$\frac{\mathrm{d}f}{\mathrm{d}t} = \frac{\partial f}{\partial t} + \dot{\mathbf{q}} \cdot \nabla_q f + \dot{\mathbf{p}} \cdot \nabla_p f = 0\,. \tag{6.2}$$

q and p denote the canonical coordinates and momenta, respectively. In this investigation the canonical variables are the spatial coordinate $q = x$ and the velocity of the particles $v = p/m$. The mass is assumed to be constant as the velocities in the plasma are well below 0.1 of the light speed. In the hybrid code the Vlasov equation is not solved directly. Instead, the characteristics of this equation are solved which provides an equivalent description. These are mainly Newtonian equations of motion with the Lorentz force and a drag force

$$\begin{aligned}
\frac{\mathrm{d}}{\mathrm{d}s}t &= 1\,, \\
\frac{\mathrm{d}}{\mathrm{d}s}\mathbf{x}_\mu &= \mathbf{v}_\mu\,, \\
\frac{\mathrm{d}}{\mathrm{d}s}\mathbf{v}_\mu &= \frac{q_\mu}{m_\mu}\Big(\mathbf{E} + \mathbf{v}_\mu \times \mathbf{B}\Big) - k_D\, n_n \Big(\mathbf{v}_\mu - \mathbf{u}_n\Big)\,.
\end{aligned} \tag{6.3}$$

Here q_μ and m_μ are the charge and mass of a particle of species μ, solar wind protons or cometary ions, respectively. s denotes an appropriate parameter, e.g. time. The collision term is added a-posteriori in Eq. (6.3) to simulate collisions between ions and neutrals. Such collisions can become important close to the nucleus but if they become too strong, then the formalism breaks down. One of the assumptions in the derivation of the Vlasov equation is that there are no direct particle interactions. This term reflects a small correction of the ion dynamics due to collisions. It simulates momentum exchange and it acts as an inner friction term. In the literature this term is often referred to as Langevin term. The parameter k_D is a phenomenological collision rate times volume element. For

Table 6.1: Characteristic values of the solar wind-comet interaction. The hybrid model depends on the interplanetary magnetic field strength B_0 and the background proton density n_0 as input parameters. The characteristic scales of the other quantities are derived from these parameters.

Quantity	Symbol	Numerical Value
Magnetic field strength	B_0	5 nT
Number density	n_0	5 cm^{-3}
Time	$t_0 = 2\pi/\Omega_{g,p}$	2 s
Length	$x_0 = c_0/\omega_{p,p}$	85 km
Velocity	$v_A = x_0/t_0$	48 km s^{-1}
Electric field	$E_0 = v_0 B_0$	0.24 mV/m
Pressure	$p_0 = B_0^2/(2\mu_0)$	0.01 nPa

weak comets the contribution of the collision term is weak. n_n and $\mathbf{u}_n$ are the number density and bulk velocity of the neutrals. If collisions between the particles cannot be treated in this way then a statistical description of the collision processes would be necessary meaning that one has to go back to the Liouville equation and to derive a suitable approximation (Cap 1970).

The Newtonian equation of motion is solved for the solar wind protons and for each cometary ion species. To overcome the problem of defining initial conditions for a large number of ions the macro-particle approach is followed. This is a numerical technique allowing the simulation of large particle collections with the important constrain that the charge-to-mass-ratio of a macro-particle equals that ratio of a real particle (Bagdonat 2005).

6.3 Material theory II - electron dynamics

The electron population is not treated in the macro-particle approach. Estimating the gyroradius r_g defined as

$$r_g = \frac{m\, v_\perp}{|q|\, B} \tag{6.4}$$

for typical solar wind conditions shows that r_{ge} is much smaller than the characteristic scale length of the SW-C interaction. q denotes charge and m the mass of the ion. $v_\perp$ denotes the perpendicular velocity to the magnetic field B. Taking a background magnetic field of 4.9 nT and an averaged velocity of 400 km s^{-1} leads to a $r_{g,e}$ of 0.43 km which is far less than the proton inertial length of 100 km or the gyroradius of protons with 850 km. Therefore, a kinetic description is not mandatory. The electron population is treated as a fluid that ensures charge neutrality on average in each volume element. Under the

assumption of an iostropic pressure the momentum equation reads as

$$\frac{\mathrm{d}(m_e\, n_e\, \mathbf{u}_e)}{\mathrm{d}t} = -e_0\, n_e\Big(\mathbf{E} + \mathbf{u}_e \times \mathbf{B}\Big) - \nabla p_e + R\, \mathbf{j}_e\,. \tag{6.5}$$

$\mathbf{u}_e$ denotes the electron bulk velocity. p_e denotes thermal pressure, R is the resistivity and $\mathbf{j}_e = e_0\, n_e\, \mathbf{u}_e$ the electron charge current density. The resistivity term is neglected in the following discussion as it was not used in the simulations. This term is introduced to effectively account for processes that can not be modeled in the hybrid model such as high frequency wave-particle scattering. As discussed in Bagdonat (2005) it can be used to make the code more stable but generally this term is small compared to numerical diffusion.

To estimate the importance of the time derivative in Eq. (6.5) the variables are scaled and non-dimensionalized. n_e is scaled to the background solar wind ion density n_0. u_e is scaled to the Alfvén velocity $v_A = x_0/t_{g,p}$ with $t_{g,p}$ being the characteristic time scale of the protons defined below and x_0 the proton inertial length given by

$$x_0 = \frac{c_0}{\omega_{p,p}} = v_A\, t_{g,p}\,. \tag{6.6}$$

$\omega_{p,p}$ denotes the proton plasma frequency defined as

$$\omega_{p,p} = \sqrt{\frac{e_0^2\, n_0}{\varepsilon_0\, m_p}}\,. \tag{6.7}$$

ε_0 is the electric vacuum permittivity, e_0 the elementary charge unit, and m_p the proton mass. Time t is scaled to the characteristic time scale $t_{g,p}$ of the proton dynamics in order to judge the importance of the left hand side of Eq. (6.5) from the view point of the ion dynamics. The electric field is scaled to

$$E_0 = v_A\, B_0\,. \tag{6.8}$$

B_0 denotes the interplanetary magnetic field to which also the magnetic field is scaled to. The thermal pressure is measured in units of the background magnetic pressure

$$p_0 = \frac{B_0^2}{2\,\mu_0}\,. \tag{6.9}$$

μ_0 is the magnetic vacuum permittivity. The current density j is scaled according to

$$j_0 = e_0\, n_0\, v_A\,. \tag{6.10}$$

The charge is scaled to the elementary charge e_0. These definitions are summarized in Table 6.1. They allow to map Eq. (6.5) to the following dimensionless equation

$$\frac{t_{g,e}}{t_{g,p}}\frac{\mathrm{d}(n_e^*\, \mathbf{u}_e^*)}{\mathrm{d}t^*} = -2\pi\, n_e^*\Big(\mathbf{E}^* + \mathbf{u}_e^* \times \mathbf{B}^*\Big) - \frac{1}{2}\nabla^* p_e^*\,. \tag{6.11}$$

Here, the characteristic time scale of electrons $t_{g,e}$ and protons $t_{g,p}$ are defined as

$$t_g = \frac{2\,\pi}{\Omega_g}\,. \tag{6.12}$$

The gyrofrequency Ω_g is given by

$$\Omega_g = \frac{q\,B}{m}\,. \tag{6.13}$$

The ratio of the time scale yields

$$\frac{t_{g,e}}{t_{g,p}} = \frac{m_e}{m_p} \approx \frac{1}{2000}\,. \tag{6.14}$$

Hence, the left hand side of Eq. (6.11) can be safely neglected if the time resolution is defined by the characteristic time scale of the protons $t_{g,p}$. The momentum equation of the electron fluid then yields the following equation

$$0 = -e_0\,n_e\Big(\mathbf{E} + \mathbf{u}_e \times \mathbf{B}\Big) - \nabla p_e\,. \tag{6.15}$$

It would be theoretically possible to take the characteristic scales of the electron dynamics. This choice would resolve the electron and the proton dynamics but practically the simulation of the solar wind-comet interaction with such a full particle code would be very hard to realize. Therefore, the model resolves in temporal dimension physical processes determined mainly by the gyrofrequency of the protons. In spatial dimension, processes that are defined on the proton inertial length are resolved. From Eq. (6.15) an explicit equation for the electric field is derived

$$\mathbf{E} = -\mathbf{u}_p \times \mathbf{B} + \frac{\mathbf{j}\times\mathbf{B}}{\mu_0\,\rho_p} - \frac{1}{\rho_p}\nabla p_e\,. \tag{6.16}$$

$\rho_p = e_0\,n_p$ denotes the ion charge density. Here, the fact that the plasma is neutral on average in each volume element is used, e.g. $n_e \approx n_p$. The proton bulk velocity enters Eq. (6.16) by employing charge neutrality and rearranging equation

$$\mathbf{j} = e_0\,n_p\,\mathbf{u}_p - e_0\,n_e\,\mathbf{u}_e \tag{6.17}$$

after $\mathbf{u}_e$. The theoretical description is closed by an adiabatic law for the thermal pressure of the electron population which is intimately related to the energy equation of the electron fluid (Motschmann 2009)

$$p_e = p_{e,0}\left(\frac{n_e}{n_{e,0}}\right)^{\kappa}. \tag{6.18}$$

The expression of the electron pressure is rewritten by applying the assumption of quasi-neutrality and by introducing the plasma beta β which is defined as the ratio between the thermal pressure to the magnetic pressure. Equation (6.18) is then written as

$$p_e = p_0\,\beta_p\left(\frac{n_p}{n_0}\right)^{\kappa}. \tag{6.19}$$

κ denotes the adiabatic exponent.

The formalism developed so far does not only apply to the electrons of solar wind origin but also to the electrons from the cometary plasma. In this case an additional term for the thermal pressure is included in Eq. (6.16) to account for the much colder electron fluid from cometary origin. Second, n_p also includes the ions of cometary origin.

6.4 Electromagnetic field in the hybrid plasma model

So far a material theory has been presented for the dynamics of positively charged ions from solar wind and cometary origin and electrons. These entities are subject to an electromagnetic field and they form currents which themselves generate an electromagnetic field. Thus, to close the theoretical description a model is necessary which describes the time evolution of the electromagnetic field in the presence of a quasi-neutral, perfectly conducting plasma with a frozen-in magnetic field. The model is derived from the electromagnetic field equations of Maxwell.

Charge neutrality on average in each single volume element implies that the macroscopic charge in a volume element is zero. But due to the complex dynamics the distribution of the charge particles inside the volume element can give rise to an electric field, e.g. polarization field. The explicit equation of the electric field in Eq. (6.16) and Gauss law given by

$$\operatorname{div} \mathbf{E} = \frac{1}{\varepsilon_0} \rho \tag{6.20}$$

enable the calculation of such sources of the electric field. There are no sources of the magnetic field

$$\operatorname{div} \mathbf{B} = 0 \,. \tag{6.21}$$

Ampére laws reads as

$$\operatorname{rot} \mathbf{B} = \mu_0 \, \mathbf{j} + \frac{1}{c_0^2} \frac{\partial}{\partial t} \mathbf{E} \,. \tag{6.22}$$

In analogy to Eq. (6.11) all quantities of Eq. (6.22) are scaled yielding the following equation

$$\operatorname{rot}^* \mathbf{B}^* = 2 \pi \, \mathbf{j}^* + \frac{v_A^2}{c_0^2} \frac{\partial}{\partial t^*} \mathbf{E}^* \,. \tag{6.23}$$

As the Alfvén velocity is much smaller than the light of speed, it is safe to neglect the displacement current. This approximation is known as Darwin approximation. Finally, Faraday's law reads as

$$\frac{\partial}{\partial t} \mathbf{B} = -\operatorname{rot} \mathbf{E} \,. \tag{6.24}$$

With Eq. (6.16) for the electric field and Ampére's law without the displacement current Faraday's law is formulated as an equation for the time evolution of the magnetic field

$$\frac{\partial \mathbf{B}}{\partial t} = \operatorname{rot} \left(\mathbf{u}_i \times \mathbf{B} \right) - \operatorname{rot} \left(\frac{\operatorname{rot} \mathbf{B} \times \mathbf{B}}{\mu_0 \, \rho_i} \right). \tag{6.25}$$

Equations (6.3), Eq. (6.16), and Eq. (6.25) are solved numerically until stationarity is reached for a given outgassing strength of the comet and a predefined outgassing pattern. The theoretical framework of the hybrid model as originally developed by Bagdonat and Motschmann (2002) and documented in more detail in the doctoral thesis of Bagdonat (2005) has been presented so far. In the last section of this chapter the numerical implementation of this model shall be briefly outlined.

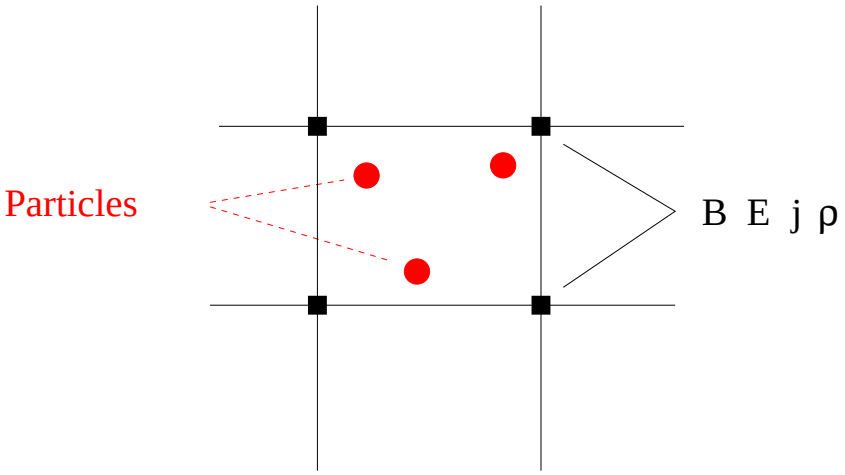

Figure 6.1: The hybrid model solves the electromagnetic field equations on the fixed grid while the (macro-)particles are continuously tracked in the computational domain. The two different formulations are connected by applying the particle-in-cell method to map information between these two spheres. E and B denote the electric and magnetic field while j and ρ the charge current and the charge density, respectively.

6.5 Numerical implementation

The hybrid model consists of the equation for the magnetic field, the adiabatic law for the pressure, of the electric field, and the characteristics of the Vlasov equation given in Eq. (6.25), Eq. (6.19), Eq. (6.16), and Eq. (6.3), respectively. The description of the electromagnetic field is Eulerian while the ion dynamics is formulated in Lagrangian coordinates. These two different formulations are connected by applying the particle-in-cell (PIC) method. A stationary Eulerian mesh is generated on which the field quantities of the hybrid model such as the electromagnetic fields, the charge densities of positively charged ions, and their currents are defined as depicted in Fig. 6.1. The characteristics of the Vlasov equation are tracked continuously in phase space. The two different formulations are connected by applying special techniques, e.g. interpolation, to map information from one formulation to the other. The interaction between the (macro-)particles occurs only through the averaged electromagnetic field. Therefore, the hybrid plasma model is a particle-mesh model.

The electromagnetic field equations require the charge and current densities at the grid nodes. These quantities are calculated from the position and the velocity of the ions by applying the PIC weighting method of Birdsall and Fuss (1969). This weighting method determines the contribution of an ion to the moments at a grid node which depends on the position of the particle relative to the nodes. Bagdonat (2005) describes the method for a Cartesian simulation grid. For the solution of the Newtonian equations of motion in Eq. (6.3) the electromagnetic field at the individual position of the ions is required. The same weighting method as for the calculation of the moments is applied to obtained the

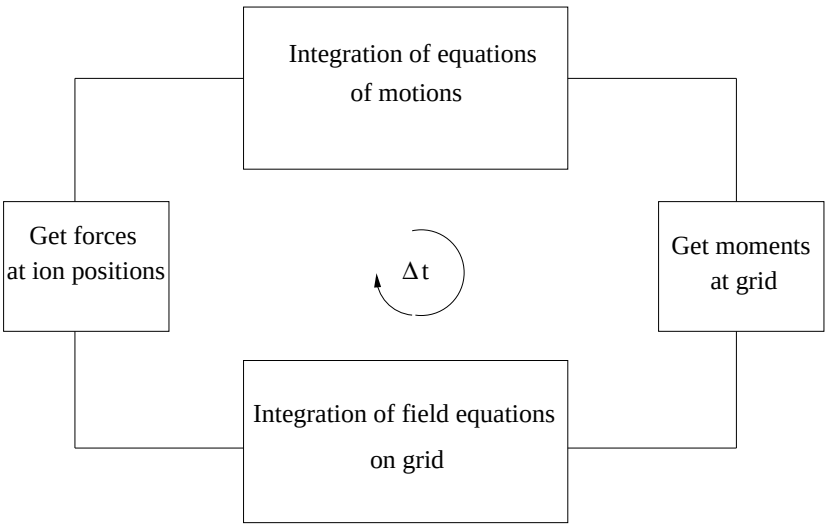

Figure 6.2: A computational cycle of the hybrid model. In a time step Δt the equations of motion of the (macro-)particles are solved for a given electromagnetic field configuration. Through a cloud-in-cell weighting method the moments of the distribution function are calculated at the grid nodes. In the third step, the electromagnetic field equations are solved. Finally, the same cloud-in-cell weighting method is employed to calculate the electromagnetic field at the particle positions.

electromagnetic field at the particle positions. As pointed out by Birdsall and Langdon (1985) the stability of the method requires to use the same weighting method for the fields as for the moments.

The working mechanism of the hybrid code follows the scheme of Birdsall and Langdon (1985). First, the equations of motion are integrated and the particles are moved. Through weighting the moments of the distribution function are calculated. Then the electromagnetic field is integrated on the grid. Finally, through weighting the electromagnetic force is derived from the electromagnetic field solution at the position of the ion particles. The computation scheme is displayed in Fig. 6.2.

The time integration uses the algorithm of Matthews (1994) and the method of Eastwood et al. (1995) for the spatial derivation in curvilinear coordinates. More details on the employed techniques can be found in Bagdonat and Motschmann (2002) and Bagdonat (2005).

7 Solar wind-comet interaction with coma anisotropies

7.1 Introduction

The outgassing strength of a comet is an important parameter for the study of the SW-C interaction as it determines the size and nature of the interaction region. Key effects such as the pick-up process depend heavily on the outgassing strength and the spatial distribution of neutral atmospheric particles before being ionized and then dominated by the interaction with the solar wind plasma.

From remote sensing it is not possible to resolve in detail the actual distribution of the outflowing gas around the nucleus. Only column densities can be inferred but observational data allow to identify anisotropy in the coma of many comets. In addition, in-situ observations have shown that the outgassing behavior of the nucleus is not spherically symmetric. Keller et al. (1986a) reported that only a minor fraction of the surface of comet 1P/Halley was active. A sunward-tailward anisotropy in H_2O outgassing has been detected for a wide range of comets such as 2P/Encke, Hale-Bopp, 1P/Halley, 9P/Tempel 1, 19P/Borrelly. More precisely, comet 2P/Encke is well known for its asymmetric coma morphology (Feldman et al. 1984, Festou and Barale 2000). The Deep Space 1 (DS1) mission to comet 19P/Borrelly revealed a significant offset of plasma boundaries to the north of the Sun-comet line which has been attributed to a strong asymmetry in the neutral gas coma by Young et al. (2004). The DS1 MICAS camera has revealed a well collimated large sunward side jet, possibly responsible for the anisotropic coma morphology. More recently, in conjunction with NASA's Deep Impact (DI) mission to comet 9P/Tempel 1, Feaga et al. (2007) reported a sunward/anti-sunward asymmetry in H_2O gas around the nucleus. Even in case of Rosetta's target comet CG, albeit so far not so intensively investigated, Lamy et al. (2007) and Schulz et al. (2004) reported about an anisotropic coma morphology.

Thermophysical modeling also shows that during the night the amount of sublimated water vapor decreases by several orders as the warm nucleus cannot provide enough energy to retain activity as during the day. This is displayed in Fig. 3.11 for water sublimation at the surface.

Numerical simulations of the outflowing gas in the coma also show a persistent anisotropy of the inner coma. Combi (1996) reported about numerical studies of a pure-gas subsolar jet for a moderate active comet ($\approx 3 \times 10^{28} s^{-1}$) that revealed a particle flow to be concentrated on the sunward side, although 15% of the particle flow crosses the terminator. During the same period Xie and Mumma (1996) published numerical studies

about H_2O gas flow for 1P/Halley that showed a radial outflow of gas with only small lateral velocities. Although, these investigations have been performed for strong comets, it is conceivable that inhomogeneous and localized surface activity of weak comets leads to an anisotropic coma morphology.

Only recently two investigators have addressed this issue in conjunction with the DS1 mission to 19P/Borrelly. Delamere (2006) reported about studies with a semi-hybrid code, only the cometary ions are treated kinetically while the solar wind protons are treated as a fluid. In this paper large gyroradius effects of cometary ions on the plasma environment are studied by variation of the interplanetary magnetic field strength. The deployed mass-loading pattern was essentially isotropic. Hence, neglecting the findings of Young et al. (2004) which indicate an anisotropic coma at the time of the DS1 encounter. More recently Jia et al. (2008) reported about a series of MHD studies for 19P/Borrelly with an anisotropic plasma source. These investigators aim to reproduce the observed offset of the mass-loading peak and the velocity minimum measured by DS1. They assume different anisotropic mass-loading pattern for their global MHD model. The authors conclude that anisotropy cannot be solely responsible for the observed offsets. They pointed out that kinetic effects, such as finite gyroradius could provide a possible mechanism to interpret the DS1 measurements. It can be concluded that while Delamere (2006) is partly able to resolve finite gyroradius effects, the solar wind protons are treated as a fluid, the model of Jia et al. (2008) is not able to do so. But the latter authors have studied anisotropy with their global MHD model systematically.

In this chapter these approaches are extended in the sense that different anisotropic plasma sources are studied with a hybrid model which is able to fully resolve finite gyroradius effects as it treats both solar wind and cometary ions kinetically. The model regards idealized and simplified configurations of real comets. Input parameters and boundary conditions are used as anticipated for comet CG during the Rosetta mission. Two shape models for the cometary plasma source were inferred from a gas dynamic model. The so called dayside model (hereafter 2π) simulates cometary activity solely on the Sun-faced side of the nucleus. The cone shaped (hereafter $c\pi$) model confines cometary activity in a cone with opening angle of 0.5π. For comparison the classical spherically symmetric coma model is also calculated. The diurnal rotation of the comet is not taken into account. Comparing the real time of a simulation with the diurnal rotation time τ_r of CG justifies to neglect the diurnal rotation of the nucleus. The real simulation time is in the range of minutes while the diurnal rotation is in the range of hours. In addition, the rotation axis of comets are not so well known (Lamy et al. 2007).

In order to address two different states of nucleus activity the calculations were done for two heliocentric distances. At 1.30 AU cometary activity is so pronounced that strong mass-loading effects on the solar wind flow can be expected while at 3.25 AU the nucleus is so faint that the feedback to the solar wind is weak. This chapter is based on the publication of Gortsas et al. (2009).

7.2 Coma shape models

In many models of cometary plasma the coma is assumed to be a spherically symmetric point source with a uniformly outflowing gas that is destroyed based on an exponential

lifetime (Combi et al. 2004). For a nucleus with outgassing strength Q the number density of neutrals $n_{n,4\pi}$ that expand radially with a velocity of u_n reads as

$$n_{n,4\pi}(r) = \frac{Q}{4\pi\, u_n\, r^2}\, e^{-\frac{r\nu}{u_n}}\,. \tag{7.1}$$

r denotes the cometocentric distance from the nucleus and ν the ionization rate. This coma model is also the starting point for the Haser model (Haser 1957) which has been used by various investigators to derive production rates from measured column densities (Ahearn 1982, Cochran 1985, Rauer et al. 2003).

This model has been used almost exclusively in many investigations of the SW-C interaction. In analytical models published by Biermann et al. (1967) and Mendis and Flammer (1984) this model was successfully used to provide basic but still very important insights into the structure and the magnitude of the effects to be expected. MHD and multi-fluid models also employed this coma model to study the global structure of the plasma environment of strongly outgassing comets (Wegmann et al. 1987, Bogdanov et al. 1996, Gombosi et al. 1996, Benna and Mahaffy 2006, Hansen et al. 2007). Also in previous hybrid simulations of comets this model was successfully used to describe the plasma environment of comets (Lipatov et al. 2002, Bagdonat and Motschmann 2002, Motschmann and Kührt 2006). The spherically symmetric shape model of this paper is defined by Eq. (7.1) and referred to as 4π case.

For weak comets a free-flow model of the coma is applicable, as the hydrodynamic region, if at all, is confined close to the vicinity of the nucleus (Combi and Smyth 1988). Therefore, the assumption of a neutral gas stream expanding in straight lines with a constant outflow velocity seems to be a good approximation. In addition, Combi (1996) reported about a series of calculations with a Direct Simulation Monte Carlo code which suggested that for moderately active comets (6×10^{28} s^{-1}) the heating of the coma remains small so that the assumption of a constant outflow velocity seems to be justified. Throughout this paper a constant outflow velocity $\mathbf{u}_n$ of 1 km s^{-1} is employed in good agreement with the cited calculations. Another model assumption is to neglect any gravitational attraction which is justified given the assumed high porosity of comet nuclei (Keller et al. 1986a).

Two model geometries are derived from this model to account for an anisotropic coma morphology. The models are displayed in Fig. 7.1. Cometary activity is geometrically confined in such a way that the integrated surface activity, i.e. the total gas production rate Q, remains constant. On the one hand, this approach is necessary in order to simulate the same number of ions mass-loading the solar wind flow for different initial particle distributions. On the other hand, observers derive, in most cases with a Haser model, integrated outgassing rates from measurements. Since the spatial resolution is limited, it is not possible to localize the gas distribution around the nucleus, so that the information of how the gas is distributed around the nucleus is missing. Therefore, it is reasonable to model in all investigated cases an equally active comet for three different geometrical limits.

The neutral gas density for the case with nucleus activity being solely concentrated on the Sun-facing side reads as

$$n_{n,2\pi}(r,\phi,\theta) = \alpha_{2\pi}\, n_{n,4\pi}(r)\, 1_{[0,\pi/2)}(\theta)\,. \tag{7.2}$$

where ϕ is the azimuthal angle in the cometocentric coordinate system in which the polar axis points in the -x direction. θ is the polar angle. This model is referred to as 2π calculation. The above introduced function $1_{[0,\pi)}(\theta)$ is the indicator function defined as

$$1_{[0,\pi)}(\theta) \quad = \begin{cases} 1 & \text{for} \quad \theta \in [0,\pi) \\ 0 & \text{else}\,. \end{cases} \tag{7.3}$$

The coefficient $\alpha_{2\pi}$ is derived from the constrain that the integrated surface activity of the 2π case equals the 4π case. Its numerical value is

$$\alpha_{2\pi} = 2\,. \tag{7.4}$$

For the cone model the polar angle θ is restricted according to

$$n_{n,c\pi}(r,\phi,\theta) = \alpha_{c\pi}\, n_{n,4\pi}(r)\, 1_{[0,\pi/4)}(\theta)\,. \tag{7.5}$$

This model is referred to as $c\pi$ model, with c as an acronym to cone. The calculation of $\alpha_{c\pi}$ relies in analogy to the 2π case on the constrain that the integrated surface activity remains in the $c\pi$ case equal to the 4π case. Its numerical value is

$$\alpha_{c\pi} = \frac{2}{1-\frac{1}{2}\sqrt{2}} \approx 6.8\,. \tag{7.6}$$

Spatial confinement thus leads to an enhancement of the neutral gas density to ascertain an equally active comet.

In Fig. 7.1 a snapshot of the gas cloud through the polar plane of the coordinate system is displayed for the three cases. At each time step the code produces pick-up currents mass-loading the solar wind according to these three shape models. As in the spherically symmetric limit a neutral gas expansion with constant outflow velocity on straight lines is also assumed for the 2π and $c\pi$ cases. An ion production rate is inferred from the neutral gas density according to

$$\frac{\partial n_i(r,\phi,\theta)}{\partial t} = \nu\, n_n(r,\phi,\theta)\,. \tag{7.7}$$

How realistic are these models? Schulz et al. (2004) published broad-band R images of CG showing distinct features in the coma of this comet as the comet moves from the Sun away between February and June 2003. Schulz et al. (2004) draw a link between the jet like features seen in these images with those of 1P/Halley. The spatial extensions of the jets appear to be in the order of 1000 to 5000 km. The $c\pi$ model shown in Fig. 7.1 is in good agreement with these values. The *high* density region is confined to around 5000 km from the nucleus.

7.3 Implementation

In a hybrid code analytical relations describing the activity of comets need to be mapped to discrete particle distributions. The algorithm must simulate the physical processes of Eq. (7.1) and Eq. (7.7) as well as for the anisotropic cases. In the spherically symmetric

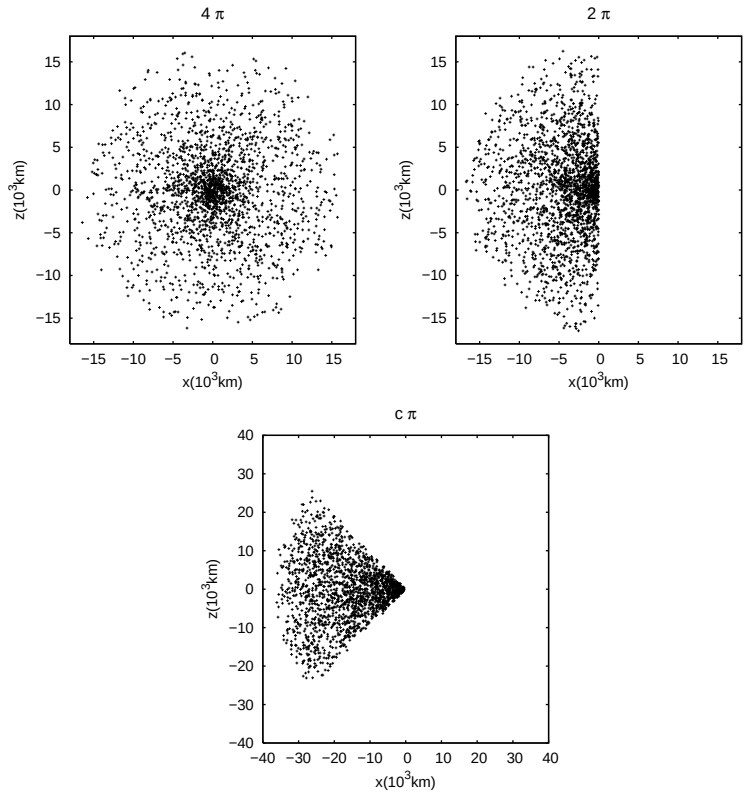

Figure 7.1: Snapshot of the comet outgassing patterns for the three investigated cases at a heliocentric distance of 1.30 AU. At each time step the hybrid code generates particles according to these patterns in 3 dimensions. The solar wind enters the box from the left side in +x direction. Upper left the spherically symmetric case, upper right the day side restricted and lower middle the cone shaped model are displayed. The polar plane of the coordinate system defined in Fig. 7.2 is shown. The concentration of particles on the sun illuminated side is clearly visible. Notice the larger scale in the cone shaped model. Figures from Gortsas et al. (2009).

case the azimuthal angle ϕ and the polar angle θ are uniformly distributed in the interval $[0, 2\pi) \times [0, \pi)$. In radial direction the neutral density follows a r^{-2} dependence from the nucleus. The spherically symmetric case has been implemented by Bagdonat (2005). The approach is based on the Linux implementation of the random algorithm in /dev/random which returns pseudo-random numbers in the range 0 to RAND_MAX. The latter variable is the upper bound of the random numbers the system can calculate. The return value of this function divided by RAND_MAX and multiplied with the length of the interval of the variables ϕ and θ provides the uniformly distributed spherical angles.

r^{-2} dependence is simulated by applying a known theorem from probability theory to generate random variables X with certain predefined distribution functions F_X from in the interval $[0, 1]$ uniformly distributed random variables Z. A series of random variables x_i with distribution function F is then obtained from a series of in $[0, 1]$ uniformly distributed random variables z_i by applying the following algorithm (Friedrich and Pietschmann

Table 7.1: Input parameter of the hybrid model for the study of coma anisotropy.

Parameter	Symbol	Study I	Study II
Heliocentric distance	r_H	1.3 AU	3.25 AU
Interplanetary magnetic field	B_0	4.9 nT	1.6 nT
SW background density	n_0	6 cm^{-3}	0.9 cm^{-3}
SW bulk velocity	u_{sw}	430 km s^{-1}	360 km s^{-1}
Expansion veloc. of com. neutrals	u_n	1 km s^{-1}	1 km s^{-1}
Outgassing strength	Q	5×10^{27} s^{-1}	1×10^{24} s^{-1}
SW plasma beta	$\beta_{e,sw}$	0.5	0.5
Cometary plasma beta	$\beta_{e,c}$	0.04	0.04
Ionisation rate	ν	10^{-6} s^{-1}	10^{-6} s^{-1}
Number of grid points		90×90×90	90×90×90

2010)

$$x_i = \sup\{\, x : F_X(x) \leq z_i \,\} \qquad (i = 1, 2, ...)\,. \tag{7.8}$$

This approach was also employed to calculate the r^{-2} dependence of the anisotropic cases. To optimize the calculation the polar axis of the coordinate system is tilted by 0.5π pointing towards the Sun. In this coordinate system the azimuthal angle remains uniformly distributed while the polar angle is restricted in the interval $[0, \pi/2)$ and $[0, \pi/4)$ for the 2π and $c\pi$ case, respectively.

7.4 Simulation set-up

In this section details of the calculation should be provided. The cometary ions are expanding radially from the nucleus according to the activity pattern presented in the previous section. Their initial velocity is 1 km s^{-1}. The ion-drag collisions are simulated according to Eq. (6.3) with a k_D constant of 1.7×10^{-9} cm^3 s^{-1} in accordance with Israelevich et al. (1999) which had used this value for comet 1P/Halley. The ionization rate ν depends on the state of the Sun. At 1 AU ν is approximately $\approx 10^{-5} - 10^{-7}$ s^{-1} as reported by Huebner et al. (1992). To keep the number of free parameters between the two heliocentric distances low a value of $\approx 10^{-6}$ s^{-1} was employed at 1.3 AU and 3.25 AU.

The plasma betas in Eq. (6.19) for the electron pressure differs for electrons of solar wind or cometary origin. The solar wind plasma is assumed to be a hot fully ionized plasma. Therefore, the solar wind plasma beta $\beta_{e,sw}$ has a value of 0.5. The cometary electron beta is an order of magnitude lower as the cometary plasma is much colder. A value of 0.04 was used for $\beta_{e,c}$. The adiabatic coefficient κ in Eq. (6.19) has a value of 2 to describe the confinement of electron dynamics in the orthogonal plane of the magnetic field.

In Fig. 7.2 the geometry of the 3-D simulation box is displayed. The solar wind enters the domain from the -x direction with a constant bulk velocity $\mathbf{u}_{sw}$. Upstream

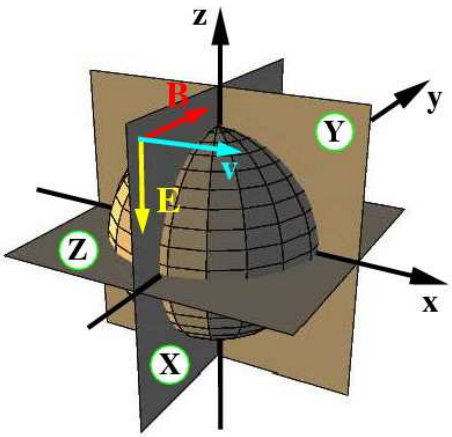

Figure 7.2: Coordinate system of the three dimensional simulation. The electric field **E**, the magnetic field **B**, and the solar wind velocity **v** correspond to the undisturbed solar wind conditions. In section 7.5 contour plots through the $y = 0$ (polar) are discussed.

inflow boundary conditions are enforced. The inserted particles enter the simulation box according to the undisturbed background conditions with a thermal velocity distribution characterized by a width of 25 km s^{-1}. Such kind of boundary conditions are applicable as the solar wind flow is supersonic, so that no information from the solar wind-comet interaction travels upstream. Upstream refers to the direction from which the plasma is flowing while downstream refers to the direction in which the undisturbed solar wind is flowing. Downstream outflow boundary conditions are used. All particles leaving the simulation box are deleted. On the remainder planes inflow boundary conditions are enforced. An equidistant Cartesian grid with a mesh of 90 nodes in each spatial direction is used. While this resolution enables us to resolve the inertial length at 3.25 AU, this is no longer true at 1.3 AU. This trade-off is necessary since currently CPU time and memory constraints on current workstations restrict the number of mesh points in each spatial direction to around 100. At the beginning the comet is switched on by producing a certain amount of particles according to the discussed shapes (see Fig. 7.1). Stationarity is reached after the solar wind passes several times through the simulation box typically up to five times. The physical parameters of the solar wind plasma have been chosen in accordance to the expected conditions of CG at two different heliocentric distances 3.25 AU (Rosetta instruments on) and 1.30 AU (perihelion) which is in agreement with Hansen et al. (2007). For all three scenarios, e.g. 4π, 2π, and $c\pi$, the same values are employed and summarized in Table 7.1.

7.5 Results

The traditional way of presenting 3 dimensional simulation results are 2 dimensional contour plots along cutting planes. This presentation format will be used in this thesis as well but the discussion shall start with a 3 dimensional illustration of the magnetic field at 1.30 AU shown in Fig. 7.3. The presentation continues then with the polar plane of the dif-

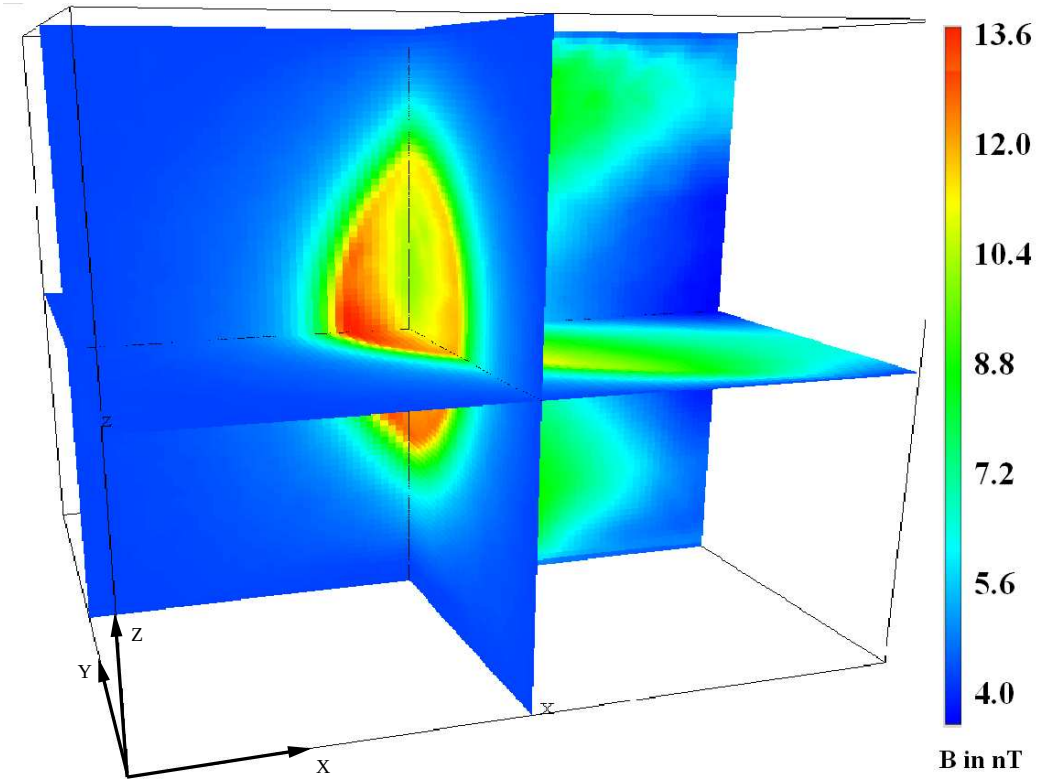

Figure 7.3: The magnetic field in nT for the three dimensional calculation at 1.30 AU for the 4π case. The solar wind enters the box from the left side in +x direction. The predominant transport of the magnetic field in -z direction is clearly visible. Furthermore, a region can be discerned which is depleted in the magnetic field behind the +z-axis. This indicates a low degree of mixing between the solar wind and cometary ion species. The magnetic field remains bound to the solar wind flow leading to the pileup in front of the obstacle. Figure from Gortsas et al. (2009).

ferent anisotropic mass loading patterns shown in Fig. 7.4, Fig. 7.5, and Fig. 7.6. The discussion is complemented by 1 dimensional plots along the x-axis shown in Fig. 7.7 which help to enlighten further the involved interaction. Finally, the results at 3.25 AU are presented in Fig. 7.8 and in Fig. 7.9.

In Fig. 7.3 an illustration of a fully 3 dimensional computation for the magnetic field along the orthogonal planes of the coordinate axes is displayed. This calculation has been done for the spherically symmetric case at 1.30 AU. Three distinct regions can be discerned in Fig. 7.3. The region in front of the obstacle is characterized by the undisturbed interplanetary magnetic field. Closer to the nucleus the magnetic field is shocked leading to the formation of a bow shock (BS) which is accompanied by the magnetic barrier region (MBR) as a parabolic structure from the +z to the -z hemisphere. Behind this structure on the downstream side a region with reduced values in magnetic field strength can be discerned. The formation of such a depletion zone is also visible along the terminator and the polar planes of Fig. 7.3. In regions of an undisturbed solar wind the magnetic field is transported through convection. However, as the solar wind

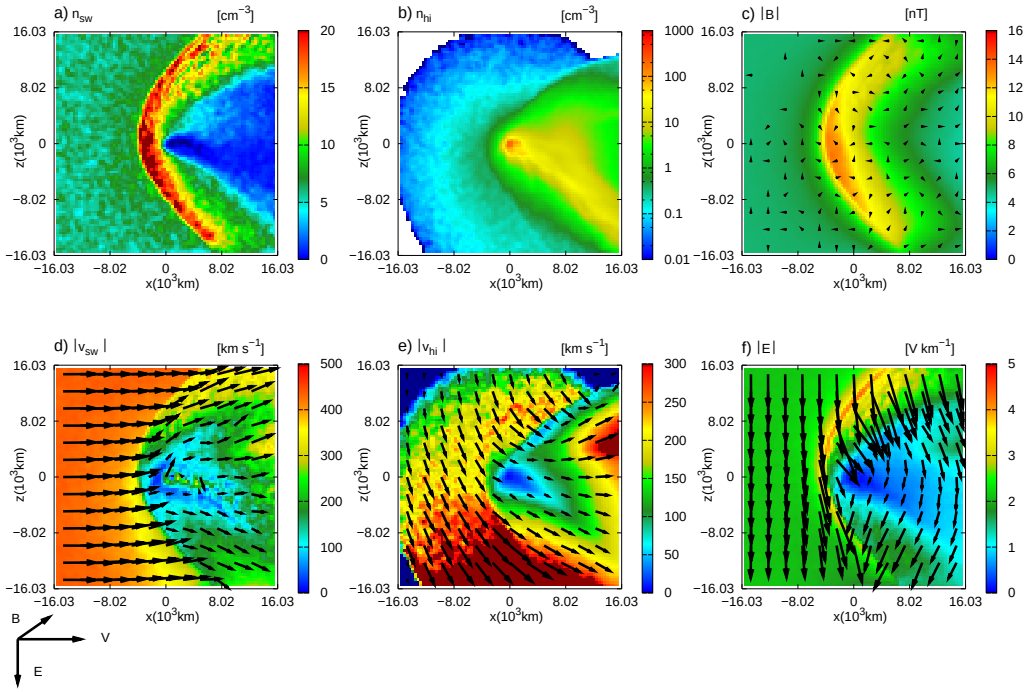

Figure 7.4: The SW-C interaction in the polar plane is displayed for the 4π case at 1.3 AU. From upper left to lower right is shown the solar wind proton density, the cometary ion density, the absolute value of the magnetic field, the solar wind bulk velocity, the cometary ion bulk velocity, and the absolute value of the electric field. Cometary activity leads to the formation of a bow shock shown in a) separating the solar wind plasma from the cold cometary plasma. The deceleration of the solar wind leads to a pileup of the magnetic field in front of the inner coma and to the formation of the magnetic barrier region in c). Figures from Gortsas et al. (2009).

approaches the nucleus, cometary ion density goes up. In this case mass loading of the solar wind leads to deceleration of the solar wind ions, while the solar wind electron fluid faces an outward directed cometary electron pressure. Hence, the mixing region of the solar wind species with the cometary species is rather small. Therefore, the magnetic field remains bound to the motion of the solar wind species rather than being passed to the cometary species. This leads to the formation of the MBR with the magnetic field draped around the obstacle.

7.5.1 4π run at 1.30 AU

The spherically symmetric case is commonly used as a model for the neutral gas source in investigations of the plasma environment of comets. The simulation results for the polar plane are shown in Fig. 7.4. In all contour plots the color scale denotes the strength of the fields while the drawn arrows represent the projection of the respective vector fields on the cutting plane. As already pointed out for the magnetic field in the 3-D plot of Fig. 7.3

three regions of different behavior can be discerned in the solar wind density, solar wind bulk velocity, the electric, and the magnetic fields. The homogeneous background region dominates the upstream side. In the middle of the simulation box a parabolically shaped structure which marks depending on the considered field a transition region with enhanced or decreased magnitudes are clearly visible. The downstream side is characterized by a decrease in magnitude. An obvious reason for these common structures is the fact that they are all derived from an equilibrium supersonic background flow. In contrast to that cometary plasma acts as a pollutant, mass loading the solar wind flow. Consequently, cometary properties like density distribution or bulk velocity reveal a different behavior as is visible in Fig. 7.4b and e.

At a heliocentric distance of 1.30 AU cometary activity of CG is so pronounced that it is in the regime of a fully developed shock as discussed by Lipatov et al. (2002), Bagdonat and Motschmann (2002), and Hansen et al. (2007) for hybrid plasma simulations of weak comets. The BS is at around 4.0×10^3 km along the x-axis from the nucleus. It is accompanied by the proton pileup region which exhibits various substructures. These kind of structures have been referred to as shocklets or turbulent structures by Omidi and Winske (1990) and they have been observed not only for comets but also for Mars by Bösswetter et al. (2004) and magnetized asteroids by Simon et al. (2006). The characteristic scale of the shocklets can be derived from the width of the cycloidal motion. A mean velocity of 400 km s^{-1} and a magnetic field of 9 nT lead to proton gyroradii of 460 km which in turn leads to a width of the cycloidal motion of $2\pi\, r_g \approx 3000$ km (Bösswetter et al. 2004). This value is in good agreement with the width of the BS of about 3500 km along the x-axis. The existence of the BS was predicted prior to any encounter with comets together with the contact surface as plasma boundaries of comets by Schmidt and Wegmann (1982) and Ip and Axford (1982). As Coates and Jones (2009) reports it is common agreement in the community that the signatures seen in the data received from encounters with comets were actually those of a BS.

Another pronounced feature of the BS is its asymmetric structuring along the z-axis, especially visible in Fig. 7.4a. In the +z hemisphere the density seems to consist several rays while in the -z hemisphere it reaches higher values. Due to the deceleration of solar wind ions and their subsequent thermalization the individual ion velocity deviates from the background flow. Hence, more solar wind protons are picked-up by the convective electric field which leads to the observed predominant particle transport in -z direction. An important boundary clearly developed in the solar wind density is the ion composition boundary (ICB). This boundary prevents the mixing of the solar wind plasma with the relatively cold cometary ion plasma. A comparison of Fig. 7.4a and b shows that in regions of high cometary ion density the solar wind density is reduced and vice versa. The physical mechanism of this boundary has been investigated for Mars and Titan by Simon et al. (2007). The authors identified a combination of electron pressure and the convective electric field to be responsible for the formation of this boundary.

From Fig. 7.4b it can be inferred that cometary ions are mainly confined in the tail region. Their motion is predominantly oriented 45° from the undisturbed solar wind flow in -z direction. The heavy cometary ions have large gyroradii causing a motion with large cycloidal arcs. The cometary ion tail shown in the -z region of the simulation box is just the first section of this cycloidal arc. With an average velocity of about 300 km s^{-1} and a magnetic field of 5 nT the gyroradius of cometary ions is about 10^4 km. This

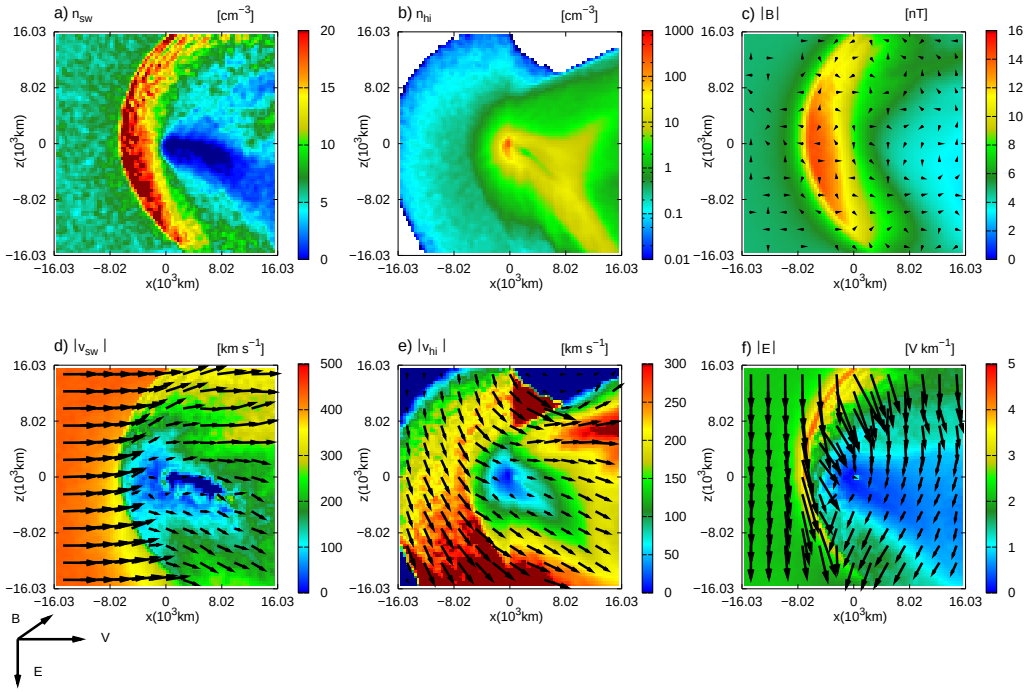

Figure 7.5: The SW-C interaction in the polar plane is displayed for the 2π case similar to Fig. 7.4. Spatial confinement leads in this case to quantitatively differences. The plasma structures are enhanced and pushed towards the Sun. Figures from Gortsas et al. (2009).

value is compared with that part of the tail lying in the simulation box which is of about 1.6×10^4 km. The observed cycloidal tail structure correlates very well with the non-vanishing magnetic field downstream of the magnetic barrier region seen in Fig. 7.4c. This magnetic field is responsible for the gyromotion of the cometary ions visible in Fig. 7.4b. The magnetic field in Fig. 7.4c shows a similar behavior as the solar wind density. Both quantities reach their maximum values along the x-axis at the same position as shown in Fig. 7.7a and d. This indicates the excitation of a fast magnetosonic mode. The MBR is clearly developed and exhibits a spatial width along the x-axis which is larger than the pileup region of the solar wind density. This indicates an increasing degree of mixing between the electron species of solar wind and cometary origin.

7.5.2 2π run at 1.30 AU

In complete analogy to the 4π case three pronounced regions in the plots of the electromagnetic fields and solar wind quantities can be discerned. As the processes involved are in principle the same for the two cases the focus will be in working out the differences. The main goal is to understand what kind of effects geometric confinement of cometary activity has on the plasma environment of comets.

Comparing the day side restricted case in Fig. 7.5 with the spherically symmetric case in Fig. 7.4 unveils qualitative similarities in all quantities. The differences are mostly

quantitative in nature. Day side activity causes a stronger shift of the bow shock towards the Sun. While in the 4π run the bow shock sets in at 4.0×10^3 km, this structure is encountered in the 2π case at a cometocentric position of 6.7×10^3 km. The ratio of the bow shock distances yields

$$\frac{R_b(2\pi)}{R_b(4\pi)} \approx 1.64\,. \tag{7.9}$$

It seems to be correlated to the increase of the neutral gas population by a factor of 2 according to Eq. (7.2). Similarly, the width of the bow shock along the x-axis exhibits a ratio of 1.58. The substructuring of the proton pileup region is here also developed. From Fig. 7.7a, b and d we can infer that the jump in solar wind proton density and in the magnetic field strength along the x-axis remains comparable to the 4π run.

The Mach cone of the fast magnetosonic mode exhibits a larger opening angle than in the 4π case. With a magnetosonic velocity of 300 km s^{-1} and of 330 km s^{-1} in case of the 4π and 2π runs deduced from Fig. 7.4d and Fig. 7.5d an angle between the undisturbed solar wind flow and the fast magnetosonic mode of about 44° and 49° is obtained, respectively. These values are in good agreement with Fig. 7.4a and Fig. 7.5a. The fact that the solar wind density and the magnetic field in Fig. 7.5a and c exhibit the same behavior clearly indicates the excitation of a fast magnetosonic mode as was the case for the 4π run. Hence, the form of the magnetic barrier region in Fig. 7.4c and Fig. 7.5c supports the conclusion of an increased fast magnetosonic wave propagation as a result of the spatial confinement of cometary activity.

The overall picture of a perceived stronger comet is also confirmed by the solar wind velocity plots in Fig. 7.4d and Fig. 7.5d for the 4π and 2π cases, respectively. As cometary activity is solely confined to the Sun illuminated side of the nucleus mass-loading of the solar wind sets in on a greater distance from the nucleus compared to the 4π run. However, as Fig. 7.7e shows the situations remains comparable.

The orientation of the cometary ion tail in Fig. 7.5b is slightly twisted away from the anti-sunward direction. This indicates an increase of the gyroradius of cometary ions. Taking the magnetic field plot of Fig. 7.5c into consideration a stronger decrease of the magnetic field is met in the downstream side which reduces the cycloidal motion of the cometary ions seen in Fig. 7.5b. With a magnetic field strength of about 3 nT and an average velocity of about 300 km s^{-1} a gyroradius of the cometary ions of 1.6×10^3 km is obtained. The gyroradius has to be compared to the gyroradius of the 4π run, which is $\approx 10^3$ km and to the extension of the tail lying in the simulation box of about 1.5×10^3 km. As only the beginning of the cycloidal motion is shown in Fig. 7.5b the predominant transport direction of the cometary ions seems to be twisted away from the Sun-comet line. Another visible difference to the 4π case is due to the deployed outgassing pattern. The dayside activity leads to a higher density on the Sun illuminated side.

The comparison between the 2π and 4π cases reveals quantitative differences while qualitatively both cases agree well. Therefore, by assuming a spherically symmetric outgassing comet and by assigning the observed total outgassing rate Q also to the nightside of the nucleus one ends up considering a weaker comet. Bagdonat (2005) reported about a similar behavior for a different scenario. By considering a weak comet with the same hybrid code and a spherically symmetric profile, the 4π case of this paper, this investigator observed a similar blow up of the plasma structures by increasing the electron temperature by a factor of 10. Bösswetter et al. (2004) confirmed the effect of the electron temperature

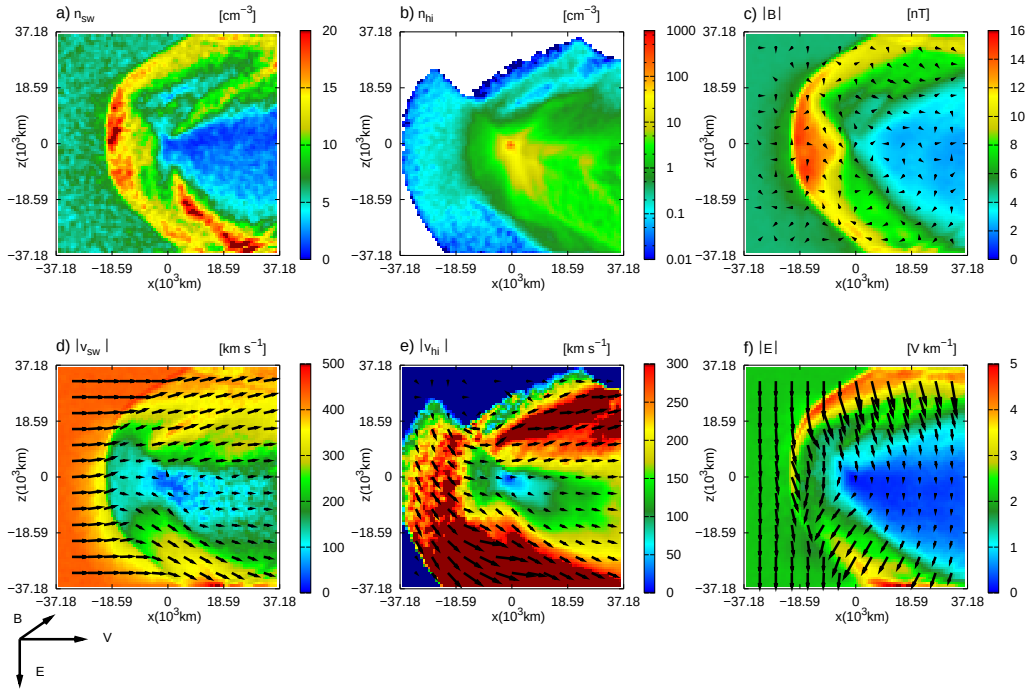

Figure 7.6: The SW-C interaction in the polar plane is displayed for the $c\pi$ case similar to Fig. 7.4. The cone shape model leads to qualitatively new features. First, the mixing region of solar wind and cometary species is increased which in turn opens an additional transport channel for the magnetic field from the MBR away. Hence, the magnetic barrier region is broader. Second, this strong mixing leads to a gradually developed ion composition boundary. Finally, the deceleration of the solar wind is much smoother than in the 2π and 4π cases. Figures from Gortsas et al. (2009).

in case of hybrid plasma simulations of Mars. In this investigation the electron temperature or the cometary plasma beta is left constant for all considered cases.

To conclude in case of small deviations from the spherically symmetric outgassing pattern the observed plasma structures show quantitative modifications but qualitatively the overall picture remains the same. The spatial activity pattern of the nucleus can quantitatively modify the location and shape of the plasma boundaries encountered at a comet and has to be considered among other parameters, such as the electron temperature, in order to fit plasma simulations to observational data.

7.5.3 $c\pi$ run at 1.30 AU

The outgassing pattern in the cone shape model deviates stronger from the spherically symmetric case than the 2π run. Consequently, the observed plasma structures show not only quantitative but also qualitative modifications. An obvious effect of the cone shaped model is the substantial increase of the interaction region. The simulation box has an extension of about 7.4 $\times 10^3$ km twice as large as in the other two cases. The bow shock

is 18.8×10^3 km from the nucleus as shown in Fig. 7.6a. Compared to the 4π case this yields a factor of

$$\frac{R_b(c\pi)}{R_b(4\pi)} \approx 4.5\,, \tag{7.10}$$

which is to some degree comparable to the increase in cometary activity introduced in Eq. (7.5). The spatial extension of the bow shock is about 13.7×10^3 km along the x-axis which is almost 4 times larger than in the 4π case. The shape of the bow shock correlates to the cone shaped outgassing pattern. It is instructive to take another look at Fig. 7.1. Similar to the previous two cases the already discussed substructuring of the proton pileup region is discernible. The cometary ion tail is to a larger part visible because of the substantially increased simulation box. The gyroradius of cometary ions is about 13.0×10^3 km for a magnetic field of 3 nT, as deduced from Fig. 7.6c, and an average velocity of 300 km s^{-1}. Hence, some complete cycloidal arcs are included in the simulation box.

So far the obtained picture of the plasma environment seems to fit the conclusion drawn in the previous section that spatial confinement of cometary activity leads to a perceived stronger comet causing a blow up of the plasma structures. However, a more refined analysis unveils important differences. In Fig. 7.7a, b, and c are shown the solar wind and cometary ion density for the three investigated cases. These figures show that the mixing region between the two species increases due to spatial confinement. Moreover, the cone shaped model leads to a substantial broadening of the MBR as shown in Fig. 7.7d. This observation is also confirmed by comparing the contour plots along the polar plane displayed in Fig. 7.4c, in Fig. 7.5c, and in Fig. 7.6c respectively. Finally, Fig. 7.7e shows that in the cπ case deceleration of the solar wind is much smoother than in the other cases. Hence, the main result of this investigation is that while the solar wind density, shown in Fig. 7.6a, exhibits similar structures like in the previous two cases, the magnetic field, shown in Fig. 7.6c, undergoes a different evolution. In addition, the ion composition boundary seems to be only gradually developed in contrast to the other cases as inferred from 7.7c.

In order to understand this result a *mixing* ratio Ξ is introduced which relates the width of the mixing region ξ to that of the 4π case

$$\Xi_{2\pi} = \frac{\xi(2\pi)}{\xi(4\pi)}\,. \tag{7.11}$$

As a representative value for the width of the mixing region ξ a horizontal line through a density value of $1\mathrm{cm}^{-3}$ is considered reasonable. This mixing ratio Ξ takes a value of 1.4 in case of the 2π run and a value of 4.1 in the cπ model. These figures clearly show that the mixing region between the two species undergoes a slight and a strong increase in case of the dayside and the cone shaped model, respectively. Mass-loading of the solar wind leads to an acceleration of the cometary ions which in turn due to momentum conservation causes a deceleration of the solar wind flow. In case of the cπ run the mass-loaded region is substantially increased. Bearing in mind that at such large distances the gradient of the cometary ion density is rather small, it becomes obvious that mass-loading of the solar wind occurs continuously and not so sharp as in the other cases. Therefore, the solar wind deceleration is smooth. In contrast to that, in the 2π case the mass-loading region increases but remains with a $\Xi_{2\pi}$ value of 1.4 comparable to the 4π case. Therefore, the

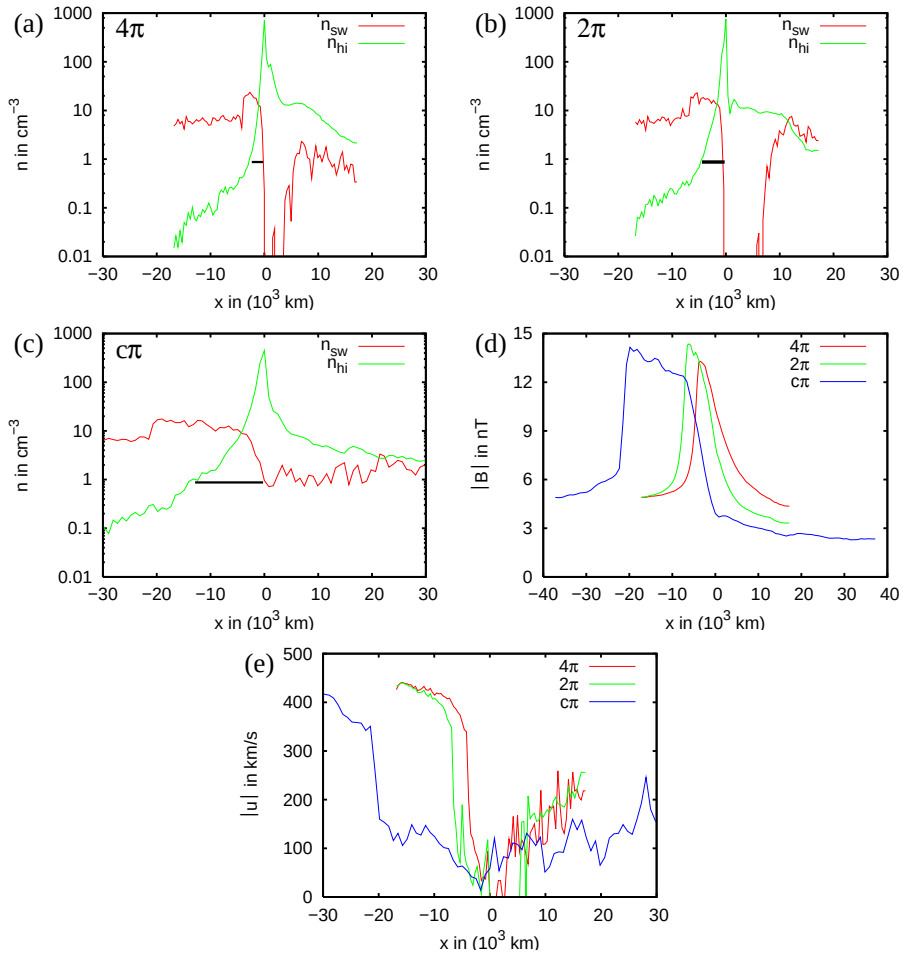

Figure 7.7: 1D plots along the x-axis at 1.30 AU. Fig. (a,b,c) show the solar wind and the cometary ion density for the three models. Fig. (d,e) compare the magnetic field and the solar wind bulk velocity for the investigated mass-loading patterns. Due to the high degree of mixing between the species in the cπ case (c) the ICB is only gradually developed. The increase of the mixing region between the two species leads to a broadening of the MBR shown in (d) and a smooth deceleration of the solar wind shown in (e). Figures from Gortsas et al. (2009).

velocity gradient is much steeper than in the cπ case. In addition, the degree of mixing remains weak so that an ion composition boundary is clearly developed. That confirms our findings of the previous section and is in good agreement with the respective figures of Fig. 7.7.

However, in case of the cπ run the mixing between the solar wind and cometary species, expressed by a mixing ratio $\Xi_{c\pi}$ of 4.1, occurs on a larger scale. Therefore, the ion composition boundary is only gradually established. The large scale mass-loading of the solar wind is also responsible for the broadening of the MBR. The magnetic field is no longer mainly transported by convection through the solar wind species but also with increasing intensity through the cometary species. Hence, an additional transport channel of the magnetic field from the barrier region away is established which hampers the

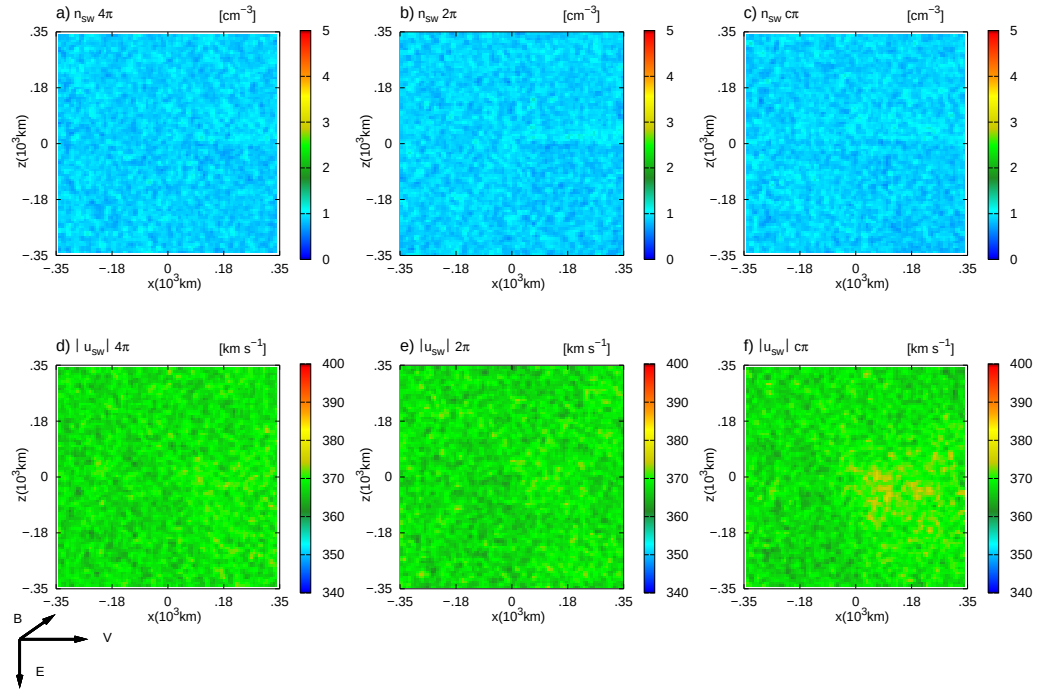

Figure 7.8: The SW-C interaction in the polar plane is displayed for the 4π, 2π, and $c\pi$ cases at a heliocentric position of 3.25 AU. The solar wind ion density and the solar wind bulk velocity are displayed. Water activity is very low leading to a negligible feedback to these solar wind paramters.

peak value and leads to the observed broadening of the magnetic field in Fig. 7.7d. The cometary bulk velocity plot in Fig. 7.6e shows that cometary ions reach rather high velocities in the region of 20.0 $\times 10^3$ km which is the position of the MBR. This corroborates the drawn conclusion that the cometary species is increasingly involved in the convective transport of the magnetic field.

The cone shaped model deviates stronger from the spherically symmetric case. It has been studied to simulate a strong neutral gas jet as observed for many comets, see for instance Schulz et al. (2004) for comet CG. This investigation reveals that increasing spatial confinement leads to an increase of the mass-loaded region along the Sun-comet line. This has three effects on the plasma environment of comets. First, the mixing region of solar wind and cometary species is increased which in turn opens an additional transport channel for the magnetic field from the MBR away. Hence, the MBR is broader. Second, this strong mixing leads to a gradually developed ion composition boundary. Finally, the deceleration of the solar wind is much smoother than in the previous cases.

7.5.4 Calculations at 3.25 AU

At a heliocentric distance of 3.25 AU CG is expected to be extremely faint with respect to water activity. Therefore, the feedback of cometary activity to the solar wind should be

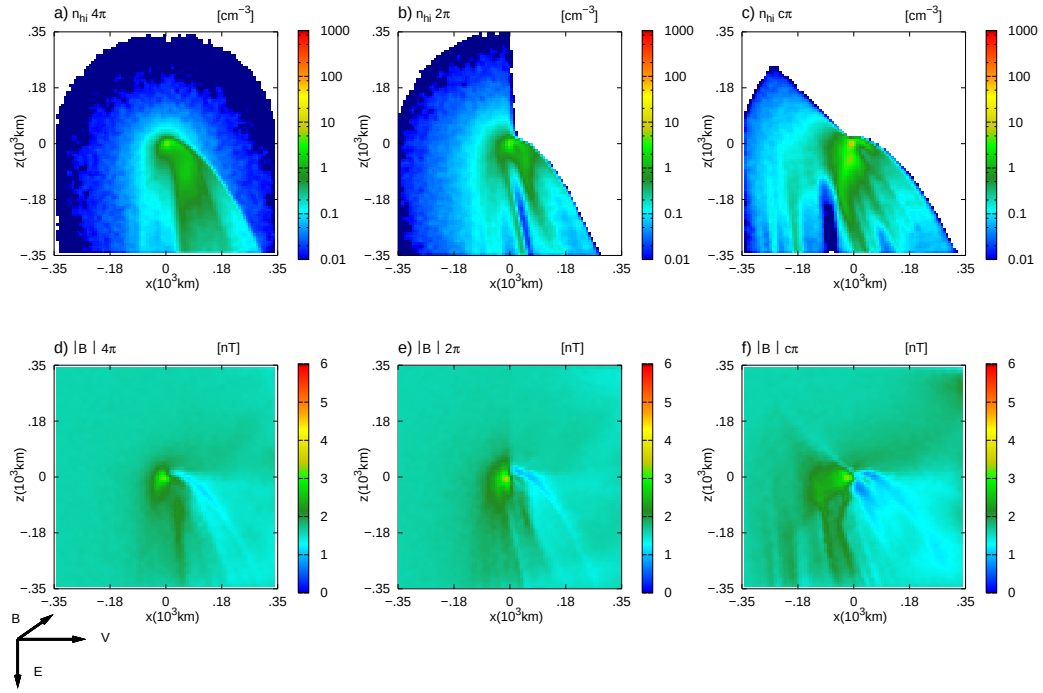

Figure 7.9: The SW-C interaction in the polar plane is displayed for the 4π, 2π, and $c\pi$ cases at a heliocentric position of 3.25 AU. The cometary ion density and the magnetic field are shown. The anisotropic outgassing patterns are clearly discernable. The magnetic field starts to deviate from the undisturbed solar wind conditions in the vicinity of the nucleus. Spatial confinement enhances this effect. Figures from Gortsas et al. (2009).

very weak. This expectation is confirmed by the simulation results shown in Fig. 7.8 and in Fig. 7.9. In these figures the polar plane is shown but the same conclusion holds for the terminator and the ecliptic planes which are therefore not shown here.

In the first column of Fig. 7.8 and Fig. 7.9 the results for the 4π case are shown. Due to the very faint nucleus the solar wind flow is not altered by the outgassing comet. The predominant flow direction throughout the simulation box remains the same. Only the magnetic fields in Fig. 7.9d show first modifications. These are localized and confined to the immediate vicinity of the nucleus. The pileup of the magnetic field leads to its increase by almost a factor of 2 compared to the background value. The developing twist of the magnetic field excites a fast magnetosonic wave which later on with increasing cometary activity leads to the formation of the linear Mach cone (Bagdonat and Motschmann 2002). Closer to perihelion this cross-section increases substantially causing the development of different plasma boundaries (see Chapter 8).

The global picture of the cometary ion density shown in Fig. 7.9a is characterized by the pick-up process. The newly born ions expand with an initial velocity of 1 km s^{-1} in radial direction. The convective electric and magnetic fields force the ions on a cycloidal trajectory. As the spatial extension of the simulation box is 600 km only the beginning of the cycloidal arc is shown. Assuming a velocity of 50 km s^{-1} the gyroradius of the

cometary ions $r_{g,hi}$ is approximately 5200 km. The transport direction of the heavy ions is a superposition of the cycloidal motion in -z direction dominated by the convective electric field and the guiding center drift parallel to the undisturbed solar wind flow. The twist of the magnetic field visible in Fig. 7.9d exposes a force on the cometary ion tail twisting it slightly in the solar wind flow direction. This is clearly visible in the cometary ion density of Fig. 7.9a. Due to the finite expansion velocity of newly born ions we can discern in Fig. 7.9a the formation of a so-called heavy ion density jump (HIDJ) (Bagdonat 2005). The high ion density close to the nucleus is enhanced by deceleration of heavy ions traveling in northward direction and their cycloidal transport in -z direction. With increasing cometary activity this HIDJ boundary develops into the ion composition boundary.

It can be summarized that cometary ions serve mainly as test particles despite first modifications of the electromagnetic field topology if cometary activity is as low as 10^{24} s^{-1}. This conclusion is in good agreement with previous results reported by Bagdonat and Motschmann (2002), Motschmann and Kührt (2006), and Hansen et al. (2007).

Switching to the second column of Fig. 7.8 and Fig. 7.9 the following picture emerges for the dayside restricted case. In analogy to the 4π case the effects of spatial confinement lead to negligible modifications of the solar wind plasma. The solar wind density and velocity field shown in Fig. 7.8b and e remain at the undisturbed solar wind conditions. However, the twist of the magnetic field is here again confined to the inner coma but it is getting stronger as shown in Fig. 7.9e. Now the jump in magnitude is given by almost a factor of 3. The spatial extension of this modification has increased by roughly a factor of 2. In Fig. 7.9b the dayside restricted ion cloud is discernable. As at this heliocentric distance the gyroradius of cometary ions is very large the transport of cometary ions in the downstream side is very weak and it occurs mainly in the -z hemisphere. That is the reason for the sharp boundary between upstream and downstream, especially in the +z hemisphere. Furthermore, the increasing modifications of the electromagnetic field topology lead to a stronger twist of the cometary ion tail in direction of the undisturbed solar wind flow in comparison to the 4π case of Fig. 7.9d.

Similar conclusions can be drawn from the cone shape model as shown in Fig. 7.8 and Fig. 7.9. Despite weak cometary activity spatial confinement of newly created ions lead to stronger modifications in the electromagnetic field topology. In distinction to the 4π and 2π cases the magnetic field is not only enhanced but but it also starts to detach from the nucleus. The center of the twisting magnetic field is now located some 120 km from the nucleus away. It covers an area of about 10^4 km^2 compared to the 250 km^2 of the 2π case. In Fig. 7.9c the cone shaped ion cloud is discernable. Similar to the 2π case the observed sharp boundaries in the +z hemisphere are due to the employed cone shape and the large gyroradius of cometary ions. Furthermore, the increasing modifications of the electromagnetic field topology lead to a stronger twist of the cometary ion tail in direction of the undisturbed solar wind flow.

7.6 Summary

In this chapter, the plasma environment of CG is investigated for different activity patterns. The model regards idealized and simplified configurations of real comets. Two

shape models of cometary activity are considered: a day side restricted and a cone shaped model. For comparison, the widely used spherically symmetric coma model is also calculated. The simulations are carried out for a heliocentric distance of 1.3 AU and 3.25 AU to address two different states of nucleus activity. The physical parameters are chosen in accordance to the expected conditions of CG during the Rosetta mission.

The day side restricted case leads to a perceived stronger comet compared to the spherically symmetric case. The plasma structures of CG are enhanced but qualitatively the interaction of the solar wind with the comet remains as in the 4π case. For the day side restricted case it can be concluded that the spatial activity pattern of the nucleus can quantitatively modify the positions and shapes of the plasma boundaries encountered at a comet and it has to be considered among other parameters, such as the electron temperature as investigated by Bösswetter et al. (2004) for Mars and by Bagdonat (2005) for weak comets in order to fit plasma simulations to observational data.

The $c\pi$ case reveals not only quantitatively but also qualitatively modifications of the plasma structures. Further increase of spatial confinement leads to a strong increase of the mass-loading region. The location of the bow shock is pushed further to the Sun by a factor of 4.5 compared to the 4π case. The mixing region between the solar wind species and the cometary species is increased by a factor of 4.1. This has three effects on the plasma environment: First, the increasing mixing of the two different species opens an additional transport channel for the magnetic field. With increasing intensity the magnetic field can also be transported by the cometary species which leads to a broadening of the magnetic barrier region. Second, the increasing degree of mixture between the species leads to an ion composition boundary which is only gradually developed. Third, it is found that the deceleration of the solar wind is much smoother than in the 2π and 4π cases.

The investigations at 3.25 AU confirmed previous results reported by Bagdonat and Motschmann (2002), Motschmann and Kührt (2006), and Hansen et al. (2007). The nucleus is so faint that despite spatial confinement almost no modifications of the solar wind flow occurs. For such low production rates cometary ions serve mainly as test particles. Only the electromagnetic field topology exhibits first modifications which are spatially confined to the vicinity of the nucleus. With increasing spatial confinement the pileup of the magnetic field increases but its cross-section remains too small to cause any visible effects on the solar wind flow. The increased magnetic field leads only to a stronger twist of the cometary ion tail in direction of the solar wind flow. In addition, increasing confinement causes a detachment of the magnetic field pileup region from the immediate vicinity of the nucleus.

8 Perihelion approach of 67P/Churyumov-Gerasimenko

8.1 Introduction

The plasma environment of comet CG during its journey into the inner Solar System is simulated by combining the hybrid plasma model with the thermophysical nucleus model developed in the first part of this thesis. This combined effort provides inside into the evolution of the plasma environment of weak comets with increasing activity. In a review of the current understanding of the plasma environment of JFC comets Coates and Jones (2009) emphasized among other not yet understood aspects of the SW-C interaction also the need to study the perihelion approach of a comet.

A key input parameter of the hybrid plasma model is the outgassing strength. In the present investigation the major cometary ion species is considered, e.g. water group ions. The simulation of the CO activity of comet CG in Chapter 5, however, showed that water is the major component in the coma only when the comet is close to the Sun. Depending on the employed parameters the crossing point of a CO dominant to a water dominant coma is at around 4 AU. In this investigation the simulation will be restricted to water as the major component in the coma. In the next chapter, the contribution of CO in a two-ion-coma simulation will be investigated in detail. The water outgassing strength of this chapter is calculated for a nucleus model of CG with heat conduction, heat advection, gas diffusion, sublimation, and condensation. The temperature remapping technique is switched on.

Previous articles concerning the plasma environment of comets were performed at some fixed heliocentric distance and the outgassing strength was set to an estimated number based on observations or it was derived from a simple outgassing model (Lipatov et al. 2002, Motschmann and Kührt 2006, Delamere 2006, Gortsas et al. 2009). Among the first studies of the dynamic and very complex phenomenon of a comet approaching the Sun and thereby gaining strength in its outgassing of volatile materials has been presented by Bagdonat and Motschmann (2002). The authors studied the plasma environment of comet 46P/Wirtanen for few heliocentric distances between 3.25 AU to 1 AU in 2 D and 3 D. Based on characteristic plasma structures different interaction regimes were identified. An improved investigation was presented by Hansen et al. (2007) who applied the hybrid plasma model of Bagdonat and Motschmann (2002) and the MHD model of Gombosi et al. (1996) to investigate the plasma environment of CG at four fixed heliocentric distances. This investigation has shown that important insight in the plasma environment of comets is obtained through a kinetic approach as presented in the hybrid plasma model.

Table 8.1: Parameter used to calculate the B_{imf} and the solar wind proton density n_0 as function of heliocentric distance.

Parameter	Symbol	Value
Reference position of Parker Model	r_b	1 AU
Angular momentum of the Sun	ω	2.6×10^{-6} rad s^{-1}
IMF at r_b	B_0	5 nT
Solar wind proton density at r_b	n_0	6 cm^{-3}
Solar wind bulk velocity at r_b	u_{sw}	430 km s^{-1}

Especially far from perihelion a kinetic description reveals important aspects of the solar wind-comet interaction.

The characteristic feature of this study is the thermal model employed to calculate the water activity of CG and the quasi continuous simulation of cometary approach to perihelion. The simulation starts at 4.2 AU and finishes at 1.3 AU with a step size in heliocentric direction of 0.1 AU. In the presentation of the simulation results strong emphasize is laid on the evolution of the cometary ion flux and the magnetic field compared to the undisturbed solar wind and the interplanetary magnetic field B_{imf}. The simulation results are compared with analytical formula for the bow shock standoff distance. Scaling laws of important boundaries are also presented.

8.2 Background values of the solar wind

The interplanetary magnet field and the solar wind proton density are necessary to perform a hybrid plasma simulation. According to Parker (1958) the magnetic field expands from the Solar corona as

$$\begin{aligned} B_r(r,\theta,\phi) &= B(\theta,\phi)\left(\frac{r_b}{r}\right)^2, \\ B_\theta(r,\theta,\phi) &= 0, \\ B_\phi(r,\theta,\phi) &= B(\theta,\phi)\left(\frac{r_b}{r}\right)^2\left(\frac{\omega}{u_{sw}}\right)(r-r_b)\,\sin\theta\,. \end{aligned} \tag{8.1}$$

ω, u_{sw}, r_b, B_0 denote the angular momentum of the Sun, the streaming velocity of the solar wind, a reference position from the Sun beyond which solar gravitation and acceleration by high coronal temperatures may be neglected, and the magnetic field at r_b. The values used in the simulations are summarized in Table 8.1. The background solar wind proton density is obtained by a fit to Voyager and IMF 8 data published by Richardson et al. (1995). It is a rational law

$$n_0(r) = n_0(r_b)\, r^{-1.93}\,. \tag{8.2}$$

Figure 8.8 and 8.7 display the B_{imf} and n_0 as function of heliocentric distance. For all simulations, it is assumed that the B_{imf} lies in the orthogonal plane of the solar wind flow direction discarding the fact that the orientation of the magnetic field is highly dynamic

Table 8.2: Input parameter of the hybrid model for the perihelion approach.

Parameter	Symbol	Value
Heliocentric distance	r_H	4.2 ... 1.3 AU
Expansion veloc. of com. neutrals	u_n	1 km s^{-1}
Outgassing strength	Q	10^{24}... $4.4 \times 10^{27} s^{-1}$
SW plasma beta	$\beta_{e,sw}$	0.5
Cometary plasma beta	$\beta_{e,c}$	0.04
Ionisation rate	ν	10^{-6} s^{-1}
Number of grid points		90×90×90

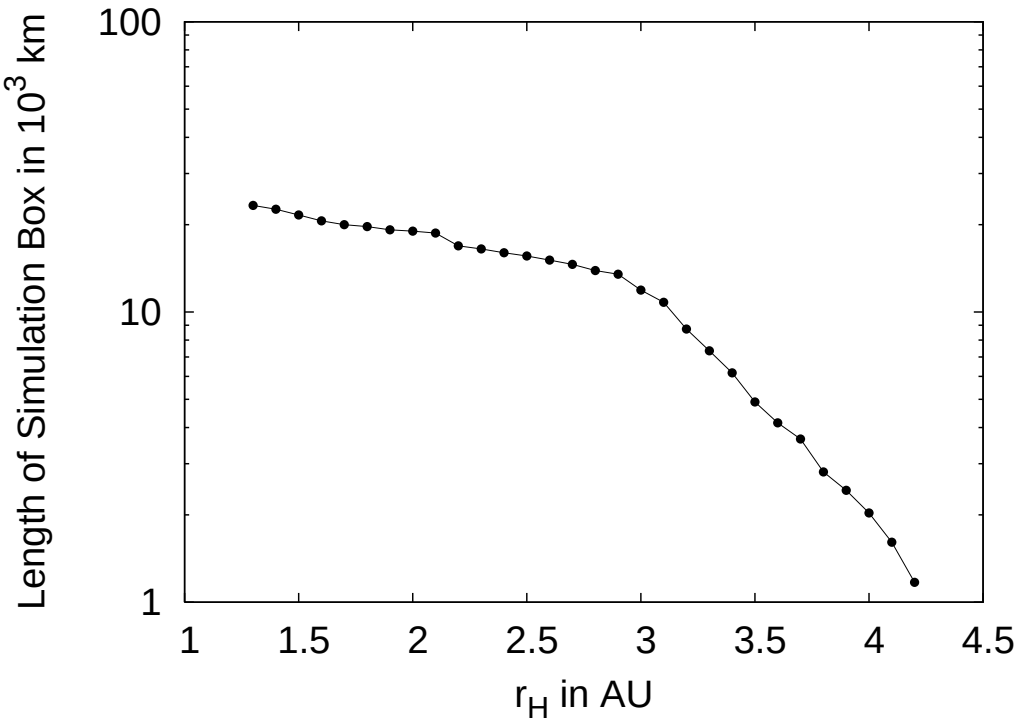

Figure 8.1: The edge length of the simulation box as function of heliocentric distance. Water activity increases by more then 3 orders of magnitude during perihelion approach making an adaptation of the box dimensions necessary. A trial-error-approach was employed with the constrain to keep characteristic structures of the solar wind-comet interaction around the middle of the box.

and changes with the rotation of the Sun. This assumption, however, is employed to simplify the analyses of the simulation results without adding to much effects right from the start.

8.3 Simulation method

Previous plasma simulations of comets have revealed the existence of several characteristic interaction regimes. It is thus important to cover all these regimes with the simulation of CG's perihelion approach. The first regime is the test-particle regime which was identified at around 3.25 AU from the Sun by Lipatov et al. (2002),Bagdonat and Motschmann (2002), and Hansen et al. (2007). The water production rate of the comet at this heliocentric distance is 10^{24} s^{-1}. The present simulation of CG's outgassing pattern yields such a production rate of water at around 4.2 AU. Hence, the simulation starts at this heliocentric distance from scratch. After the calculation has reached stationarity, the result is used as input for the next heliocentric position at 4.1 AU. This is continued until CG's perihelion position at 1.3 AU. The same boundary conditions as in Section 7.4 have been used for this study. Important input parameters of the hybrid model are listed in Table 8.2.

By applying this technique, the time to fill the simulation box is reduced allowing to conduct efficiently this elaborate simulation. As the code is working only with normalized values, it is also important to adjust the input values of the (n+1) simulation which has as input the simulation result of the (n) run. As the comet production rate increases by more then 3 orders of magnitude it is necessary to adapt the size of the simulation box. This is done in an trial-and-error fashion with the constrain to keep important plasma structures, like the bow shock, around the middle of the simulation box and to get a smooth transition between adjacent steps. The simulation domain increases from 1.2×10^3 km at 4.2 AU to 24.0×10^3 km at CG's perihelion position. The edge length of the simulation box is displayed in Fig. 8.1. Besides the length of the simulation box also the solar wind background values and the outgassing strength are adapted at each heliocentric step according to Fig. 8.8 and Fig. 8.7. The same boundary conditions as in Section 7.4 have been used for this study.

Variations in the ambient solar wind conditions are considered in the sense that the background solar wind proton density n_0 and the B_{imf} are functions of heliocentric distance. This simplifying approach neglects interesting phenomenon which are due to the dynamic nature of the solar wind plasma. With this assumption it follows that it is sufficient to simulate the movement of the comet towards the Sun only through adaptation of the solar wind conditions and the outgassing strength of the comet. The characteristic time scale of the nucleus movement on its orbit exceeds by far the time scale for the plasma environment to reach stationarity. Effects in the coma which are due to the movement of the comet and which might impact the plasma environment of the comet are also not resolved. But currently, even the most advanced coma simulations do not take the diurnal rotation of the comet nor the movement of the comet on its orbit to the Sun into account (Tenishev et al. 2008).

The outgassing pattern in the hybrid code is spherically symmetric and the outgassing strength is derived from the thermal model developed in the first part of this thesis. The model consists of water ice, CO ice, and dust in a porous ice-dust matrix similar to Chapter 5. A thermal conduction coefficient of 10^{-2} W m^{-1} K^{-1} has been used. The Stefan problem was also used in the calculation.

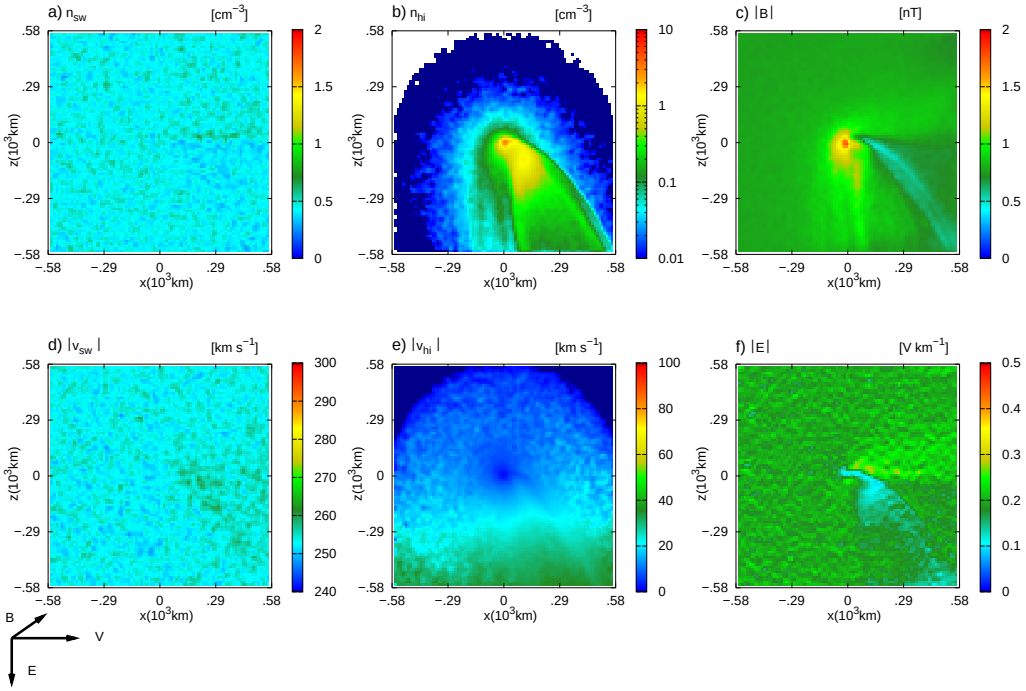

Figure 8.2: The solar wind-comet interaction in the polar plane at 4.2 AU is displayed. The solar wind ion density (a), the cometary ion density (b), the magnetic field strength (c), the solar wind ion bulk velocity (d), the cometary ion bulk velocity (e), and the electric field (f) are displayed. Water activity is low causing almost no effects on the solar wind ion properties. Only the magnetic and electric field show first reactions to the comet which are confined in the vicinity of the nucleus. The cometary ion tail is almost perpendicular to the solar wind flow direction. This is the test particle regime.

8.4 Simulation results

The simulation results for the water outgassing strength are displayed in Fig. 8.7. The water sublimation curve is fitted to observations of Schleicher (2006) by integrating over the whole nucleus and by assuming that 3 % of the total surface is active. At 4.2 AU the comet is very faint reaching an integrated water activity of 10^{24} s^{-1}. At such large heliocentric distances water activity is very low. But other more volatile species can sublime from the nucleus despite low energy input from the Sun. Such a volatile species would be CO. For the present investigation, however, only water vapor is considered in the hybrid plasma model. Depending on the simulation parameters of the thermal model water exceeds CO outgassing between 4 AU to 3.5 AU. Therefore, the role of CO is not further investigated here. At perihelion, the comet reaches a water outgassing strength of 4.4×10^{27} s^{-1}. Thus, during the simulation cometary water activity increases by more than three orders of magnitude.

8.4.1 2D view on the solar wind-comet interaction

The approach of comet CG to perihelion starting at 4.2 AU shall be presented in 2 dimensional contour plots. In Fig. 8.2 the solar wind ion density, the cometary ion density, the magnetic field strength, the solar wind ion bulk velocity, the cometary ion bulk velocity, and the electric field are displayed in the polar plane of the coordinate system defined in Fig. 7.2. The same format has been chosen for Fig. 8.3, Fig. 8.4, Fig. 8.5, and Fig. 8.6 showing the results at 3.7 AU, 2.7 AU, 2 AU, and 1.3 AU, respectively.

At 4.2 AU cometary water activity is low compared to the peak value at perihelion leading to almost no feedback on the solar wind. In Fig. 8.2a and d the solar wind density and bulk velocity remain in the state of the undisturbed solar wind flow. The magnetic and electric fields show first modifications which are confined in the vicinity of the nucleus as shown in Fig. 8.2c and f. The magnetic field exhibits an enhancement by a factor of 2 compared to the background values. The cometary ion tail is oriented perpendicular to the solar wind flow direction as result of the pickup process of freshly ionized particles. As described e.g. in Lipatov et al. (2002) and Bagdonat and Motschmann (2002) the mechanism for the perpendicular orientation of the tail is due to a very small initial velocity compared to the undisturbed solar wind flow $\mathbf{u}_{sw}$ leading to a convective electric field $\mathbf{E}$ given as

$$\mathbf{E} = -q\,\mathbf{u}_{sw} \times \mathbf{B}\,. \tag{8.3}$$

As cometary ions are accelerated they start to follow a gyromotion due to an increasing contribution by

$$\mathbf{E} = q\,\mathbf{v}_{hi} \times \mathbf{B}\,, \tag{8.4}$$

with $\mathbf{v}_{hi}$ being the cometary ion velocity. The superposition of these forces leads to the cycloidal arcs. But generally, the velocity of the cometary ion population is low as shown in Fig. 8.2e. Cometary ions behave mainly like test particles. The emerging picture at 4.2 AU corresponds to the test particle regime described in the articles of Lipatov et al. (2002), Bagdonat and Motschmann (2002), Motschmann and Kührt (2006), and Hansen et al. (2007). Haerendel et al. (1986) reported about a similar behavior seen during the artificial comet of the AMPTE/UKS experiments. As pointed out in Hansen et al. (2007) the almost perpendicular orientation of the tail is not seen in single-fluid magnetohydrodynamic simulations of comets. A jump in the heavy ion density can be discerned in Fig. 8.2b. As described in Hansen et al. (2007) this jump can not be interpreted as an ion composition boundary as the solar wind completely penetrates the coma but this structure will later evolve to a boundary separating the solar wind from the cometary plasma. The test-particle regimes extends to around 3.7 AU from the Sun as shown in Fig. 8.3. At this heliocentric distance cometary activity has increased by an order of magnitude as shown in Fig. 8.7. The solar wind ion density and bulk velocity in Fig. 8.3a and d show first indications of the linear Mach cone. This asymmetric cone structure is caused by the increasing coma around the nucleus with high cometary ion density but not the nucleus itself. As discussed in Hansen et al. (2007) the cometary coma is not symmetric but due to the pickup process asymmetric and not comparable to a point source. Therefore, an asymmetric cone is excited in difference to a symmetric structure in case of a point source in a superfast flow. The density of cometary ions around the nucleus has increased by an order of magnitude compared to the 4.2 AU case. The tail of the comet is not perpendicular anymore but has slightly rotated in solar wind flow direction. Below the flank in Fig.

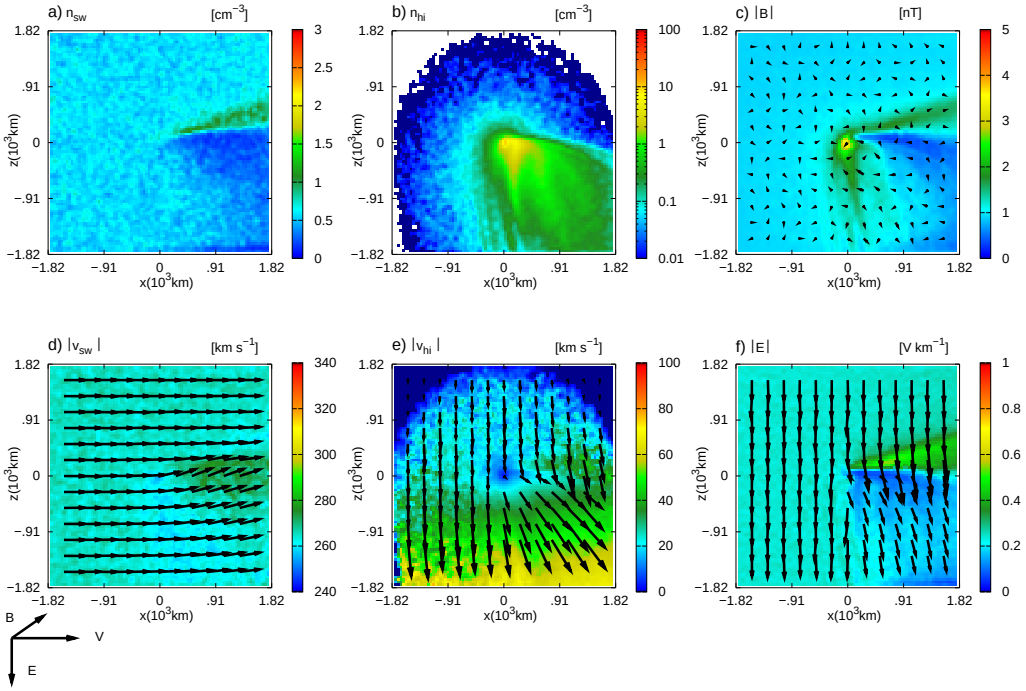

Figure 8.3: The solar wind-comet interaction in the polar plane at 3.7 AU is displayed with the same quantities as in Fig. 8.2. Water activity has increased by an order of magnitude. The transition from the test-particle regime to the linear Mach cone is characterized by the formation of a flank in the solar wind ion density, the magnetic field, the electric field, and the rotation of the tail from almost 90° to 45° with respect to the solar wind flow direction.

8.3a the proton density is decreasing compared to the undisturbed solar wind flow. The deflection of the incoming solar wind at the inner coma is getting stronger. As Fig. 8.3e shows the predominant flow direction of cometary ions is around 45° below the solar wind flow direction. The magnetic field in Fig. 8.3c is enhanced in front of the nucleus while downstream there is a region behind the nucleus evolving with magnetic field strengths below the interplanetary magnetic field indicating that the penetration of the cometary tail by the solar wind flow is getting weaker.

From 3.7 AU to 2.7 AU water activity has increased by a factor of 25. The feedback of the growing comet to the solar wind is getting stronger. In Fig. 8.4a the linear Mach cone is clearly developed. The comet has grown leading to a stronger deflection of the incoming solar wind particles. The primary flow direction of the solar wind in the +z hemisphere is in direction of the Mach cone as shown in Fig. 8.4d. The tail of the comet in Fig. 8.4b is oriented parallel to the solar wind flow direction continuing the rotation during the test-particle regime. The magnetic pileup at the stronger head of the nucleus leads to an enhancement of the magnetic field. The electric field in Fig. 8.4f shows that the field drops to very low values in the region of enhanced cometary ion density. The energy of the electric field is used to accelerate the cometary ions which have an initial velocity of only 1 km s^{-1}. The electric field in the region with the linear Mach cone is enhanced and points into the region with increased cometary ion density. As investigated

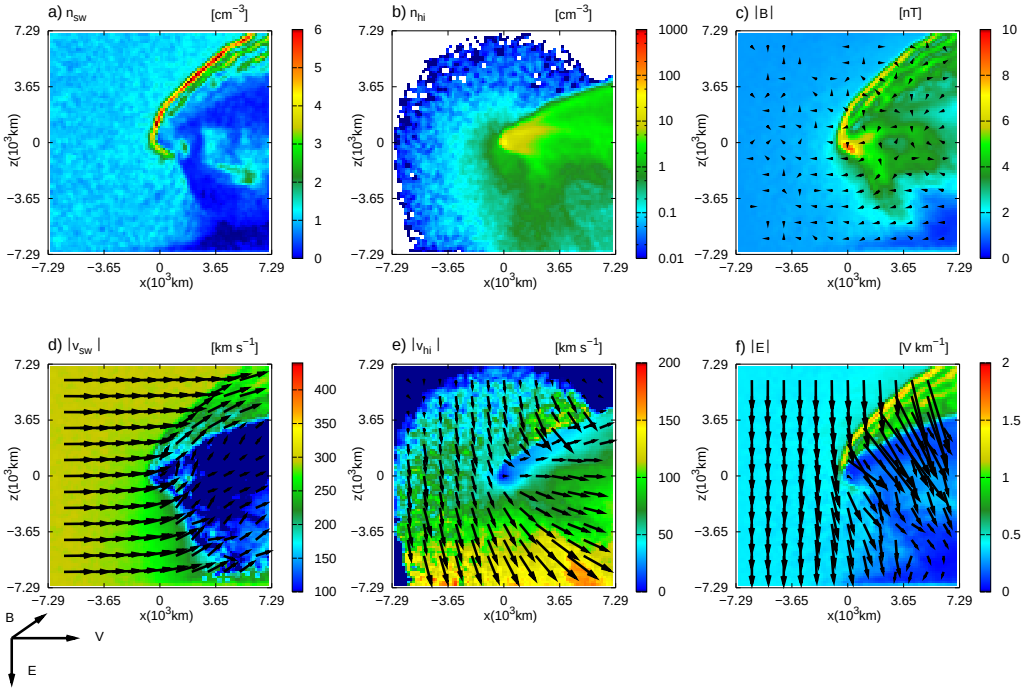

Figure 8.4: The solar wind-comet interaction in the polar plane at 2.7 AU is displayed for the same quantities as in Fig. 8.2. Water activity has increased by a factor of 25 compared to 3.7 AU. As the comet has grown the incoming solar wind is more and more deflected upwards leading to the formation of the linear Mach cone which is fully developed. The cometary ion tail has rotated in anti-sunward direction and the head of the comet has increased. The penetration of the cometary tail by the solar wind ions is getting weaker leading to low solar wind ion densities in the downstream side. The decreasing penetration of the tail leads also to a stronger draping of the magnetic field around the comet.

by Simon et al. (2007) for Mars and Titan a combination of the electric field and electron pressure forces leads to the formation of a sharply pronounced boundary layer. In the interval from 3.7 AU to 2.7 AU the plasma structures are asymmetric with respect to the z-axis.

A third regime can be discerned in the simulation covering a heliocentric distance from 2.7 AU to around 2 AU. According to the water activity curve shown in Fig. 8.7 nucleus activity has increased by a factor of 4. The coma of the nucleus is spatially growing providing a strong obstacle to the solar wind flow as shown in Fig. 8.5b compared to Fig. 8.4b at 2.7 AU. The penetration of the coma by the solar wind is getting weaker than in the previous regime. The comet is growing in -z direction yielding a stronger separation of the solar wind and cometary plasma. The linear Mach cone splits during this interval in several rays. In addition, the proton pileup boundary starts to evolve also in the -z direction reducing the asymmetry of the linear Mach cone regime. The magnetic field strength is also growing in -z direction reducing the asymmetry in Fig. 8.3c. Figure 8.5e shows that the bulk velocity of the cometary ion population is getting higher reaching values at around 150 to 200 km s^{-1}.

The last regime covers the range from 2 AU to 1.3 AU the perihelion distance of CG.

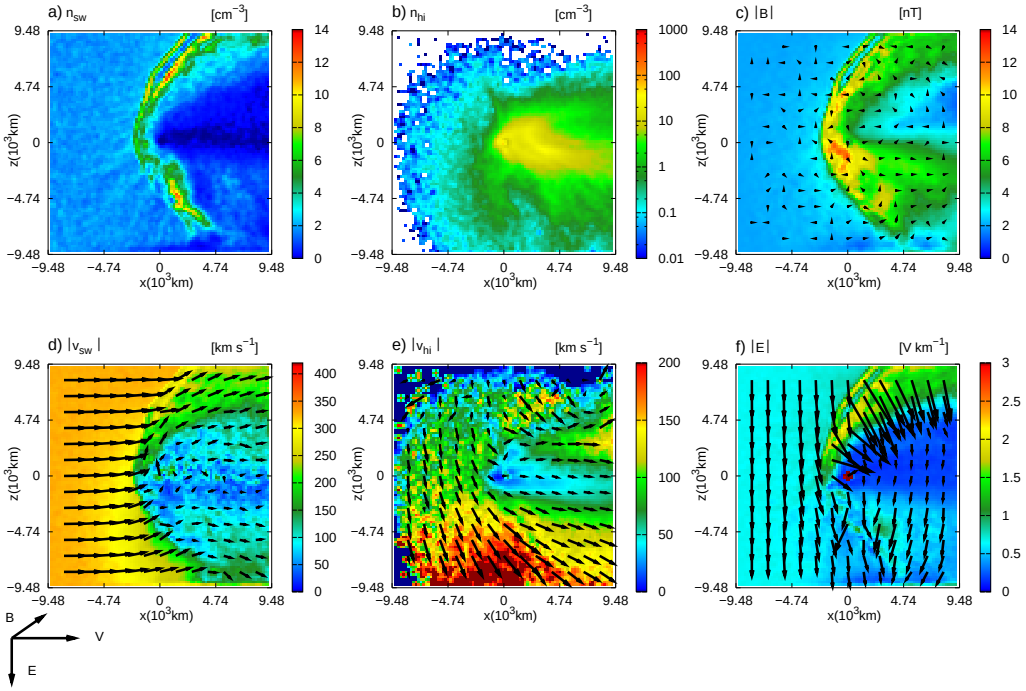

Figure 8.5: The solar wind-comet interaction in the polar plane at 2 AU is displayed for the same quantities as in Fig. 8.2. Water activity has increased by a factor of 4 compared to 2.7 AU. The linear Mach cone splits in two rays indicating that the nucleus is now in the nonlinear Mach cone regime. The plasma structures show the transition to a quasi-symmetric state. The coma is growing and extending in -z direction reaching higher velocities compared to the 2.7 AU case.

This is the shock formation regime. A parabolic structure separates the hot solar wind plasma from the cold cometary ion plasma. The mass loading of the solar wind leads to a deceleration of the solar wind flow in flow direction. As a result a shock evolves. The solar wind proton density and the cometary ion density are complementary. The former reaches low values where the latter exhibits large values. The coma grows also in -z direction following the convective electric field shown in Fig. 8.6b and f, respectively. The magnetic barrier region is fully developed as the mixing between the solar wind ion population and the cometary ion population remains weak. The solar wind ions are deflected around the dense part of the coma leading to an enhancement of the magnetic field.

The proposed division of the simulation range in four interaction regimes appears to be in good agreement with the investigation of Hansen et al. (2007). There are, however, also differences. The test-particle regime is further away from the Sun in the ranges from 4.2 AU to 3.7 AU while in Hansen et al. (2007) this regime was at 3.25 AU. This is mainly due to different water outgassing curves. The formation of the Mach cone was identified by Hansen et al. (2007) at 2.7 AU which coincides well with the present investigation. According to the present simulation the Mach cone evolves between 3.7 AU to 2.7 AU. At 2 AU Hansen et al. (2007) identified the non-linear Mach cone with the splitting into several rays. As the comet approaches its perihelion position the Hansen

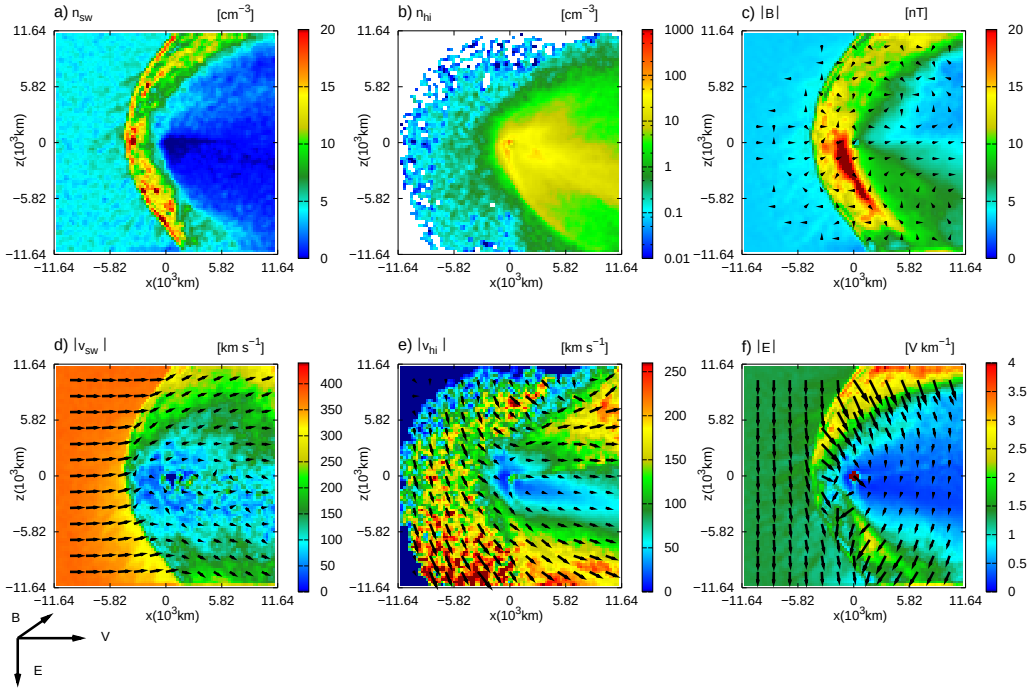

Figure 8.6: The solar wind-comet interaction in the polar plane at 1.3 AU is displayed showing the same quantities as in Fig. 8.2. Water activity has increased by a factor of 4 compared to the 2 AU case. The bow shock is clearly developed in the solar wind ion density as a parabolic structure separating the solar wind ion plasma from the cold cometary ion plasma. The coma has grown in -z direction. As the solar wind plasma cannot penetrate the dense part of the coma the magnetic field froze-in the solar wind drapes around the obstacle.

et al. (2007) and the present investigation converge as the differences in the employed water activity get smaller. To conclude the present investigation is in good agreement with similar investigations of CG's approach to the Sun. In the next section a global view on the perihelion approach of CG will be given.

8.4.2 Global view on the solar wind-comet interaction

The maximum cometary ion flux and magnetic field strength are displayed as functions of heliocentric distance in Fig. 8.7 and in Fig. 8.8, respectively. At 4.2 AU cometary activity is low yielding a maximum value of the cometary ion flux which is an order of magnitude below the undisturbed solar wind ion flux as displayed in Fig. 8.7. At around 3.7 AU, cometary activity has increased yielding a maximum ion flux comparable to the undisturbed solar wind ion flux. The evolution of the magnetic field is depicted in Fig. 8.8. At the beginning, the maximum of the magnetic field is a factor of 2.5 above the B_{imf}. This value is reached in front of the nucleus while further away the magnetic field remains as in the undisturbed solar wind. At 3.7 AU this factor rises to a value of almost 5. The interval starting at 4.2 AU to 3.7 AU exhibits features which are characteristic to the test-particle regime as described in Bagdonat and Motschmann (2002). The comet is

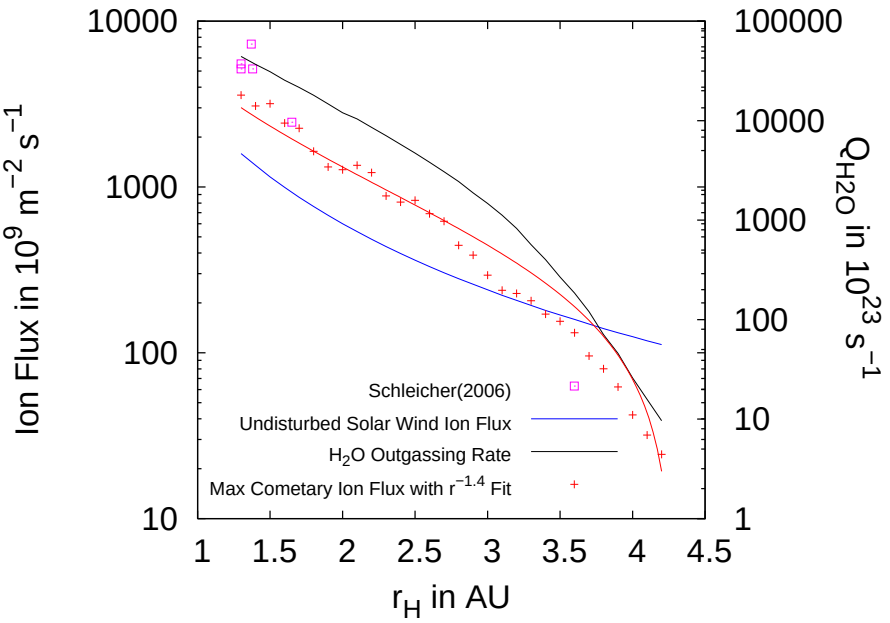

Figure 8.7: Left scale: Maximum of the cometary ion flux as a function of heliocentric distance. The maximum is taken from the whole simulation domain and fitted with a rational law $r^{-1.4}$. For comparison the undisturbed solar wind ion flux is also shown. Three regimes can be distinguished. At the beginning, the solar wind ion flux exceeds the cometary ion flux, this is the test particle regime covering the range from 4.2 AU to 3.7 AU. Around 3.7 AU, these quantities reach the same values. This regime is referred to as Mach cone regime which covers the range up to 2.7 AU. From 2.7 AU to 1.3 AU, the maximum cometary ion flux exceeds the solar wind ion flux clearly. This is the shock formation regime. Right scale: Total water outgassing rates. Figure from Gortsas et al. (2010b).

too faint to cause any significant feedback to the solar wind.

The simulation data allows to identify a second regime covering a heliocentric range from 3.7 AU to 2.7 AU. In this interval, the growth of cometary activity is a factor of 25. This growth process is followed by the cometary ion flux which exceeds the solar wind flux by a factor of 2 at the end of the interval. The magnetic field exceeds the B_{imf} by a factor of 7. Compared to the factor at 3.7 AU this makes a moderate enhancement of about 1.4. This regime has been characterized in previous studies of the solar wind-comet interaction by the formation of the linear Mach cone (Lipatov et al. 2002, Bagdonat and Motschmann 2002).

The last regime spans the distance from 2.7 AU to 1.3 AU. In this interval, cometary activity increases by more than an order of magnitude. The maximum of the cometary ion flux and of the magnetic field, however, seem to grow only moderately. Both quantities exceed the background values of the solar wind by a factor of 2 and 7, respectively; factors that were already reached at 2.7 AU. Hence, despite the growth in cometary activity by an order of magnitude the maximum of the magnetic field and the cometary ion flux seem to follow the growth of the interplanetary magnetic field strength and the solar wind ion flux. In previous investigations of the solar wind-comet interaction this last regime

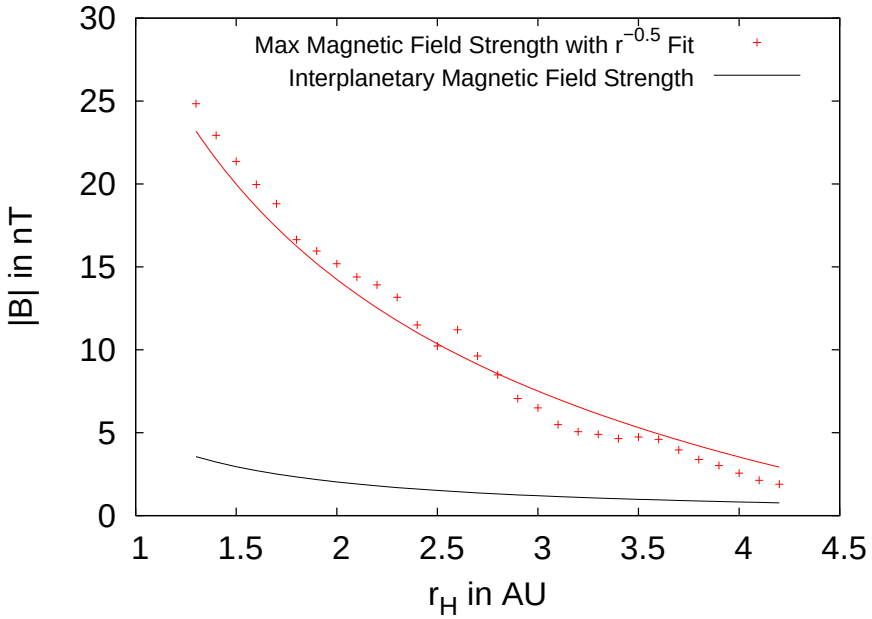

Figure 8.8: The maximum of the magnetic field as function of heliocentric distance is shown. The maximum is taken from the whole simulation domain and fitted with a rational law of $r^{-0.5}$. For comparison the interplanetary magnetic field is also depicted. As the comet approaches the Sun the magnetic field maximum exceeds the B_{imf} by a factor 2.5 at 4.2 AU to a factor 7 at 1.3 AU. The enhancement of the magnetic field at 4.2 AU is close to the nucleus surface as also shown in Fig. 8.2c. As the comet approaches the Sun the maximum of the magnetic field detached from the nucleus surface and affects large regions around the nucleus as also displayed in Fig. 8.6c. See also Fig. 8.9 on the position of the magnetic pile-up region along the Sun-comet line. Figure from Gortsas et al. (2010b).

was characterized by the splitting of the Mach cone and the formation of a bow shock (Bagdonat and Motschmann 2002).

In the global view of the solar wind-comet interaction the splitting of the Mach cone and the formation of the bow shock cannot be separated. These structures evolve from 2.7 AU to perihelion.

8.4.3 Shocks and cometary characteristics

The position of the bow shock R_{bs} relative to the comet as function of heliocentric distance is compared with an analytical formula derived by Biermann et al. (1967). Assuming a stationary flow in an axial symmetric 1 D model of the solar wind the mass flux equation reads as (Biermann et al. 1967)

$$\frac{d(\rho_m\, u)}{dx} = \frac{Q\, m_i}{4\,\pi\, u_g\, \nu^{-1}\, r^2}\,. \tag{8.5}$$

Integrating this equation from the undisturbed solar wind conditions to the location of the bow shock leads to the following expression for the standoff distance R_{bs} (Biermann et al.

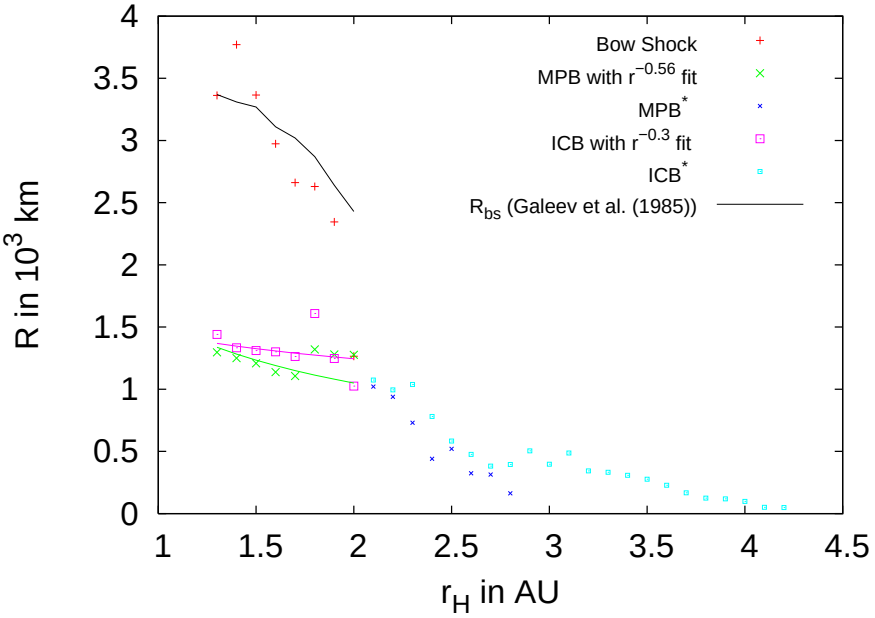

Figure 8.9: The bow shock (BS), the magnetic pileup boundary (MPB), and the ion composition boundary (ICB) position along the Sun-comet line as function of heliocentric distance are displayed. The BS position agrees well with an analytical formula of Galeev et al. (1985). The MPB and the ICB are well fitted by $r_H^{-0.56}$ and $r_H^{-0.3}$ law, respectively. Both boundaries remain in close vicinity over the relevant heliocentric range. Beyond 2 AU all three boundaries are not well defined because the nucleus is too weak. Therefore, the MPB* and the ICB* carry a superscript. They are only displayed for illustration purposes. Figure from Gortsas et al. (2010b).

1967, Galeev et al. 1985)

$$R_{bs} = \frac{Q\, m_i}{4\,\pi\, u_g\, \nu^{-1}\, \rho_\infty\, u_\infty [(\hat{\rho}\,\hat{u})_c - 1]}\,. \tag{8.6}$$

m_i, u_g,ν, ρ_∞, and u_∞ denote the cometary ion mass of the water species, the escape velocity of the ions, e.g. 1 km s^{-1}, the ionization rate, e.g. 10^{-6} s^{-1}, the background solar wind proton mass density, and velocity. $(\hat{\rho}\,\hat{u})_c$ denotes the critical mass flux ratio of the contaminated solar wind for shock formation. A continuous solar wind flow is possible only until the point at which the mean molecular weight of the solar wind particles reaches a critical value. This value was estimated by Biermann et al. (1967) to be $(\hat{\rho}\,\hat{u})_c = 4/3$ based on a simplified one dimensional model. Schmidt and Wegmann (1982) showed that for 1P/Halley at 1 AU a shock wave with Mach number 2 occurred at a distance from the nucleus where $(\hat{\rho}\,\hat{u})_c = 1.185$. Huddleston et al. (1992) employed Eq. (8.6) under the assumption that the critical number $(\hat{\rho}\,\hat{u})_c$ is mainly a function of the cometary ion flux while the solar wind ion flux is set to the undisturbed background values far from the comet. The authors obtained estimates for the shock position of 6.6×10^3 km for comet 26P/Grigg-Skjellerup along the Sun-comet line with a $(\hat{\rho}\,\hat{u})_c$ value of 1.22. In the present investigation, the critical value $(\hat{\rho}\,\hat{u})_c$ is used as a fit parameter. It turns out that the hybrid simulation data of the standoff distance are well fitted by Eq. (8.6) if $(\hat{\rho}\,\hat{u})_c$ has a value of 2.05. At perihelion, the standoff distance of CG is 3.37×10^3 km which is a factor of

Table 8.3: Scaling laws. r_H denotes heliocentric distance. Fits to the hybrid plasma simulation data are listed here. The linear dependence of the Galeev et al. (1985) formula on the outgassing strength Q was confirmed by the present hybrid plasma simulation. R denotes the position of the boundary from the nucleus along the Sun-comet line.

67P/Churyumov-Gerasimenko		
R_{bs}	3.4×10^3 km	
R_{bs}	$\sim Q$	confirmed
R_{mpb}	$\sim r_H^{-0.56}$	
R_{icb}	$\sim r_H^{-0.3}$	
$\|F_{hi}\|_{max}$	$\sim r_H^{-1.4}$	
$\|B\|_{max}$	$\sim r_H^{-0.5}$	

2 below the value of comet 26P/Grigg-Skjellerup which has almost the same outgassing strength as CG at perihelion.

The standoff distance of the bow shock, the position of the ion composition boundary, and of the magnetic pile-up boundary as function of heliocentric distance are displayed in Fig. 8.9 from 2 AU to perihelion as these boundaries are not well defined beyond 2 AU. The outgassing strength of the nucleus is too low beyond 2 AU. The ICB is defined as the location of the cross point along the Sun-comet line of the solar wind proton density and the cometary ion density. The position of the MPB is represented by the peak value of the magnetic field strength. The ICB and MPB coincide well at perihelion while further away from the Sun these boundary appear to follow different patterns. The ICB follows a $r^{-0.3}$ fit while the MPB a $r^{-0.56}$ fit. The later is comparable to the fit of the maximum magnetic field in the simulation domain of $r_H^{-0.5}$ as presented in Fig. 8.8. The coincidence of the ion composition boundary and the magnetic pileup boundary at comet CG has also been observed at planet Mars by Bösswetter et al. (2004). The fit to the cometary ion flux maximum shown in Fig. 8.7 is $r_H^{-1.4}$. A summary of the fit laws can be found in Table 8.3.

8.5 Summary

The evolution of the plasma environment of comet CG is investigated as the comet approaches the Sun. The plasma environment is calculated with the quasi-neutral, three dimensional hybrid plasma model while the thermal model presented in the first part of this thesis is used to calculate the water activity.

The simulation starts at 4.2 AU and finishes at 1.3 AU with a step size in heliocentric distance of 0.1 AU. After giving a short discussion on 2 dimensional contour plots of important stages during perihelion approach the maximum of the cometary ion flux and of the magnetic field are presented as functions of heliocentric distance.

The simulation results allow to distinguish three different regimes in the global view. The test-particle regime covers a heliocentric distance between 4.2 AU to 3.7 AU. Weak

mass-loading of the solar wind leads to a moderate enhancement of the magnetic field which is localized in the vicinity of the nucleus and which reaches factors in the range 2.5 to 5 compared to the B_{imf}. In the Mach cone regime covering a heliocentric distance of 3.7 AU to about 2.7 AU the cometary ion flux exceeds the undisturbed solar wind ion flow leading to a stronger feedback on the solar wind parameters. The magnetic field exhibits an enhancement by a factor 7 and the enhancement is detaching from the nucleus surface. The last regime covers a distance of 2.7 AU to perihelion. Although, this regime shows strong effects on the plasma environment of the comet the absolute values of the magnetic field and the cometary ion flux appear to follow the growth process of the interplanetary magnetic field and of the solar wind ion flux as the comet approaches the Sun.

The 2 dimensional contour plots provide more information than the global 1 dimensional view. Therefore, the shock formation regime can be separated to the nonlinear Mach regime covering a range from 2.7 AU to 2 AU. The shock formation regime extends from 2 AU to perihelion.

The position of the bow shock along the Sun-comet line is compared with an analytical formula by Biermann et al. (1967) and Galeev et al. (1985) yielding good agreement. Rational law fits to the hybrid simulation data are also presented. Fits to the maximum of the cometary ion flux, the maximum of the magnetic field magnitude, and fits along the Sun-comet line to the magnetic pileup boundary, the ion composition boundary, and the bow shock position as function of heliocentric distance are discussed.

9 Solar wind-comet interaction with a water and CO coma

9.1 Introduction

In the preceding chapters, CG was assumed to consist only of a water dominated coma. The fact that the coma of comets is much more complicated was neglected to obtain a general picture on how the solar wind-comet interaction leads to the formation of the characteristic plasma structures. In this last chapter, the model is extended to simulate a nucleus with water and CO activity. These simulations are often referred to as multi-ion hybrid simulations.

Multi-ion simulations in hybrid plasma models were presented by Simon et al. (2007) which extended the model of Bagdonat and Motschmann (2002) to simulate the interaction between Titan's atmosphere with several ion species and the Saturnian magnetospheric plasma flow. As the spread in the mass ratio of the atmospheric ions were large a mass spectrometer was identified allowing to distinguish between ions of different mass. The underlying mechanism is based on the ion gyroradius depending on the ion mass. Multi-species calculations have also been presented by Bösswetter et al. (2009) in connection with hybrid plasma simulations of Mars.

There are, however, no studies of the plasma environment of comets available for a comet outgassing more than one species. Although, as discussed for comet Hale-Bopp in Chapter 4 or in Chapter 7 about coma anisotropies at comet CG the coma of comets is very complex consisting of several species some of which are originating directly from the nucleus while others are the products of a complex chemistry. The thermal modeling of comet CG has unveiled a crossing point between a CO dominated coma to a water dominated coma. This crossing point is depending on the employed simulation parameters between 3.5 AU and 4 AU along the preperihelion branch. It is thus important to simulate how an additional ion species is going to affect the plasma environment of comet CG. At 4.2 AU the CO outgassing is ten times stronger than water activity. The thermal model also showed that the CO outgassing strength is almost constant along the preperihelion branch. This strong CO activity should have an impact on the formation of certain plasma structures. In particular, the existence of the test particle regime has to be verified for this comet which might also have implications on the planning of the Rosetta mission once it reaches the comet.

Two aspects will be investigated. First, it will be discussed how the presence of CO affects the plasma environment of CG. Then, the plasma environment of CG with water and CO will be presented for a simulation starting at 4.2 AU and finishing at 3.5 AU with

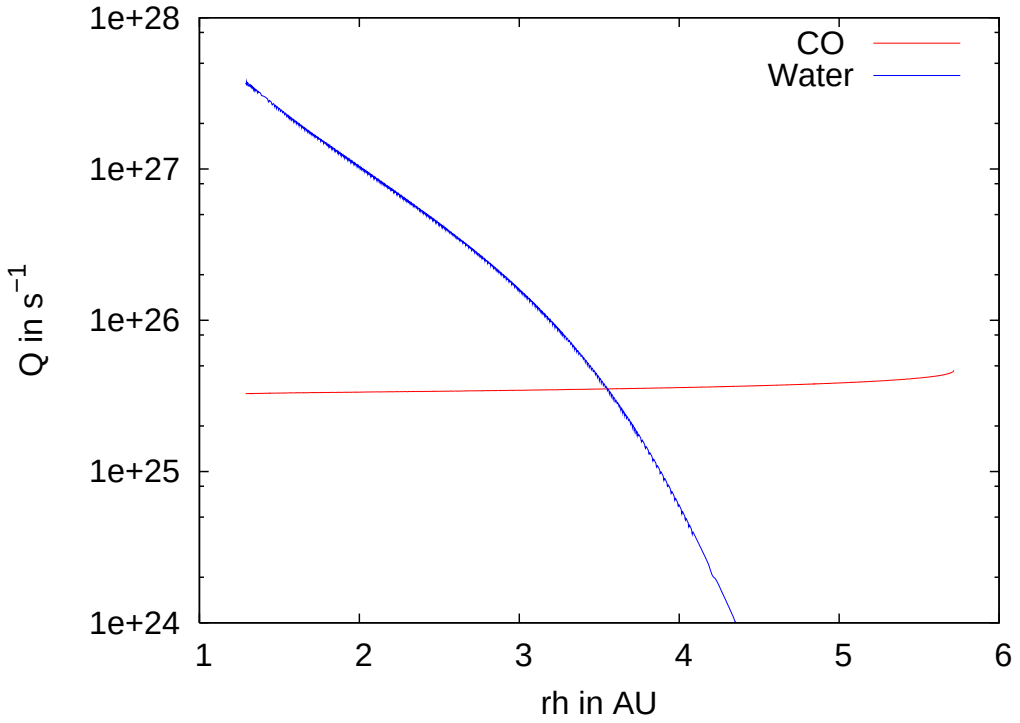

Figure 9.1: The water and CO activity as function of heliocentric distance along the preperihelion branch. At around 3.5 AU water activity exceeds CO. At 4.2 AU CO is more then an order of magnitude above the water activity.

a step size in heliocentric direction of 0.1 AU.

9.2 Implementation

The dynamics of the second ion species is simulated in analogy to the first ion species by the characteristics of the Vlasov equation given in Eq. (6.3). The same boundary conditions as in Section 7.4 have been used for this study. In the present simulation water and CO differ in their mass. All other quantities like charge, initial velocity, outgassing pattern, ionization rate are the same. These values can be found in Section 7.4. Perihelion approach is modeled as in the previous chapter. But the simulation is proceeded only to 3.5 AU as at this heliocentric distance water and CO activity are roughly the same. As shown in Fig. 9.1 the crossing point of the CO and water production curves are at 3.5 AU.

9.3 Results

Comet CG has an aphelion distance of 5.6 AU and a perihelion distance of 1.25 AU. At aphelion, water activity drops to values below 10^{24} s^{-1}. But already for such low water production rates previous investigations of the solar wind comet-interaction have shown that the solar wind is directly interacting with the surface of the nucleus. This regime was called test particle regime as the feedback of the very faint comet to the solar wind

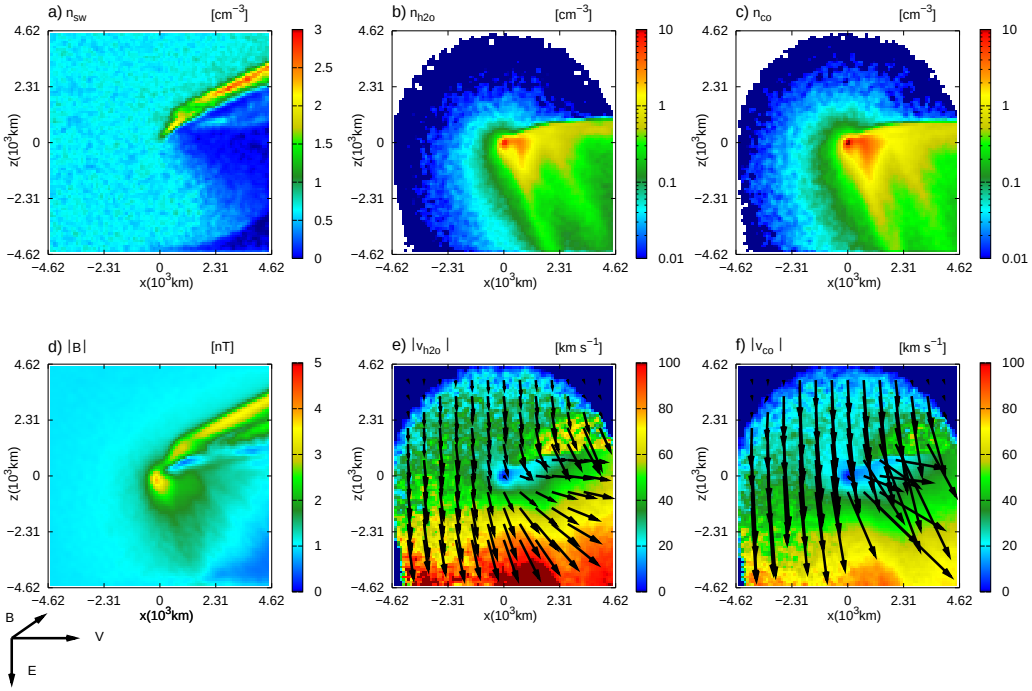

Figure 9.2: The solar wind-comet interaction with water and CO in the polar plane is shown at 3.5 AU. The solar wind ion density (a), the water ion density (b), the CO ion density (c), the magnetic field (d), the water ion bulk velocity (e), and the CO ion bulk velocity (f) are displayed. CO activity is as strong as water. CO leads to a quantitative enhancement of the magnetic field and the solar wind densities compared to simulations without CO as shown in Fig. 9.3. But qualitatively the plasma environment of CG has not changed. As CO is heavier than water the acceleration of CO ions leads to lower velocities as shown in f) compared to e). Small differences in the flow direction of the two cometary ion species are also discernible.

parameters is very low (Lipatov et al. 2002, Bagdonat and Motschmann 2002, Hansen et al. 2007, Coates and Jones 2009). In the previous chapter the test particle regime was identified at 4.2 AU. But in this simulation CO was neglected. The thermal modeling in Chapter 5 has shown that there is a cross point between a water dominated and a CO dominated coma. According to Fig. 9.1 this crossing point is at around 3.5 AU. Beyond this distance the nucleus is outgassing CO at a constant rate of 3×10^{25} s^{-1}. Therefore, CO activity exceeds water activity at 4.2 AU by more than an order of magnitude. For such high activity rates the plasma environment of CG could not be in the test particle regime.

9.3.1 Plasma environment with and without CO activity at 3.5 AU

The plasma environment of CG is simulated at 3.5 AU for two cases. In Fig. 9.2 is displayed the polar plane for a calculation with water and CO. For comparison, the same calculation with only water but the same total activity is shown in Fig. 9.3.

The solar wind density in the simulation with a CO plasma source depicted in Fig. 9.2a shows the linear Mach cone. The cone structure is very similar to the Mach cone

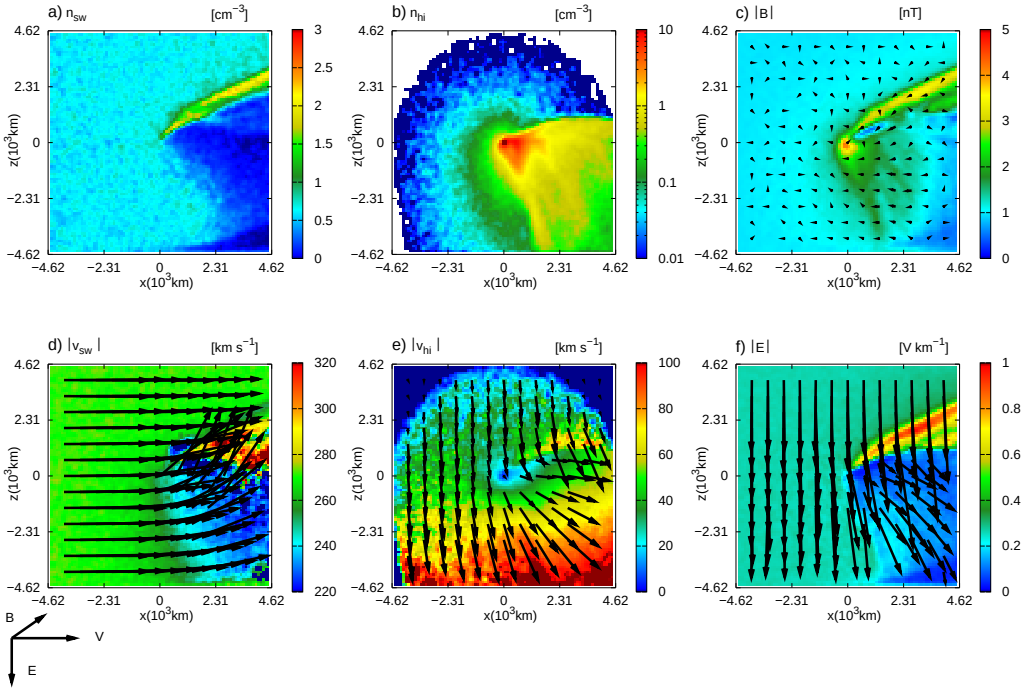

Figure 9.3: The solar wind-comet interaction in the polar plane is displayed without CO activity at 3.5 AU. The solar wind proton density (a), the cometary ion density (b), the magnetic field (c), the solar wind bulk velocity (d), the cometary ion bulk velocity (e), and the electric field (f) are displayed. The comet is in the regime of the linear Mach cone. The penetration of the cometary tail by the solar wind is getting weaker leading to a deflection of the incoming solar wind.

seen in the solution without CO which is displayed in Fig. 9.3a. The differences are mainly quantitative. The Mach cone appears to be enhanced by the presence of the CO species. It is broader and spatially larger than the Mach cone without CO shown in Fig. 9.2a and Fig. 9.3a, respectively. The pile-up of the magnetic field in front of the obstacle appears to be stronger in absolute values and in its spatial extensions in the solution with CO as shown in Fig. 9.2d compared to the solution without CO as displayed in Fig. 9.3c. The water ions shown in Fig. 9.2e reach higher velocities compared to the case without CO in Fig. 9.3e. But generally, the SW-C interaction with and without CO appears to be the same with small quantitative differences. As the mass ratio of CO to water ions is 1.6 the tail orientation of the two species is rather similar. This mass ratio is small compared to the ratio of Simon et al. (2007) which led to the conclusion that there must be a mass spectrometer due to the ion gyroradius depending on the ion mass. More pronounced are the differences in the bulk velocity displayed in Fig. 9.2e and f. The heavier CO ions reach lower velocities than the water ions. The predominant flow direction of the water ions is between 45 to 20° from the solar wind flow direction while the CO flow directions lies in the range 45 to 80°. Hence, the light species rotates faster in flow direction which is in good agreement with Simon et al. (2007).

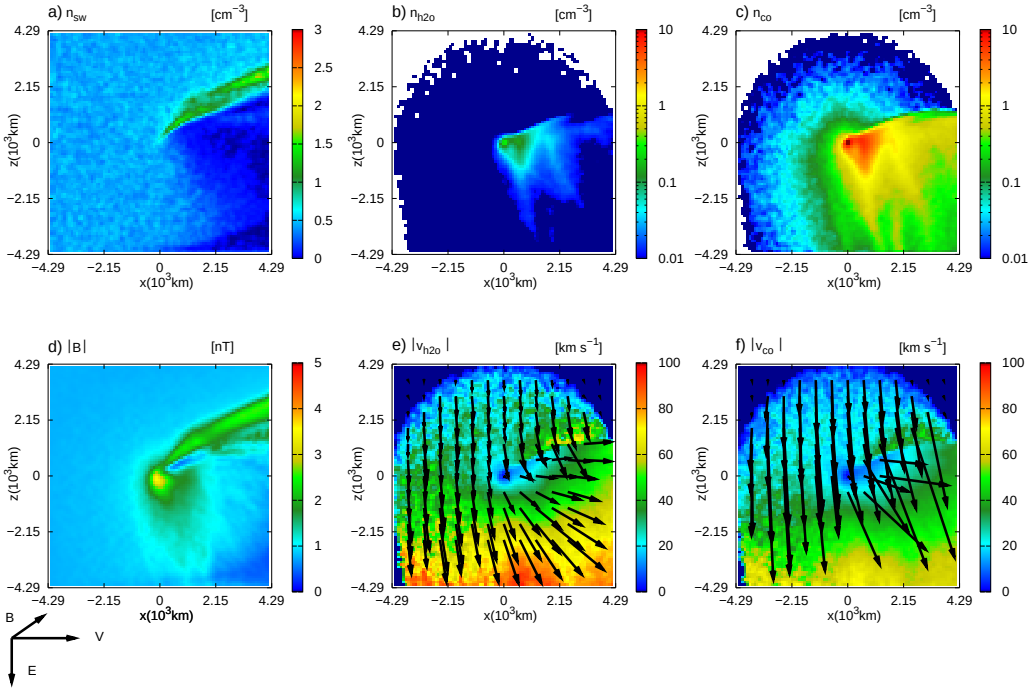

Figure 9.4: The solar wind-comet interaction with water and CO in the polar plane at 4.2 AU with the same quantities as Fig. 9.2. At 4.2 AU CO activity exceeds water by more than an order of magnitude reaching values of 3×10^{25} s^{-1}. The linear Mach cone is clearly discernible in the solar wind density a). The penetration of the tail by the solar wind is weaker than in Fig. 8.2a without CO. The magnetic field is enhanced in front of the obstacle. The situation is comparable to the linear Mach cone regime discussed in the previous Chapter for water between 3.7 AU and 2.7 AU. This result shows that there might be no test particle regime at comet CG.

9.3.2 Perihelion approach with CO and water activity from 4.2 to 3.5 AU

The perihelion approach of CG is simulated with water and CO activity. As in the simulation of Chapter 8 with a pure water ion coma the simulation is started at 4.2 AU. At this heliocentric position and beyond water activity is more than an order of magnitude below CO activity. The plasma environment beyond 4.2 AU should therefore be dominated by CO or even other volatile species. As the CO activity displayed in Fig. 9.1 along the preperihelion branch is constant the plasma environment beyond 4.2 AU should be similar to the results shown in Fig. 9.4 at 4.2 AU.

A striking difference of the plasma environment with CO compared to the solution without CO is the expansion of the interaction region. At 4.2 AU and without CO the simulation box is 1.2×10^3 km large as shown in Fig. 8.2. With CO the simulation box increases to 8.6×10^3 km which is a factor of 7 larger. The plasma environment of CG at 4.2 AU is dominated by the CO activity which is around 3.6×10^{25} s^{-1}. Compared to water activity CO exceeds it roughly by a factor of 40. The water ion tail is consequently very faint compared to the CO ion tail shown in Fig. 9.4b and c, respectively. The feedback

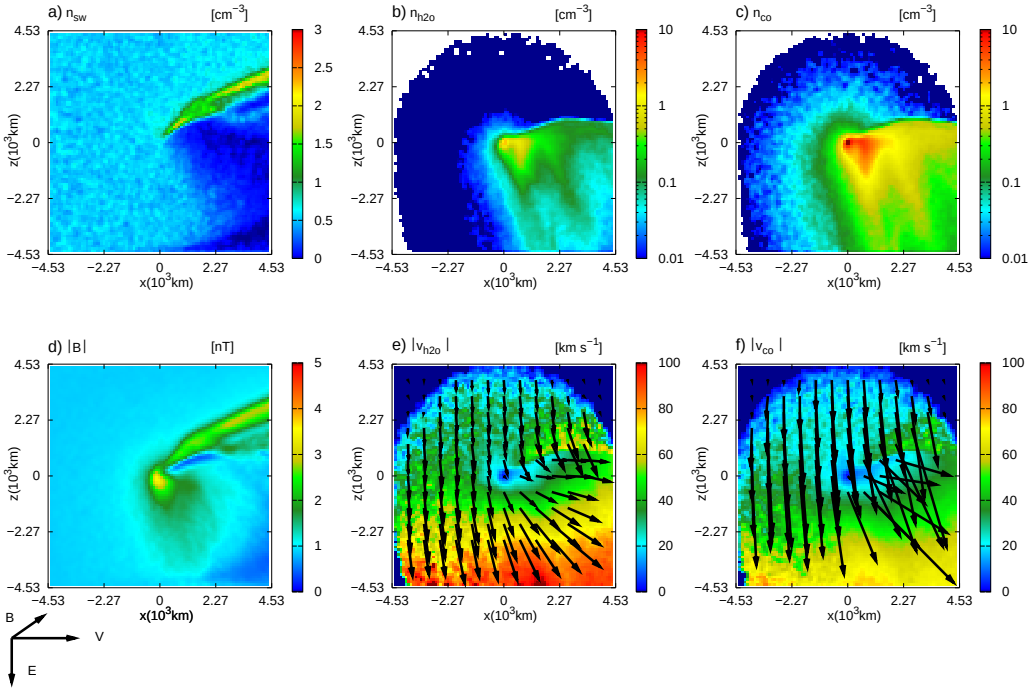

Figure 9.5: The solar wind-comet interaction with water and CO in the polar plane at 3.8 AU with the same quantities as Fig. 9.2. Water activity is getting stronger. But the plasma environment is still dominated by the CO activity as in Fig. 9.4. Only weak enhancements in the solar wind parameters are discernible.

to the solar wind parameters is in this calculation very strong compared to the results without CO shown in Fig. 8.2. A linear Mach cone is visible in the solar wind ion density depicted in Fig. 9.4a. The penetration of the cometary tail is much weaker than in the calculation without CO shown in Fig. 8.2. A pile-up of the magnetic field in front of the nucleus is shown in Fig. 9.4a which is very weak and confined in the immediate vicinity of the nucleus in the solution without CO of Fig. 8.2.

It thus can be concluded that with CO the plasma environment of CG at 4.2 AU exhibits a strong feedback by the CO coma. The comet is in the linear Mach cone regime. The test particle regime discussed in many articles should not be present at this comet if CG exhibits a CO activity as predicted by the thermal model of this thesis which has been successfully applied on the CO production rates of comet C/1995 O1 (Hale-Bopp). Of course, for other comets with larger aphelion positions and/or less volatile components the concept of the test particle regime should be still valid. But as this investigation has showed the contribution of super volatiles far from the Sun should not be neglected to obtain a more realistic picture of the plasma environment of comets.

As the comet approaches perihelion water activity increases while CO activity remains almost constant as shown in Fig. 9.1. Consequently, the feedback to the solar wind is getting stronger as water activity increases. At 3.8 AU from the Sun the linear Mach cone in the solar wind ion density is increasing with water activity as shown in Fig. 9.5a. Compared to the Mach cone at 4.2 AU the enhancement is moderate. The same conclusion can be drawn for the magnetic field. Although, water activity has increased by a factor of

7 at 3.8 AU compared to 4.2 AU. Therefore, the plasma environment is still dominated by the CO.

At a heliocentric position of 3.5 AU water activity is almost the same as CO. The feedback to the solar wind starts to get noticeably stronger. The linear Mach cone shown in Fig. 9.2 is enhanced further. The angle between the solar wind flow and the Mach cone is increasing. Also the magnetic pile-up is getting stronger. As CO activity remains constant it can be concluded that these reactions of the solar wind parameters are due to the water activity. Hence, based on the employed model parameters 3.5 AU marks the transition from a plasma environment that is dominated by CO activity to a regime in which water activity is dominant. With increasing water activity the plasma environment of the comet is converging to the pure water coma simulations presented in Chapter 8.

9.4 Summary

The evolution of the plasma environment of comet CG with water and CO activity is investigated as the comet approaches the Sun in the range from 4.2 AU to 3.5 AU. The plasma environment is calculated with the quasi-neutral, three dimensional hybrid plasma model while the thermal model presented in the first part of this thesis is used to calculate the water and CO activity.

A comparison of the plasma environment of CG with and without CO at 3.5 AU shows that a CO coma leads to a quantitative enhancement of the plasma structures but qualitatively the plasma environment remains the same. The linear Mach cone is enhanced as the heavier CO ions are not accelerated so strong as the water ions. The penetration of the cometary ion tail is weaker in the CO solution compared to a calculation without CO. The magnetic pile-up is stronger. As the mass ratio of CO to water is 1.6 the water tail and CO tail exhibit a similar orientation.

The plasma environment of CG is investigated over a heliocentric range from 4.2 AU to 3.5 AU with a step size in heliocentric distance of 0.1 AU. It is shown that at 4.2 AU CO activity is so strong that the comet is in the linear Mach cone regime. The interaction region is a factor of 7 larger in the solution with CO compared to the solution without CO. The test particle regime is not present for CG as CO activity is too strong. The transition from a CO dominated solar wind-comet interaction to a water dominated is found at 3.5 AU which correlated well with the crossing point between the water and CO production curves derived from thermal modeling.

The presented simulation results could be of great importance for ESA's Rosetta mission. They indicate a complex interaction regime even at a heliocentric distance of 4.2 AU in distinction to the test particle regime of a water dominated coma. The role of super volatile species like CO must be included in plasma simulation of comets far from the Sun to obtain a refined picture of the SW-C interaction.

10 Summary

10.1 Thermal model

In the first part of this thesis a thermal model devoted to the simulation of cometary activity is presented. The nucleus model accounts for heat conduction, heat advection, gas diffusion, sublimation, and condensation in an ice-dust matrix with moving boundaries. Surface erosion due to surface sublimation leads to a moving boundary which is resolved by applying a temperature remapping technique. This approach allows to take properly into account the loss in the internal energy of the eroded surface layers. Such moving boundary techniques are referred to as Stefan problems. The newly developed computer program is extendable and modular. New features can be easily incorporated. The code allows to switch on and off certain physical features, like Stefan problem, gas diffusion, CO bulk ice. The importance of the Stefan problem and gas diffusion on temperature depth profiles and activity has been investigated for a pure water ice sphere. It is shown that gas diffusion without the Stefan problem has a strong impact on temperature depth profiles but water activity at the surface is not much affected. The Stefan problem reduces the effect of gas diffusion considerably also for the temperature depth profiles.

The model is applied to interpret the water and CO production rates of comet C/1995 O1 (Hale-Bopp). The approach is guided by recent observational findings on important parameters controlling cometary activity. For the first time, a thermal model is applied to the full data set of water and CO production rates of comet Hale-Bopp covering a heliocentric range from -7 AU pre- to 15 AU postperihelion. For the first time, a thermal model without the assumption of amorphous ice with occluded CO gas is successfully applied to interpret the measured CO and water production rates of comet Hale-Bopp. The CO production curve fits the observations over the whole heliocentric distance starting at -7 AU to 15 AU very well. A low thermal conductivity of 0.01 W $K^{-1}m^{-1}$ is in good agreement with the Hale-Bopp observations.

After having successfully reproduced the production rates of comet Hale-Bopp for CO and water the thermal model is applied to predict the activity of ESA's Rosetta target comet 67P/Churyumov-Gerasimenko. Thermal flux, temperature depth profiles, and activity of water and CO are studied. The influence of the thermal conductivity as a key yet poorly constrained parameter has been studied. The importance of the Stefan problem is worked out in detailed. The loss of internal energy of the eroded surface layers leads to a much colder nucleus compared to a calculation in which this aspect is neglected. Strong differences in the thermal flux and temperature depth profiles are found at perihelion as surface sublimation and thus surface erosion reaches its peak value.

Activity of water is shrinked by the Stefan problem if the thermal conductivity is

large,e.g. 10^{-1} W m^{-1} K^{-1}. CO activity exhibits a characteristic asymmetry with an almost constant activity along the preperihelion branch, a peak at perihelion, and a smooth decline similar to the solar irradiation of the surface along the preperihelion branch. Such an asymmetry is not observed in the solution without the Stefan problem and it is pronounced for low thermal conductivities, e.g. 10^{-3} W K^{-1}m^{-1}. The Stefan problem brings the CO front close to the surface at perihelion while without it the CO front remains several tens of cm or meters below the surface. With increasing thermal conductivity the CO activity profile converges to a flat curve.

For low values of the thermal conductivity, Rosetta should measure a steep temperature gradient below an active area mainly near perihelion. Even at strong solar insolation the temperatures are extremely low directly below the surface since the cold CO front is located at a depth of only some centimeters. This would also mean that other volatiles and amorphous ice, if it does exist, are present near the surface and one could possibly find pristine matter in shallow depths.

The thermal model presented in this thesis is successful in the interpretation of the CO and water production rates of comet Hale-Bopp. Yet, there are many unresolved issues surrounding thermal modeling of comets. The most prominent aspect is the treatment of dust in the study of cometary activity as presented in this thesis. During the KOSI experiments at the DLR/Cologne activity subsided if a mixture of ice and dust is considered. In-situ images from comets revealed dust covered surfaces with only little ice covered areas (Keller et al. 1986a,b, Belton et al. 2007, Thomas et al. 2007) yet comets show a rather constant activity pattern for several apparitions (Schleicher 2006). How does dust influence the thermal evolution of comets? How is dust ejected from the surface of comets? How does dust exchange energy with gas and how does dust drag work? Other extensions of the model would include models of the shape and spin state of the nucleus. The model could be used to study inverse problems such as to derive surface properties from thermal spectra. It would also be important to work towards better boundary conditions for the gas diffusion model.

10.2 Hybrid plasma model

The plasma environment of comet CG is investigated with a quasi-neutral, three dimensional hybrid plasma model that treats the dynamics of the solar wind protons and cometary ions kinetically while the electrons are modeled as a charge neutralizing fluid that instantaneously adapts to the heavy ion dynamics. Results from the thermal modeling of comet CG are incorporated into the hybrid model to study different aspects of the solar wind-comet interaction.

The study of coma anisotropies has shown that the mass loading of the solar wind is strongly affected by the spatial distribution of the freshly born cometary ions. While the restriction of cometary activity to the Sun illuminated side has led to only quantitative modifications the confinement of cometary activity in a cone shaped model has unveiled also qualitative new features. The cone shaped model leads to an increasing degree of mixing between the solar wind protons and cometary ions. This opens an additional transport channel for the magnetic field so with increasing intensity the magnetic field can also be transported by the cometary species which leads to a broadening of the magnetic

barrier region. Second, the increasing degree of mixture between the species leads to an ion composition boundary which is only gradually developed. Third, it is found that the deceleration of the solar wind is much smoother than in the dayside restricted and spherically symmetric activity patterns.

The simulation of the perihelion approach of comet CG allows to distinguish three different regimes when considering the maximum cometary ion flux and the maximum magnetic field. For these quantities the test-particle regime covers a heliocentric distance between 4.2 AU to 3.7 AU. Weak mass-loading of the solar wind leads to a moderate enhancement of the magnetic field which is localized in the vicinity of the nucleus. In the Mach cone regime covering a heliocentric distance of 3.7 AU to about 2.7 AU the cometary ion flux exceeds the undisturbed solar wind ion flow leading to a stronger feedback, e.g. factor of 7, to the magnetic field strength. The last regime covers a distance of 2.7 AU to perihelion. This regime is the shock formation regime. At the end of this interval the solar wind and the cometary plasma are almost completely separated. The global view, however, does not reflect these processes so clearly. The absolute values of the magnetic field and the cometary ion flux appear to follow the growth process of the interplanetary magnetic field and of the solar wind ion flux as the comet approaches the Sun. The position of the bow shock along the Sun-comet line is compared with an analytical formula by Biermann et al. (1967) and Galeev et al. (1985) yielding good agreement.

In the last hybrid simulation, CO is included in the model. A comparison of the plasma environment of CG with and without CO shows that a CO coma leads to quantitative enhancement of the plasma structures. The plasma environment of CG is also investigated over a heliocentric range from 4.2 AU to 3.5 AU. It is shown that at 4.2 AU CO activity is so strong that the comet is in the linear Mach cone regime. The test-particle regime is not present for CG as CO activity is too strong. The transition from a CO dominated solar wind-comet interaction to a water dominated is found at 3.5 AU which correlates well with the crossing point between the water and CO production curves derived from thermal modeling.

The presented simulation results could be of great importance for ESA's Rosetta mission. They indicate a complex interaction regime even at a heliocentric distance of 4.2 AU in distinction to the test particle regime of a water dominated coma. The role of super volatile species like CO must be included in plasma simulation of comets far from the Sun to obtain a refined picture of the SW-C interaction.

Danksagung

Die vorliegende Arbeit wurde am Deutschen Zentrum für Luft- und Raumfahrt (DLR) in Berlin angefertigt. Dem Vorstand des DLR sei für die Bewilligung der finanziellen Mittel für dieses Promotionsvorhaben herzlich gedankt.

Mein besonderer Dank gilt Herrn Dr. Ekkehard Kührt für die Übertragung der Arbeit, für seine persönliche Unterstützung und für viele Anregungen und Diskussionen, die der Arbeit wichtige Impulse gegeben haben. Für die Möglichkeit an zahlreiche Konferenzen teilzunehmen sei herzlich gedankt.

Mein besonderer Dank gilt Herrn Prof. Uwe Motschmann für die Begleitung der Arbeit als Mentor. Die Arbeit hat in jeder Hinsicht von den vielen Diskussionen mit Herrn Motschmann profitiert. Sein fachliches Wissen, seine stete Unterstützung und seine Zuverlässigkeit haben einen bleibenden Eindruck hinterlassen. Für die Möglichkeit am ISSI Comet Modeling Team mitwirken zu können, möchte ich mich herzlich bedanken.

Herrn Priv. Dr. Horst-Uwe Keller möchte ich für die vielen Diskussionen zur Oberflächenerosion und zu Kometen allgemein herzlich danken. Unvergessen wird die Fahrt zum Atlas V Start bleiben.

Herrn Prof. Karl-Heinz Glaßmeier möchte ich für das Koreferat und seine Denkanstöße zur Perihelannäherung herzlich danken.

Herrn Prof. Jürgen Blum möchte ich für seine Bereitschaft den Vorsitz der Prüfungskommission zu übernehmen herzlich danken.

Herrn Dr. B. Davidsson, Herrn Prof. H. Rickman und Herrn Dr. U. Skorov sei für viele Gespräche zur thermischen Modellierung von Kometen gedankt.

Mein Dank gilt A. Schmidt für die Bereitstellung von Rechenzeit bei der ESAC.

Dem ISSI Comet Modeling Team sei gedankt für viele Diskussionen zur Modellierung von Kometen.

Bei meinen Kollegen am Deutschen Zentrum für Luft- und Raumfahrt möchte ich mich für die schöne Zeit herzlich bedanken. Den Kollegen der Arbeitsgruppe von Prof. Motschmann an der TU Braunschweig gilt mein besonderer Dank für die gute Zusammenarbeit.

Ein Dank sei auch an die Open Source Bewegung gerichtet, die viele der Werkzeuge bereitgestellt hat, die für die Durchführung dieser Arbeit maßgeblich waren.

Bibliography

Ahearn, M. F., 1982, Spectrophotometry of comets at optical wavelengths, in IAU Colloq. 61: Comet Discoveries, Statistics, and Observational Selection, (Ed.) L. L. Wilkening, pp. 433–460

Axford, W. I., 1962, The Interaction between the Solar Wind and the Earth's Magnetosphere, J. Geophys. Res., 67, 3791–3796

Bagdonat, T., 2005, Hybrid Simulation of Weak Comets, Copernicus Verlag

Bagdonat, T., Motschmann, U., 2002, 3d hybrid simulation code using curvilinear coordinates, J. Comp. Phys., 183, 470 – 485, ISSN 0021-9991

Bagdonat, T., Motschmann, U., 2002, From a Weak to a Strong Comet - 3d Global Hybrid Simulation Studies, Earth Moon and Planets, 90, 305–321

Bar-Nun, A., Laufer, D., 2003, First experimental studies of large samples of gas-laden amorphous "cometary" ices, Icarus, 161, 157–163

Bar-Nun, A., Pat-El, I., Laufer, D., 2007, Comparison between the findings of Deep Impact and our experimental results on large samples of gas-laden amorphous ice, Icarus, 187, 321–325

Bate, R. R., Mueller, D. D., White, J. E., 1971, Fundamentals of astodynamics, Dover Publications, New York

Belton, M. J., Thomas, P., Veverka, J., Schultz, P., A'Hearn, M. F., Feaga, L., Farnham, T., Groussin, O., Li, J.-Y., Lisse, C., McFadden, L., Sunshine, J., Meech, K. J., Delamere, W. A., Kissel, J., 2007, The internal structure of Jupiter family cometary nuclei from Deep Impact observations:The "talps" or "layered pile" model, Icarus, 191, 573 – 585, ISSN 0019-1035

Benkhoff, J., Huebner, W. F., 1995, Influence of the vapor flux on temperature, density, and abundance distributions in a multicomponent, porous, icy body, Icarus, 114, 348–354

Benkhoff, J., Spohn, T., 1991, Results of a coupled heat and mass transfer model applied to KOSI sublimation experiments, in Theoretical Modelling of Comet Simulation Experiments, (Ed.) N. I. Kömle, S. J. Bauer, & T. Spohn, pp. 31–+

Benna, M., Mahaffy, P. R., 2006, New multi-fluid MHD model of comet 26P/Grigg-Skjellerup: Extrapolation to comet 67P/Churyumov-Gerasimenko, Geophys. Res. Lett., 33, 10 103–+

Biermann, L., 1951, Kometenschweife und solare Korpuskularstrahlung, Zeitschrift für Astrophysik, 29, 274–+

Biermann, L., Brosowski, B., Schmidt, H. U., 1967, The interactions of the solar wind with a comet, Solar Physics, 1, 254–284

Birdsall, C. K., Fuss, D., 1969, Clouds-in-clouds, clouds-in-cells physics for many-body plasma simulation, J. of Comp. Phys., 3, 494 – 511, ISSN 0021-9991

Birdsall, C. K., Langdon, A. B., 1985, Plasma physics via computer simulation, McGraw-Hill Book Company, Singapore

Biver, N., Bockelée-Morvan, D., Colom, P., Crovisier, J., Germain, B., Lellouch, E., Davies, J. K., Dent, W. R. F., Moreno, R., Paubert, G., Wink, J., Despois, D., Lis, D. C., Mehringer, D., Benford, D., Gardner, M., Phillips, T. G., Gunnarsson, M., Rickman, H., Winnberg, A., Bergman, P., Johansson, L. E. B., Rauer, H., 1997, Long-term Evolution of the Outgassing of Comet Hale-Bopp From Radio Observations, Earth Moon and Planets, 78, 5–11

Biver, N., Bockelée-Morvan, D., Colom, P., Crovisier, J., Henry, F., Lellouch, E., Winnberg, A., Johansson, L. E. B., Gunnarsson, M., Rickman, H., Rantakyrö, F., Davies, J. K., Dent, W. R. F., Paubert, G., Moreno, R., Wink, J., Despois, D., Benford, D. J., Gardner, M., Lis, D. C., Mehringer, D., Phillips, T. G., Rauer, H., 2002, The 1995 2002 Long-Term Monitoring of Comet C/1995 O1 (HALE BOPP) at Radio Wavelength, Earth Moon and Planets, 90, 5–14

Blake, D., Allamandola, L., Sandford, S., Hudgins, D., Freund, F., 1991, Clathrate hydrate formation in amorphous cometary ice analogs in vacuo, Science, 254, 548–551

Blum, J., Wurm, G., 2008, The Growth Mechanisms of Macroscopic Bodies in Protoplanetary Disks, Ann. Rev. of Astron. and Astrophys., 46, 21–56

Bockelée-Morvan, D., Rickman, H., 1997, C/1995 O1 (Hale-Bopp): Gas Production Curves And Their Interpretation, Earth Moon and Planets, 79, 55–77

Bockelée-Morvan, D., Moreno, R., Biver, N., Crovisier, J., Crifo, J., Fulle, M., Grewing, M., 2004, CO and dust productions in 67P/Churyumov-Gerasimenko at 3 AU post-perihelion, in The New Rosetta Targets. Observations, Simulations and Instrument Performances, (Ed.) L. Colangeli, E. Mazzotta Epifani, & P. Palumbo, vol. 311 of Astrophysics and Space Science Library, pp. 25–+

Bockelée-Morvan, D., Henry, F., Biver, N., Boissier, J., Colom, P., Crovisier, J., Despois, D., Moreno, R., Wink, J., 2009, Interferometric imaging of carbon monoxide in comet C/1995 O1 (Hale-Bopp): evidence of a strong rotating jet, Astron. Astrophys., 505, 825–843

Bogdanov, A., Sauer, K., Baumgärtel, K., Srivastava, K., 1996, Plasma structures at weakly outgassing comets-results from bi-ion fluid analysis, Planet. Space. Sci., 44, 519–528

Bösswetter, A., Bagdonat, T., Motschmann, U., Sauer, K., 2004, Plasma boundaries at mars: a 3-d simulation study, Annales Geophysicae, 22, 4363–4379, ISSN 0992-7689

Bösswetter, A., Auster, U., Richter, I., Fränz, M., Langlais, B., McKenna-Lawlor, S., Simon, S., Motschmann, U., Glassmeier, K. H., Edberg, N. J. T., Lundin, R., 2009, Rosetta swing-by at Mars - an analysis of the ROMAP measurements in comparison with results of 3-D multi-ion hybrid simulations and MEX/ASPERA-3 data, Annales Geophysicae, 27, 2383–2398

Burchell, M. J., Kearsley, A. T., 2009, Short-period Jupiter family comets after Stardust, Planet. Space. Sci., 57, 1146–1161

Cap, F., 1970, Einführung in die Plasmaphysik I, Akademie Verlag, Berlin

Capria, M. T., Capaccioni, F., Coradini, A., de Sanctis, M. C., Espinasse, S., Federico, C., Orosei, R., Salomone, M., 1996, A P/Wirtanen evolution model, Planet. Space. Sci., 44, 987–1000

Capria, M. T., Coradini, A., De Sanctis, M. C., Orosei, R., 2000, CO emission mechanisms in C/1995 O1 (Hale-Bopp), Astron. Astrophys., 357, 359–366

Capria, M. T., Coradini, A., De Sanctis, M. C., Blecka, M. I., 2001, P/Wirtanen thermal evolution: effects due to the presence of an organic component in the refractory material, Planet. Space. Sci., 49, 907–918

Capria, M. T., Coradini, A., De Sanctis, M. C., 2002, C/1995 O1 Hale-Bopp: Short and Long Distance activity from a Theoretical Model, Earth Moon and Planets, 90, 217–225

Charnley, S. B., Rodgers, S. D., 2008, Interstellar Reservoirs of Cometary Matter, Space Sci. Rev., 138, 59–73

Coates, A. J., 1997, Ionospheres and magnetospheres of comets, Advances in Space Research, 20, 255–+

Coates, A. J., Jones, G. H., 2009, Plasma environment of Jupiter family comets, Planet. Space. Sci., 57, 1175–1191

Coates, A. J., Johnstone, A. D., Wilken, B., Neubauer, F. M., 1993, Velocity space diffusion and nongyrotropy of pickup water group ions at comet Grigg-Skjellerup, J. Geophys. Res., 98, 20 985–+

Cochran, A. L., 1985, A re-evaluation of the Haser model scale lengths for comets, The Astron. J., 90, 2609–2614

Colom, P., Gérard, E., Crovisier, J., Bockelé-Morvan, D., Biver, N., Rauer, H., 1997, Observations of the OH Radical in Comet C/1995 O1 (Hale-Bopp) with the Nançay Radio Telescope, Earth Moon and Planets, 78, 37–43

Combi, M. R., 1996, Time-Dependent Gas Kinetics in Tenuous Planetary Atmospheres: The Cometary Coma, Icarus, 123, 207–226

Combi, M. R., Smyth, W. H., 1988, Monte Carlo Particle Trajectory Models for Neutral Cometary Gases. II. The Spatial Morphology of the Lyman-Alpha Coma, Astrophys. J., 327, 1044–+

Combi, M. R., Harris, W. M., Smyth, W. H., 2004, Gas dynamics and kinetics in the cometary coma: theory and observations, in Comets II, (Ed.) Festou, M. C., Keller, H. U., & Weaver, H. A., pp. 523–552, University of Arizona Press, Tucson

Cottin, H., Gazeau, M. C., Benilan, Y., Raulin, F., 2001, Polyoxymethylene as Parent Molecule for the Formaldehyde Extended Source in Comet Halley, Astrophys. J., 556, 417–420

Crank, J., 1984, Free and moving boundary problems, Oxford University Press, Oxford New York Toronto

Crank, J., Gupta, R. S., 1972, A method for solving moving boundary problems in heat flow using cubic splines or polynomials, J. Inst. Math. Appl., 10, 296–304

Crovisier, J., Leech, K., Bockelée-Morvan, D., Lellouch, E., Brooke, T. Y., Hanner, M. S., Altieri, B., Keller, H. U., Lim, T., 1999, The Spectrum of Comet Hale-Bopp as seen by ISO, in The Universe as Seen by ISO, (Ed.) P. Cox & M. Kessler, vol. 427 of ESA Special Publication, pp. 137–+

Crovisier, J., Colom, P., Gérard, E., Bockelée-Morvan, D., Bourgois, G., 2002, Observations at Nançay of the OH 18-cm lines in comets. The data base. Observations made from 1982 to 1999, Astron. Astrophys., 393, 1053–1064

Davidsson, B. J. R., Gutiérrez, P. J., 2005, Nucleus properties of Comet 67P/Churyumov Gerasimenko estimated from non-gravitational force modeling, Icarus, 176, 453–477

Davidsson, B. J. R., Skorov, Y. V., 2002, On the Light-Absorbing Surface Layer of Cometary Nuclei II. Thermal Modeling, Icarus, 159, 239–258

Davidsson, B. J. R., Skorov, Y. V., 2004, A practical tool for simulating the presence of gas comae in thermophysical modeling of cometary nuclei, Icarus, 168, 163–185

Davidsson, B. J. R., Gutiérrez, P. J., Rickman, H., 2009, Physical properties of morphological units on Comet 9P/Tempel 1 derived from near-IR Deep Impact spectra, Icarus, 201, 335–357

de Sanctis, M. C., Capaccioni, F., Capria, M. T., Coradini, A., Federico, C., Orosei, R., Salomone, M., 1999, Models of P/Wirtanen nucleus: active regions versus non-active regions, Planet. Space. Sci., 47, 855–872

de Sanctis, M. C., Capria, M. T., Coradini, A., 2006, 67P/Churyumov Gerasimenko nucleus model: Portrayal of the Rosetta target, Adv. in Space Res., 38, 1906–1910

Delamere, P. A., 2006, Hybrid code simulations of the solar wind interaction with Comet 19P/Borrelly, J. Geophys. Res., 111, 12 217–+

Disanti, M. A., Mumma, M. J., Russo, N. D., Magee-Sauer, K., Novak, R., Rettig, T. W., 1999, Identification of two sources of carbon monoxide in comet Hale-Bopp, Nature, 399, 662–665

Disanti, M. A., Mumma, M. J., Dello Russo, N., Magee-Sauer, K., 2001, Carbon Monoxide Production and Excitation in Comet C/1995 O1 (Hale-Bopp): Isolation of Native and Distributed CO Sources, Icarus, 153, 361–390

Douglas, J., Gallie, T. M., 1955, On the numerical integration of a parabolic differential equation subject to a moving boundary condition, Duke Math. J., 22, 557–570

Duncan, M. J., 2008, Dynamical Origin of Comets and Their Reservoirs, Space Sci. Rev., 138, 109–126

Eastwood, J. W., Arter, W., Brealey, N. J., Hockney, R. W., 1995, Body-fitted electromagnetic pic software for use on parallel computers, Computer Physics Communications, 87, 155 – 178, ISSN 0010-4655, particle Simulation Methods

Eberhardt, P., Krankowsky, D., Schulte, W., Dolder, U., Lammerzahl, P., Berthelier, J. J., Woweries, J., Stubbemann, U., Hodges, R. R., Hoffman, J. H., Illiano, J. M., 1987, To Co/ and n2 Abundance in Comet p/ Halley, Astron. Astrophys., 187, 481–+

Enzian, A., 1999, On the Prediction of CO Outgassing from Comets Hale-Bopp and Wirtanen, Space Sci. Rev., 90, 131–139

Enzian, A., Cabot, H., Klinger, J., 1997, A 2 1/2 D thermodynamic model of cometary nuclei. I. Application to the activity of comet 29P/Schwassmann-Wachmann 1., Astron. Astrophys., 319, 995–1006

Enzian, A., Cabot, H., Klinger, J., 1998, Simulation of the water and carbon monoxide production rates of comet Hale-Bopp using a quasi 3-D nucleus model, Planet. Space. Sci., 46, 851–858

Espinasse, S., Klinger, J., Ritz, C., Schmitt, B., 1991, Modeling of the thermal behavior and of the chemical differentiation of cometary nuclei, Icarus, 92, 350–365

Fanale, F. P., Salvail, J. R., 1984, An idealized short-period comet model - Surface insolation, H2O flux, dust flux, and mantle evolution, Icarus, 60, 476–511

Feaga, L. M., A'Hearn, M. F., Sunshine, J. M., Groussin, O., Farnham, T. L., 2007, Asymmetries in the distribution of H_2O and CO_2 in the inner coma of Comet 9P/Tempel 1 as observed by Deep Impact, Icarus, 191, 134–145

Feldman, P. D., Weaver, H. A., Festou, M. C., 1984, The ultraviolet spectrum of periodic Comet Encke (1980 XI), Icarus, 60, 455–463

Fernández, J. A., 2007, Origin of Comet Nuclei and Dynamics, Space Sci. Rev., 138, 27–42

Fernández, Y. R., 2002, The Nucleus of Comet Hale-Bopp (C/1995 O1): Size and Activity, Earth Moon and Planets, 89, 3–25

Festou, M. C., Barale, O., 2000, The Asymmetric Coma of Comets. I. Asymmetric Outgassing from the Nucleus of Comet 2P/Encke, The Astron. J., 119, 3119–3132

Flammer, K. R., Mendis, D. A., Houpis, H. L. F., 1998, On the Outgassing Profile of Comet Hale-Bopp, Astrophys. J., 494, 822–+

Friedrich, H., Pietschmann, F., 2010, Numerische Methoden, de Gruyter, Berlin

Galeev, A. A., Cravens, T. E., Gombosi, T. I., 1985, Solar wind stagnation near comets, Astrophys. J., 289, 807–819

Glassmeier, K., Motschmann, U., Mazelle, C., Neubauer, F. M., Sauer, K., Fuselier, S. A., Acuna, M. H., 1993, Mirror modes and fast magnetoacoustic waves near the magnetic pileup boundary of comet P/Halley, J. Geophys. Res., 98, 20 955–+

Glassmeier, K., Boehnhardt, H., Koschny, D., Kührt, E., Richter, I., 2007, The Rosetta Mission: Flying Towards the Origin of the Solar System, Space Sci. Rev., 128, 1–21

Gombosi, T. I., De Zeeuw, D. L., Häberli, R. M., Powell, K. G., 1996, Three-dimensional multiscale MHD model of cometary plasma environments, J. Geophys. Res., 101, 15 233–15 252

Gortsas, N., Kührt, E., Motschmann, U., Keller, H. U., 2007, New Thermal Model of the Sub-Surface Layer of Comets, in Bulletin of the American Astronomical Society, vol. 38 of Bulletin of the American Astronomical Society, pp. 498–+

Gortsas, N., Kührt, E., Motschmann, U., 2008, Numerical Studies of Surface Erosion in a Multi-Component Comet Nucleus, LPI Contributions, 1405, 8220–+

Gortsas, N., Motschmann, U., Kührt, E., Knollenberg, J., Simon, S., Boesswetter, A., 2009, Mapping of coma anisotropies to plasma structures of weak comets: a 3-d hybrid simulation study, Annales Geophysicae, 27, 1555–1572, ISSN 0992-7689

Gortsas, N., Kührt, E., Motschmann, U., Keller, H. U., 2010a, Thermal model of water and CO activity of C/1995 O1 (Hale-Bopp), submitted to Icarus

Gortsas, N., Motschmann, U., Kührt, E., Glassmeier, K., Hansen, K., Müller, J., Schmidt, A., 2010b, Global plasma parameter simulation of comet 67P/Churyumov-Gerasimenko approaching the Sun, submitted to Astron. & Astrophys.

Groussin, O., A'Hearn, M. F., Li, J., Thomas, P. C., Sunshine, J. M., Lisse, C. M., Meech, K. J., Farnham, T. L., Feaga, L. M., Delamere, W. A., 2007, Surface temperature of the nucleus of Comet 9P/Tempel 1, Icarus, 187, 16–25

Grün, E., Gebhard, J., Bar-Nun, A., Benkhoff, J., Dueren, H., Eich, G., Hische, R., Huebner, W. F., Keller, H. U., Klees, G., 1993, Development of a dust mantle on the surface of an insolated ice-dust mixture - Results from the KOSI-9 experiment, J. Geophys. Res., 98, 15 091–+

Haerendel, G., Paschmann, G., Baumjohann, W., Carlson, C. W., 1986, Dynamics of the AMPTE artificial comet, Nature, 320, 720–723

Hanner, M. S., Tedesco, E., Tokunaga, A. T., Veeder, G. J., Lester, D. F., Witteborn, F. C., Bregman, J. D., Gradie, J., Lebofsky, L., 1985, The dust coma of periodic Comet Churyumov-Gerasimenko (1982 VIII), Icarus, 64, 11–19

Hansen, K. C., Bagdonat, T., Motschmann, U., Alexander, C., Combi, M. R., Cravens, T. E., Gombosi, T. I., Jia, Y., Robertson, I. P., 2007, The Plasma Environment of Comet 67P/Churyumov-Gerasimenko Throughout the Rosetta Main Mission, Space Sci. Rev., 128, 133–166

Haser, L., 1957, Distribution d'intensite dans la tete d'une comete, Bulletin de la Societe Royale des Sciences de Liege, 43, 740–750

Hirsch, C., 1991, Numerical computation of internal and external flows, John Wiley & Sons Ltd.

Hoppe, P., 2007, Reservoir for Comet Material: Circumstellar Grains, Space Sci. Rev., 138, 43–57

Huddleston, D. E., Coates, A. J., Johnstone, A. D., 1992, Predictions of the solar wind interaction with Comet Grigg-Skjellerup, Geophys. Res. Lett., 19, 837–840

Huebner, W. F., 2008, Origins of Cometary Materials, Space Sci. Rev., 138, 5–25

Huebner, W. F., Markiewicz, W. J., 2000, The temperature and bulk flow speed of a gas effusing or evaporating from a surface into a void after reestablishment of collisional equilibrium, Icarus, 148, 594 – 596, ISSN 0019-1035

Huebner, W. F., Keady, J. J., Lyon, S. P., 1992, Solar photo rates for planetary atmospheres and atmospheric pollutants, Astrophys. and Space Sci., 195, 1–289

Huebner, W. F., Benkhoff, J., Capria, M. T., Coradini, A., de Sanctis, M. C., Enzian, A., Orosei, R., Prialnik, D., 1999, Results from the Comet Nucleus Model Team at the International Space Science Institute, Bern, Switzerland, Advances in Space Research, 23, 1283–1298

Huebner, W. F., Benkhoff, J., Capria, M., Coradini, A., de Sanctis, C., Orosei, R., Prialnik, D. (Eds.), 2006, Heat and Gas Diffusion in Comet Nuclei

Ip, W., Axford, W. I., 1982, Theories of physical processes in the cometary comae and ion tails, in IAU Colloq. 61: Comet Discoveries, Statistics, and Observational Selection, (Ed.) L. L. Wilkening, pp. 588–634

Irvine, W. M., Bergin, E. A., Dickens, J. E., Jewitt, D., Lovell, A. J., Matthews, H. E., Schloerb, F. P., Senay, M., 1998, Chemical processing in the coma as the source of cometary HNC, Nature, 393, 547–550

Israelevich, P. L., Gombosi, T. I., Ershkovich, A. I., DeZeeuw, D. L., Neubauer, F. M., Powell, K. G., 1999, The induced magnetosphere of comet Halley 4. Comparison of in situ observations and numerical simulations, J. Geophys. Res., 104, 28 309–28 320

Jewitt, D., Senay, M., Matthews, H., 1996, Observations of Carbon Monoxide in Comet Hale-Bopp, Science, 271, 1110–1113

Jia, Y. D., Combi, M. R., Hansen, K. C., Gombosi, T. I., Crary, F. J., Young, D. T., 2008, A 3-D global MHD model for the effect of neutral jets during the Deep Space 1 Comet 19P/Borrelly flyby, Icarus, 196, 249–257

Jorda, L., Rembor, K., Lecacheux, J., Colom, P., Colas, F., Frappa, E., Lara, L. M., 1997, The Rotational Parameters Of Hale-Bopp (C/1995 O1) From Observations Of The Dust Jets At PIC DU Midi Observatory, Earth Moon and Planets, 77, 167–180

Julian, W. H., Samarasinha, N. H., Belton, M. J. S., 2000, Thermal Structure of Cometary Active Regions: Comet 1P/Halley, Icarus, 144, 160–171

Kamoun, P., Campbell, D., Pettengill, G., Shapiro, I., 1998, Radar observations of three comets and detection of echoes from one: P/Grigg-Skjellerup, Planet. Space. Sci., 47, 23–28

Keller, H. U., Arpigny, C., Barbieri, C., Bonnet, R. M., Cazes, S., Coradini, M., Cosmovici, C. B., Delamere, W. A., Huebner, W. F., Hughes, D. W., Jamar, C., Malaise, D., Reitsema, H. J., Schmidt, H. U., Schmidt, W. K. H., Seige, P., Whipple, F. L., Wilhelm, K., 1986a, First Halley multicolour camera imaging results from Giotto, Nature, 321, 320–326

Keller, H. U., Delamere, W. A., Huebner, W. F., Reitsema, H., Schmidt, H. U., Schmidt, W. K. H., Whipple, F. L., Wilhelm, K., 1986b, Dust activity of Comet Halley's nucleus, in ESLAB Symposium on the Exploration of Halley's Comet, (Ed.) B. Battrick, E. J. Rolfe, & R. Reinhard, vol. 250 of ESA Special Publication, pp. 359–362

Klinger, J., 1981, Some consequences of a phase transition of water ice on the heat balance of comet nuclei, Icarus, 47, 320–324

Kossacki, K. J., Koemle, N. I., Kargl, G., Steiner, G., 1994, The influence of grain sintering on the thermoconductivity of porous ice, Planet. Space. Sci., 42, 383–389

Kossacki, K. J., Komle, N. I., Leliwa-Kopystynski, J., Kargl, G., 1997, Laboratory Investigation of the Evolution of Cometary Analogs: Results and Interpretation, Icarus, 128, 127–144

Kossacki, K. J., Szutowicz, S. Ł., Leliwa-Kopystyński, J., 1999, Comet 46P/Wirtanen: Evolution of the Subsurface Layer, Icarus, 142, 202–218

Krankowsky, D., Lammerzahl, P., Herrwerth, I., Woweries, J., Eberhardt, P., Dolder, U., Herrmann, U., Schulte, W., Berthelier, J. J., Illiano, J. M., Hodges, R. R., Hoffman, J. H., 1986, In situ gas and ion measurements at comet Halley, Nature, 321, 326–329

Kührt, E., 1984, Temperature profiles and thermal stresses in cometary nuclei, Icarus, 60, 512–521

Kührt, E., 1999, H2O-Activity of Comet Hale-Bopp, Space Sci. Rev., 90, 75–82

Kührt, E., Keller, H. U., 1994, The formation of cometary surface crusts, Icarus, 109, 121–132

Lamy, P. L., Toth, I., Davidsson, B. J. R., Groussin, O., Gutiérrez, P., Jorda, L., Kaasalainen, M., Lowry, S. C., 2007, A Portrait of the Nucleus of Comet 67P/Churyumov-Gerasimenko, Space Sci. Rev., 128, 23–66

Laufer, D., Pat-El, I., Bar-Nun, A., 2005, Experimental simulation of the formation of non-circular active depressions on Comet Wild-2 and of ice grain ejection from cometary surfaces, Icarus, 178, 248–252

Lederer, S. M., Campins, H., 2002, Evidence for Chemical Heterogeneity in the Nucleus of C/1995 O1 (Hale-Bopp), Earth Moon and Planets, 90, 381–389

Lederer, S. M., Campins, H., Osip, D. J., 2009, Chemical and physical properties of gas jets in comets. II. Modeling OH, CN and C_2 jets in Comet C/1995 O1 (Hale Bopp) one month after perihelion, Icarus, 199, 484–504

Lipatov, A. S., Motschmann, U., Bagdonat, T., 2002, 3D hybrid simulations of the interaction of the solar wind with a weak comet, Planet. Space. Sci., 50, 403–411

Mäkinen, J. T. T., 2004, Water production rate of comet 67P/Churyumov-Gerasimenko, in The New Rosetta Targets. Observations, Simulations and Instrument Performances, (Ed.) L. Colangeli, E. Mazzotta Epifani, & P. Palumbo, vol. 311 of Astrophysics and Space Science Library, pp. 61–+

Matthews, A. P., 1994, Current advance method and cyclic leapfrog for 2d multispecies hybrid plasma simulations, Journal of Computational Physics, 112, 102 – 116, ISSN 0021-9991

Mekler, Y., Prialnik, D., Podolak, M., 1990, Evaporation from a porous cometary nucleus, Astrophys. J., 356, 682–686

Mendis, D. A., Flammer, K. R., 1984, The multiple modes of interaction of the solar wind with a comet as it approaches the sun, Earth Moon and Planets, 31, 301–311

Merk, R., Prialnik, D., 2006, Combined modeling of thermal evolution and accretion of trans-neptunian objects-Occurrence of high temperatures and liquid water, Icarus, 183, 283–295

Merk, R., Breuer, D., Spohn, T., 2002, Numerical Modeling of ^{26}Al-Induced Radioactive Melting of Asteroids Considering Accretion, Icarus, 159, 183–191

Motschmann, U., 2009, Plasmaphysik, TU Braunschweig

Motschmann, U., Glassmeier, K., 1993a, Simulation of heavy ion ring and shell distributions downstream of the bow shock, Geophys. Res. Lett., 20, 987–990

Motschmann, U., Glassmeier, K., 1993b, Nongyrotropic distribution of pickup ions at comet P/Grigg-Skjellerup: A possible source of wave activity, J. Geophys. Res., 98, 20 977–+

Motschmann, U., Kührt, E., 2006, Interaction of the Solar Wind with Weak Obstacles: Hybrid Simulations for Weakly Active Comets and for Mars, Space Sci. Rev., 122, 197–208

Murray, W. D., Landis, F., 1959, Numerical and maschine solutions of transient heat conduction problems involving phase change., Journal of Heat Transfer, 81, 106–112

Neugebauer, M., 1990, Spacecraft observations of the interaction of active comets with the solar wind, Reviews of Geophysics, 28, 231–252

Ockendon, J. R., Hodgkins, W. R., 1975, Moving Boundary Problems in Heat Flow and Diffusion, Oxford University Press, New York

Omidi, N., Winske, D., 1990, Steepening of kinetic magnetosonic waves into shocklets - Simulations and consequences for planetary shocks and comets, J. Geophys. Res., 95, 2281–2300

Oort, J. H., 1950, The structure of the cloud of comets surrounding the Solar System and a hypothesis concerning its origin, Bull. Astron. Inst. Neth., 11, 91–110

Orosei, R., Capaccioni, F., Capria, M. T., Coradini, A., Espinasse, S., Federico, C., Salomone, M., Schwehm, G. H., 1995, Gas and dust emission from a dusty porous comet., Astron. Astrophys., 301, 613–+

Orosei, R., Capaccioni, F., Capria, M. T., Coradini, A., Sanctis, M. C. D., Federico, C., Salomone, M., Huot, J., 1999, Numerically improved thermochemical evolution models of comet nuclei, Planet. Space. Sci., 47, 839–853

Osip, D. J., Schleicher, D. G., Millis, R. L., 1992, Comets - Groundbased observations of spacecraft mission candidates, Icarus, 98, 115–124

Parker, E. N., 1958, Dynamics of the Interplanetary Gas and Magnetic Fields., Astrophys. J., 128, 664–+

Podolak, M., Prialnik, D., 1996, Models of the structure and evolution of comet P/Wirtanen, Planet. Space. Sci., 44, 655–664

Prialnik, D., 1992, Crystallization, sublimation, and gas release in the interior of a porous comet nucleus, Astrophys. J., 388, 196–202

Prialnik, D., 1997a, A Model for the Distant Activity of Comet Hale-Bopp, Astrophys. J., 478, L107+

Prialnik, D., 1997b, Modelling Gas and Dust Release from Comet Hale-Bopp, Earth Moon and Planets, 77, 223–230

Prialnik, D., 2006, What makes comets active?, in Asteroids, Comets, Meteors, (Ed.) L. Daniela, M. Sylvio Ferraz, & F. J. Angel, vol. 229 of IAU Symposium, pp. 153–170

Prialnik, D., Bar-Nun, A., 1987, On the evolution and activity of cometary nuclei, Astrophys. J., 313, 893–905

Prialnik, D., Merk, R., 2008, Growth and evolution of small porous icy bodies with an adaptive-grid thermal evolution code. I. Application to Kuiper belt objects and Enceladus, Icarus, 197, 211–220

Prialnik, D., Egozi, U., Ban-Nun, A., Podolak, M., Greenzweig, Y., 1993, On pore size and fracture in gas-laden comet nuclei, Icarus, 106, 499–+

Prialnik, D., Benkhoff, J., Podolak, M., 2004, Modeling the structure and activity of comet nuclei, in Comets II, (Ed.) Festou, M. C., Keller, H. U., & Weaver, H. A., pp. 359–387

Rauer, H., Helbert, J., Arpigny, C., Benkhoff, J., Bockelée-Morvan, D., Boehnhardt, H., Colas, F., Crovisier, J., Hainaut, O., Jorda, L., Kueppers, M., Manfroid, J., Thomas, N., 2003, Long-term optical spectrophotometric monitoring of comet C/1995 O1 (Hale-Bopp), Astron. Astrophys., 397, 1109–1122

Richardson, J. D., Paularena, K. I., Lazarus, A. J., Belcher, J. W., 1995, Radial evolution of the solar wind from IMP 8 to Voyager 2, Geophys. Res. Lett., 22, 325–328

Rickman, H., 1989, The nucleus of comet halley: Surface structure, mean density, gas and dust production, Advances in Space Research, 9, 59 – 71, ISSN 0273-1177

Rickman, H., Fernandez, J. A., 1986, Formation and blowoff of a cometary dust mantle, in Comet Nucleus Sample Return Mission, (Ed.) O. Melita, vol. 249 of ESA Special Publication, pp. 185–194

Rickman, H., Fernandez, J. A., Gustafson, B. A. S., 1990, Formation of stable dust mantles on short-period comet nuclei, Astron. Astrophys., 237, 524–535

Ridders, C., 1979, Three-point iterations derived from exponential curve fitting, Circuits and Systems, IEEE Transactions on, 26, 669 – 670, ISSN 0098-4094

Rodgers, S. D., Charnley, S. B., 1998, HNC and HCN in Comets, Astrophys. J., 501, L227+

Rosenberg, E. D., Prialnik, D., 2007, A fully 3-dimensional thermal model of a comet nucleus, New Astronomy, 12, 523–532, arXiv:astro-ph/0703250

Rosenberg, E. D., Prialnik, D., 2009, Fully 3-dimensional calculations of dust mantle formation for a model of Comet 67P/Churyumov-Gerasimenko, Icarus, 201, 740–749

Rubin, M., Hansen, K. C., Gombosi, T. I., Combi, M. R., Altwegg, K., Balsiger, H., 2009, Ion composition and chemistry in the coma of comet 1p/halley–a comparison between giotto's ion mass spectrometer and our ion-chemical network, Icarus, 199, 505 – 519, ISSN 0019-1035

Sanctis, M. D., Lasue, J., Capria, M., Magni, G., Turrini, D., Coradini, A., 2010, Shape and obliquity effects on the thermal evolution of the rosetta target 67p/churyumov-gerasimenko cometary nucleus, Icarus, 207, 341 – 358, ISSN 0019-1035

Schleicher, D. G., 2006, Compositional and physical results for Rosetta's new target Comet 67P/Churyumov Gerasimenko from narrowband photometry and imaging, Icarus, 181, 442–457

Schmidt, H. U., Wegmann, R., 1982, Plasma Flow and Magnetic Fields in Comets, in IAU Colloq. 61: Comet Discoveries, Statistics, and Observational Selection, (Ed.) L. L. Wilkening, pp. 538–+

Schulz, R., Stüwe, J. A., Böhnhardt, H., 2004, Monitoring Comet 67P/Churyumov-Gerasimenko from ESO in 2003, in The New Rosetta Targets. Observations, Simulations and Instrument Performances, (Ed.) L. Colangeli, E. Mazzotta Epifani, & P. Palumbo, vol. 311 of Astrophysics and Space Science Library, pp. 15–+

Schwehm, G., Schulz, R., 1999, Rosetta Goes to Comet Wirtanen, Space Science Reviews, 90, 313–319

Seiferlin, K., 1991, The thermal conductivity of porous ice with application to KOSI sample material: A review, in Theoretical Modelling of Comet Simulation Experiments, (Ed.) N. I. Kömle, S. J. Bauer, & T. Spohn, pp. 49–+

Seiferlin, K., Kömle, N. I., Kargl, G., Spohn, T., 1996, Line heat-source measurements of the thermal conductivity of porous H_2O ice, CO_2 ice and mineral powders under space conditions, Planet. Space. Sci., 44, 691–704

Sekanina, Z., 1979, Fan-shaped coma, orientation of rotation axis, and surface structure of a cometary nucleus. I - Test of a model on four comets, Icarus, 37, 420–442

Simon, S., Bagdonat, T., Motschmann, U., Glassmeier, K.-H., 2006, Plasma environment of magnetized asteroids: a 3-d hybrid simulation study, Annales Geophysicae, 24, 407–414, ISSN 0992-7689

Simon, S., Boesswetter, A., Bagdonat, T., Motschmann, U., 2007, Physics of the Ion Composition Boundary: a comparative 3-D hybrid simulation study of Mars and Titan, Annales Geophysicae, 25, 99–115

Simon, S., Boesswetter, A., Bagdonat, T., Motschmann, U., Schuele, J., 2007, Three-dimensional multispecies hybrid simulation of titan's highly variable plasma environment, Annales Geophysicae, 25, 117–144, ISSN 0992-7689

Skorov, Y. V., Kömle, N. I., Keller, H. U., Kargl, G., Markiewicz, W. J., 2001, A Model of Heat and Mass Transfer in a Porous Cometary Nucleus Based on a Kinetic Treatment of Mass Flow, Icarus, 153, 180–196

Smoluchowski, R., 1982, Heat transport in porous cometary nuclei, J. Geophys. Res., 87, 422–+

Spohn, T., Benkhoff, J., 1990, Thermal history models for KOSI sublimation experiments, Icarus, 87, 358–371

Spohn, T., Benkhoff, J., Klinger, J., Grun, E., Kochan, H., 1989, Thermal modelling of two KOSI comet nucleus simulation experiments, Advances in Space Research, 9, 127–131

Squyres, S. W., McKay, C. P., Reynolds, R. T., 1985, Temperatures within comet nuclei, J. Geophys. Res., 90, 12 381–+

Stadermann, F. J., Hoppe, P., Floss, C., Heck, P. R., Hörz, F., Huth, J., Kearsley, A. T., Leitner, J., Marhas, K. K., McKeegan, K. D., Stephan, T., 2008, Stardust in Stardust -The C, N, and O isotopic compositions of Wild 2 cometary matter in Al foil impacts, Meteoritics and Planetary Science, 43, 299–313

Stefan, J., 1891, Über die Theorie der Eisbildung, insbesondere über die Eisbildung im Polarmeere, Ann. der Phys. und Chem., 42, 269–286

Steiner, G., Koemle, N. I., 1991, A model of the thermal conductivity of porous water ice at low gas pressures, Planet. Space. Sci., 39, 507–513

Steiner, G., Kömle, N. I., Kührt, E., 1991, Thermal modelling of comet simulation experiments, in Theoretical Modelling of Comet Simulation Experiments, (Ed.) N. I. Kömle, S. J. Bauer, & T. Spohn, pp. 11–+

Stern, S. A., Colwell, W. B., Festou, M. C., Tamblyn, P. M., Parker, J. W., Slater, D. C., Weissman, P. R., Paxton, L. J., 1999, Comet Hale-Bopp (C/1995 O1) Near 2.3 AU Postperihelion: Southwest Ultraviolet Imaging System Measurements of the H_2O and Dust Production, The Astron. J., 118, 1120–1125

Stöffler, D., Duren, H., Knolker, J., Hische, R., Bischoff, A., 1991, Cometary analogue material - Preparation, composition, and thin section petrography, Geophys. Res. Lett., 18, 285–288

Tancredi, G., Rickman, H., Greenberg, J. M., 1994, Thermochemistry of cometary nuclei. 1: The Jupiter family case, Astron. Astrophys., 286, 659–682

Tancredi, G., Fernández, J. A., Rickman, H., Licandro, J., 2000, A catalog of observed nuclear magnitudes of Jupiter family comets, Astron. Astrophys., 146, 73–90

Tenishev, V., Combi, M., Davidsson, B., 2008, A Global Kinetic Model for Cometary Comae: The Evolution of the Coma of the Rosetta Target Comet Churyumov-Gerasimenko throughout the Mission, Astrophys. J., 685, 659–677

Thomas, P. C., Veverka, J., Belton, M. J., Hidy, A., A'Hearn, M. F., Farnham, T., Groussin, O., Li, J.-Y., McFadden, L. A., Sunshine, J., Wellnitz, D., Lisse, C., Schultz, P., Meech, K. J., Delamere, W. A., 2007, The shape, topography, and geology of tempel 1 from

deep impact observations, Icarus, 187, 4 – 15, ISSN 0019-1035, deep Impact Mission to Comet 9P/Tempel 1, Part 1

Trigo-Rodriguez, J. M., Blum, J., 2009, Tensile strength as an indicator of the degree of primitiveness of undifferentiated bodies, Planet. Space. Sci., 57, 243–249

Vasundhara, R., Chakraborty, P., 1999, Modeling of Jets from Comet Hale-Bopp (C/1995 O1): Observations from the Vainu Bappu Observatory, Icarus, 140, 221–230

Vetterling, W. T., Flannery, B. P., 2002, Numerical recipes example book (C++), Cambridge University Press, New York

Weaver, H. A., Feldman, P. D., A'Hearn, M. F., Arpigny, C., Brandt, J. C., Stern, S. A., 1999, Post-Perihelion HST Observations of Comet Hale-Bopp (C/1995 O1), Icarus, 141, 1–12

Wegmann, R., Schmidt, H. U., Huebner, W. F., Boice, D. C., 1987, Cometary MHD and chemistry, Astron. Astrophys., 187, 339–350

Weissman, P. R., Kieffer, H. H., 1981, Thermal modeling of cometary nuclei, Icarus, 47, 302–311

Whipple, F. L., 1950, A comet model. I. The acceleration of Comet Encke, Astrophys. J., 111, 375–394

Xie, X., Mumma, M. J., 1996, Monte Carlo Simulation of Cometary Atmospheres: Application to Comet P/Halley at the Time of the Giotto Spacecraft Encounter. II. Axisymmetric Model, Astrophys. J., 464, 457–+

Young, D. T., Crary, F. J., Nordholt, J. E., Bagenal, F., Boice, D., Burch, J. L., Eviatar, A., Goldstein, R., Hanley, J. J., Lawrence, D. J., McComas, D. J., Meier, R., Reisenfeld, D., Sauer, K., Wiens, R. C., 2004, Solar wind interactions with Comet 19P/Borrelly, Icarus, 167, 80–88